AL-TR-90-039

AD:

Final Report
or the period
1 Aug 1986 to
30 Nov 1989

Theoretical Studies of the Lifetime of Metastable H_3

November 1990

Author:
Aron Kuppermann

California Institute of Technology
Division of Chemistry and Chemical Engineering
Pasadena CA 91125

F04611-86-K-0067

Approved for Public Release

Distribution is unlimited. The AL Technical Services Office has reviewed this report, and it is releasable to the National Technical Information Service, where it will be available to the general public, including foreign nationals.

Prepared for the: **Astronautics Laboratory (AFSC)**
Air Force Space Technology Center
Space Systems Division
Air Force Systems Command
Edwards AFB CA 93523-5000

NOTICE

When U.S. Governemt drawings, specifications, or other data are used for any purpose other than a defintely related G ernment procurement operation, the fact that the Government may have formulated, fu nished, or in any way supplied the said drawings, specifications, or other data, is not to be regarded by implication or otherwise, or in any way licensing the holder or any other person or corporation, or conveying any rights or permission to manufacture, use, or sell any patented invention that may be related thereto.

FOREWORD

This final report was submitted by the California Institute of Technology, Pasadena CA on completion of contract F04611-86-K-0067 with the Astronautics Laboratory (AFSC), Edwards AFB CA. Capt Tim Wiley was the Project Manager.

This report has been reviewed and is approved for release and distribution in accordance with the distribution statement on the cover and on the DD Form 1473.

Timothy G. Wiley

TIMOTHY G. WILEY, CAPT, USAF
Project Manager

Stephen L. Rodgers

STEPHEN L. RODGERS
Chief, Advanced Research in Energy Storage Office

FOR THE DIRECTOR

Robert C Corley

ROBERT C. CORLEY
Director, Astronautical Sciences Division

SECURITY CLASSIFICATION OF THIS PAGE

REPORT DOCUMENTATION PAGE

Form Approved OMB No. 0704-0188

1a. REPORT SECURITY CLASSIFICATION: UNCLASSIFIED	1b. RESTRICTIVE MARKINGS
2a. SECURITY CLASSIFICATION AUTHORITY	3. DISTRIBUTION/AVAILABILITY OF REPORT: Approved for public release; Distribution is unlimited
2b. DECLASSIFICATION/DOWNGRADING SCHEDULE	
4. PERFORMING ORGANIZATION REPORT NUMBER(S)	5. MONITORING ORGANIZATION REPORT NUMBER(S): AL-TR-90-039
6a. NAME OF PERFORMING ORGANIZATION: California Institute of Technology; 6b. OFFICE SYMBOL (If applicable)	7a. NAME OF MONITORING ORGANIZATION: Astonautics Laboratory (AFSC)
6c. ADDRESS (City, State, and ZIP Code): Division of Chemistry and Chemical Engrg, Mail Code 127-72, Pasadena CA 91125	7b. ADDRESS (City, State, and ZIP Code): AL/LSX, Edwards AFB CA 93523-5000
8a. NAME OF FUNDING/SPONSORING ORGANIZATION; 8b. OFFICE SYMBOL (If applicable)	9. PROCUREMENT INSTRUMENT IDENTIFICATION NUMBER: F04611-86-K-0067
8c. ADDRESS (City, State, and ZIP Code)	10. SOURCE OF FUNDING NUMBERS

PROGRAM ELEMENT NO.	PROJECT NO.	TASK NO	WORK UNIT ACCESSION NO.
62302F	5730	00WP	342400

11. TITLE (Include Security Classification)

Theoretical Studies of the Lifetime of Metastable H_3 (U)

12. PERSONAL AUTHOR(S)

Kuppermann, Aron

13a. TYPE OF REPORT	13b. TIME COVERED	14. DATE OF REPORT (Year, Month, Day)	15. PAGE COUNT
Final	FROM 860801 TO 891130	9011	118

16. SUPPLEMENTARY NOTATION

17. COSATI CODES			18. SUBJECT TERMS (Continue on reverse if necessary and identify by block number)
FIELD	GROUP	SUB-GROUP	trihydrogen, tetrahydrogen, H_3, H_4, double many body expansion, DMBE, molecular Aharonov-Bohm, MAB, metastable lifetimes
07	02		
21	09		

19. ABSTRACT (Continue on reverse if necessary and identify by block number)

In this report, the major steps toward the ab initio determination of the lifetime (via both the radiation and the predissociation decay mechanisms) for the H_3 metastable states have been identified and analyzed. Some results on the ab initio calculation of the lowest four electronic potential energy surfaces of the H_3 system are presented, as well as the electric transition dipole moments between them. The ro-vibrational eigenstates of H_3 (for total angular momentum J=0 and J=1) on the upper sheet of the Double Many Body Expansion (DMBE) surfaces have been calculated. A new hypershperical coordinate propagation method has been developed and applied to the similar calculation of the ro-vibrational motion of H_3 with inclusion of the nuclear permutation symmetry and the Molecular Aharonov-Bohm (MAB) effect (or Berry's geometric phase). This effect has a profound influence on both the bound and scattering states of this system.

20. DISTRIBUTION/AVAILABILITY OF ABSTRACT	21. ABSTRACT SECURITY CLASSIFICATION
☒ UNCLASSIFIED/UNLIMITED ☐ SAME AS RPT. ☐ DTIC USERS	UNCLASSIFIED

22a. NAME OF RESPONSIBLE INDIVIDUAL	22b. TELEPHONE (Include Area Code)	22c. OFFICE SYMBOL
Capt Tim Wiley	(805) 275-5749	LSX

DD Form 1473, JUN 86 — Previous editions are obsolete. — SECURITY CLASSIFICATION OF THIS PAGE

Tables of Contents

List of Figures

1. SCIENTIFIC BACKGROUND

1.1 Motivation

Unlike the H_3 system in its ground electronic state, which does not support any bound states of nuclear motion, this system is known to have a long-lived[1-4] excited Rydberg state $2p_z\ ^2A_2''$. The high resolution spectroscopic measurements of Herzberg and co-workers[5-9] and of Helm and co-workers[10-13] confirmed it beyond doubt. A very intense beam of H_3 in this metastable state has been generated by Garvey and Kuppermann[14]. Their estimation of the lifetime of this metastable state is more than 40 μ seconds. This metastable H_3 species can liberate 180 Kcal/mole (7.8 eV/molecule) when decomposing into $H_2(X\ ^1\Sigma_g^+)$ molecules according to $H_3(2p_z\ ^2A_2'') \longrightarrow 3/2H_2(X\ ^1\Sigma_g^+)$. Its specific impulse (ISP) is estimated to be about 2050s, while current rocket fuels have ISP of the order of only 400s. Such a high ISP makes H_3 a very interesting rocket propellant candidate.

What the lifetime of this metastable H_3 actually is, via what kind of mechanism it decays, and how collisions affect this lifetime are important questions whose answers are needed in assessing its potential as a possible rocket propellant. One of the decay channels is the ro-vibrational predissociation of the $2p_z\ ^2A_2''$ metastable electronic state into the $2p\ ^2E'$ repulsive ground electronic state. It is difficult to measure directly the lifetime of this channel, because it is not accompanied by any emission of radiation. The total lifetime estimation from linewidth measurements[5-9] suffers from the Doppler broadening effects inside the plasma sources which are used to generate H_3 metastable molecules, especially if the lifetime of interest is long, as is the case for the H_3 in the $2p_z\ ^2A_2''$ state. For this reason, a theoretical investigation of its lifetime (for both radiative and predissociative processes) is highly desirable. This theoretical investigation should also provide guidance for the experimental studies of the properties of this metastable species.

1.2 Decay Processes and Lifetime

In the theory of predissociation processes, the lifetime τ of a bound state predissociating to an unbound state can be expressed as[15,16]

$$\tau_m^{-1} = \frac{\hbar}{2\pi} \mid V_{E_m}^m \mid^2 \tag{1}$$

$$V_E^m = < \Psi_m \mid H' \mid \Psi_E > \tag{2}$$

In these expressions, Ψ_m is the wavefunction of the bound state with quantum number m and energy E_m, Ψ_E is that of the unbound state with total energy E, and H' is the part of total Hamiltonian which provides the coupling between the bound state and unbound

state. V_E^m is called the coupling matrix element between these two states. The integration in Eq. 2 is over the coordinates of all electrons and nuclei. The choices of normalization for the above two wavefunctions are:

$$< \Psi_m \mid \Psi_m >= 1 \tag{3}$$

$$< \Psi_E \mid \Psi_{E'} >= \delta(E - E') \tag{4}$$

For electric dipole transitions, the Einstein coefficient between an initial state Ψ_i and a final state Ψ_f is[17]

$$A_{i,f} = (4\alpha\omega^3/3c^2)|< \Psi_i \mid \mathbf{T} \mid \Psi_f >|^2 \tag{5}$$

and the spontaneous radiation lifetime of this process is

$$\tau = \frac{1}{A_{i,f}} \tag{6}$$

where α is the fine structure constant, ω the frequency of the emitted photon, and c the speed of light. Here again the initial and final state wavefucntions are normalized as in Eqs. 3 and 4. $< \Psi_i \mid \mathbf{T} \mid \Psi_f >$ is the electric transition dipole moment between the initial and the final states, and again the integration in Eq. 5 is over the coordinates of all electrons and nuclei. For molecular systems, the total wavefunctions in Eqs. 2 through 4 can be written, using the Born-Oppenheimer approximation[18], as

$$\Psi_{total} = \Psi_{electr}\Psi_{nucl} \tag{7}$$

Here Ψ_{electr} is the electronic wavefunction with fixed nuclear coordinates as parameters and Ψ_{nucl} describes the nuclear motion in an effective potential generated by the electron motion (*i.e.*, the electronic potential energy surface).

In order to calculate both the radiative and predissociative lifetimes, Eqs. 1 through 7 show that the following quantities are needed:

1. The wavefunctions which are solutions of the electronic motion Schrodinger equation for the $2p_z\ ^2A_2''$ state and all lower energy electronic states ($2p\ ^2E'(1)$, $2p\ ^2E'(2)$ and $2s\ ^2A_1'$), to which the $2p_z\ ^2A_2''$ state may decay either radiatively or predissociatively. The resulting electronic potential energy surfaces are needed for solving for the wavefunctions of the nuclear motion.

2. The coupling matrix elements between those electronic states.

3. The electric transition dipole moments among those electronic states.

4. The ro-vibrational states of the nuclear motion in the field of the potential energy surfaces which support bound states. The energy eigenvalues of those states will determine the spectroscopic transition energies, and the wavefunctions are needed in the lifetime calculations.

5. The scattering wavefunction on the ground potential energy surface.

The following sections describe in detail the progress achieved so far in obtaining these different quantities necessary for the calculation of the radiative and predissociative lifetimes.

2. Calculation of the Electronic Wavefunctions and Energies of H_3

2.1 General Consideration

The first step toward the investigation of the lifetime of the $2p_z\ ^2A_2''$ metastable state of H_3 is to calculate the electronic potential energy surfaces of the ground and the first three excited electronic states, as well as the electronically non-adiabatic coupling matrix elements and the electric dipole transition moments between those electronic states. We originally hoped that these quantities would be calculated by other groups. Since this has not turned out to be the case, we initiated a program to calculate them ourselves.

Let us first introduce the notation for those states. When the three protons form an equilateral triangle, the electronic ground state is degenerate with the first excited state, and the two generate the $2p\ ^2E'$ representation of the D_{3h} point group[19]. The second and third excited electronic states are classified as $2s\ ^2A_1'$ and $2p_z\ ^2A_2''$. The x and y axes are in the molecular plane, while the z axis is perpendicular to it. ($2s$, $2p_{x,y,z}$) are the state assignments for an Li atom in the united-atom limit (UA). We still use this notation to identify those states even when the nuclear geometry is no longer an equilateral triangle.

The potential energy surface is well known when the three electrons are in the $2p\ ^2E'(1)$ ground state[19-22]. Using a functional extrapolation and the double many body expansion method[23-26], Varanda *et al.* also obtained the potential energy surface of the $2p\ ^2E'(2)$ state which, for the equilateral triangle nuclear geometry, is degenerate with the ground state[20,22]. Along with the potential energy surfaces, the major coupling matrix elements between the ground state and the first excited state were also obtained using the same method[22].

After the first H_3 spectroscopic measurements[5], several theoretical electronic calculations for this system with equilateral triangle nuclear geometry have been made[27-30], Emphasis was placed on the calculation of a large number of electronic states, in order to reproduce the observed pattern of the experimental energy levels in the H_3 Rydberg spectra. Figure 1 is the state correlation diagram between an equilateral triangular H_3 and a diatom H_2 plus a distant atom H. In these calculations, a frozen core approximation was used for H_3^+, plus single Rydberg excitations for the third electron. These limited calculations agree with each other and are qualitatively successful in explaining the experimental spectra. The frozen core treatment gives however poor results for the $2p\ ^2E'(1,2)$ states, and also over-estimates the energy gap between the $2s\ ^2A_1'$ and $2p_z\ ^2A_2''$ states by a factor of 1.6 to 2.0 [32] at the inter-nuclear distance $R = 1.64$ bohr.

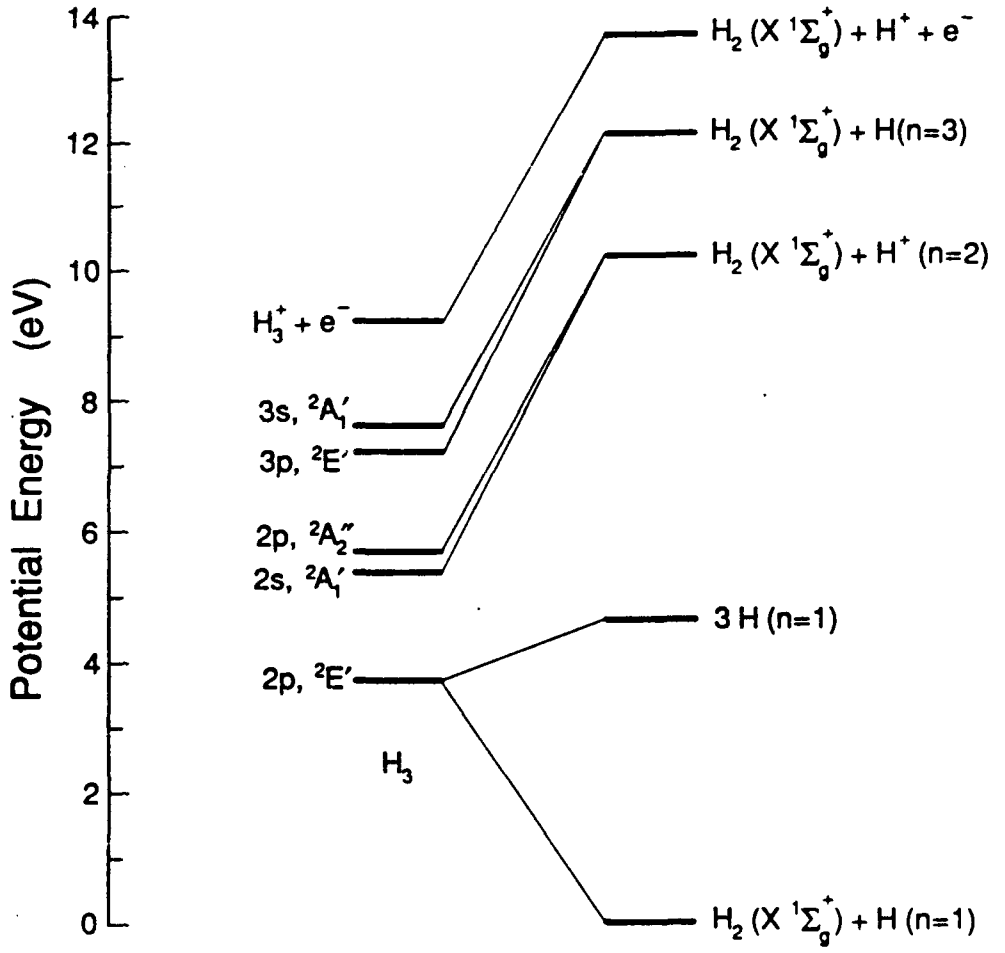

Figure 1: Energy Level and Correlation Diagram for H_3. The spacing of the H_3 energy levels was obtained theoretically for an equilateral triangle configuration[27] and referred to the energy of dissociated products by the results of a separate calculation[31].

Recently another calculation for several of the low electronic states of H_3 in some special geometries has been published[32]. The MRD-CI method used in that work is very general and powerful[33,34]. It could be used with arbitrary nuclear geometries and to generate the full potential energy surfaces. It also offers a much better description of the $2p\ ^2E'(1,2)$ states, and reduces the energy gap between the $2s\ ^2A_1'$ and $2p_z\ ^2A_2''$ states to just 10% greater than the experimental measurement[32]. The electric dipole transition moment between these two states for an equilateral triangle nuclear geometry with the internuclear distance of R=1.64 bohr agrees with the previous calculations. Because of its capability and performance, we chose this method for our calculations and initiated a collaboration with Professor J.S. Wright[32] of Carleton University, Ottawa, Canada.

2.2 MRD-CI method

The details behind the MRD-CI (Multi-Reference, single and Double excitation Configuration Interaction) are beyond the scope of this report and can be found elsewhere[33,34]. Only the major steps of the calculation are briefly described below:

1. First, a set of atomic orbitals (AO) are chosen. Gaussian-Type atomic orbitals (GTO) are used[35].

2. Second, the nuclear geometry is taken into account. A set of symmetry-adapted functions (SAF) is constructed by linear combinations of the set of atomic orbitals. By taking advantage of the nuclear geometry symmetry, the MRD-CI calculation for a given molecular system can be speeded up significantly.

3. In the third step, the Self Consistant Field (SCF) calculation with this SAF-AO basis set is conducted in an iterative manner. The molecular orbitals (MO) obtained from the SCF serve as the starting point for the CI calculation.

4. In the forth step, before the CI calculation, a reference configuration set and an threshold energy are chosen. All the single and double excitations over the reference configurations are generated. First, a small scale CI calculation with N_{ref} reference configurations is performed and an estimation of the eigen-energies of these wanted states is obtained. Then, one by one, each generated configuration is tested by being added to the reference configuration set and another small scale CI calculation of $N_{ref}+1$ configurations is performed. Only those configurations which lower the energy of any one of the states of interest by an amount bigger than the threshold energy are included in the final CI calculation. This is a way of drastically reducing the final CI space size without missing important contributions from the full single and double excitation CI space. In order to

ensure the convergence of the calculation, the reference configuration set is chosen to be big enough so that the final wavefunction of each wanted state has at lease 90% of its contribution from the reference configurations.

5. The fifth step uses a large fraction of the total CPU time. It is the diagonalization of the electronic Hamiltonian including all the configurations selected. After that, another calculation with a new threshold twice as large as old one is made, including the selection of the configurations to be added to the reference set and the final diagonolization. Assuming the correctness of the extrapolation back to the zero threshold energy, the final CI energies can be approximated to even better values, without doing the calculation at such a small threshold energy as to make the calculation too costly. This is the most important aspect of this MRD-CI method.

6. With the resulting electronic wavefunctions, the electric transition dipole moment between any two known electronic states is then calculated.

2.3 Numerical Details and Results

The version of the MRD-CI code for Sun workstations was obtained from Professor Wright[32]. The CRAY version was obtained directly from Professor Buenker's group[33,34]. These codes do not have the capability of calculating the electronically non-adiabatic coupling matrix elements between two electronic states, and will have to be modified in the future to permit such calculations, which is needed in the predissociative lifetime calculation.

Initially we made small testing runs on Sun workstations (Sun-386i, Sun-3, and Sun-4) and a micro VAX. The production runs have been done on the JPL CRAY-XMP and the SDSC CRAY-YMP. The typical CPU time on the CRAY-YMP is about 400s for a complete calculation at a single nuclear configuration, using the largest one of the basis sets described below.

The details of the Gaussian-Type atomic orbitals (GTO) are given in Ref. 31. In summary, they are defined as:

$$\chi(n_g, \zeta_i, l, m) = N_{n_g,i}\, r^{n_g-1} \exp(-\xi_i r^2) Y_{l,m}(\theta, \phi) \qquad (8)$$

where $N_{n_g,i}$ is a normalization factor and $Y_{l,m}(\theta, \phi)$ the spherical harmonic function. (r, θ, ϕ) are the spherical coordinates of a point with respect to the origin of the GTO. n_g can have the values 1, 2, 3, ... , l can have the values 0, 1, 2, ... (which corresponds to

s, p, d, ... orbitals), and m can vary from $-l$ to l in steps of unity. i is an index for the exponent ξ_i. Sometimes $r^{n_g-1}Y_{l,m}(\theta,\phi)$ is replaced by linear combinations of terms of the form $x^{n_x}y^{n_y}z^{n_z}$, where $(x,\ y,\ z)$ are Cartesian coordinates and n_x, n_y, n_z are non-negative integers whose sum equals $n_g - 1$.

In some applications contracted basis functions are used. They are defined as linear combinations of similar GTO functions having the same quantum numbers n_g, l, m but different exponents ξ_i.

$$\chi_{\rm contr}(n_g,.,m) = \sum_i C_i \chi(n_g,\zeta_i,l,m) \tag{9}$$

The C_i are called the coefficients of the contraction.

We have used two GTO basis sets. The first one is a variation of the basis set used in Ref. 28. It consists of $(10s/8s,\ 4p)$ orbitals, in which there are eight s-type GTOs (one of them being a contraction of three s-type GTOs), and four p-type GTOs. The second basis set consists of $(12s/7s,\ 4p,\ 1d)$ orbitals, with seven s-type GTOs (one of them contracted from six s-type GTOs), four p-type GTOs and one d-type GTOs. The main part of it, $10s/5s,\ 4p,\ 1d$, is adopted from one used in a H_3^+ calculation[36], with the intention to provide simultaneously an accurate description of the system's valence space and the Rydberg states arising from n=2 hydrogen orbitals. In order to improve the description of the Rydberg states of the H_3 system, we added two diffuse Gaussian s-type functions into that basis set, with exponents 0.01149 and 0.0042 (see Tables 1 and 2 for details).

Both GTO basis sets have been tested and calibrated in calculations for an isolated H atom, and an isolated H_2 molecule with bond length R=1.4 bohr. The results are shown in Table 3. The H atom calculation shows that both sets give a fairly good description of the $H(1s)$, $H(2s)$, and $H(2p_{x,y,z})$ atomic states. The H_2 results clearly show that the $(12s/7s,\ 4p,\ 1d)$ basis set offers a much better description of the $H_2(X\ ^1\Sigma_g^+)$ and $H_2(b\ ^3\Sigma_u^+)$ states than does the $(10s/8s,\ 4p)$ one. Because we are interested in correlating the $2p_z\ ^2A_2''$, $2s\ ^2A_1'$ and $2p\ ^2E'(1,2)$ states of H_3 with these two diatomic states mentioned above plus a free H atomic state (see Figure 1), it is important to have a good description of these diatomic states.

In the H_3 system, the most general geometric symmetry is the reflection symmetry C_s with respect to the plane of these three nuclei. In order to take advantage of this symmetry, we placed the nuclei in the $x\ y$ plane, with one nucleus at the origin of the

Table 1: (10s/8s, 4p) Gaussian-type basis set.

orbital	i	ξ_i	C_i
1s	1 2 3	68.16 10.2465 2.34648	0.002558 0.01938 0.0928
2s	1	0.67332	1.00000
3s	1	0.22466	1.00000
4s	1	0.0822	1.00000
5s	1	0.0475	1.00000
6s	1	0.01875	1.00000
7s	1	0.0133	1.00000
8s	1	0.00525	1.00000
1p	1	0.7	1.00000
2p	1	0.20	1.00000
3p	1	0.06	1.00000
4p	1	0.024	1.00000

Table 2: $(12s/7s,\ 4p,\ 1d)$ Gaussian-type basis set.

orbital	i	ξ_i	C_i
1s	1	837.22	0.000112
	2	123.524	0.000895
	3	27.7042	0.004737
	4	7.82599	0.019518
	5	2.6504	0.065862
	6	0.938258	0.178008
2s	1	0.372145	1.00000
3s	1	0.155838	1.00000
4s	1	0.066180	1.00000
5s	1	0.027580	1.00000
6s	1	0.011490	1.00000
7s	1	0.004200	1.00000
1p	1	1.6	1.00000
2p	1	0.40	1.00000
3p	1	0.09	1.00000
4p	1	0.025	1.00000
1d	1	1.0	1.00000

Table 3: Calibration of the basis sets for isolated H and H_2[a].

Calculated H energy levels

Gaussian basis set	$H(1s)$	$H(2s)$	$H(2p_x)$	$H(2p_y)$	$H(2p_z)$
10s/8s, 4p	-0.499942	-0.124989	-0.124812	-0.124812	-0.124812
12s/7s, 4p, 1d	-0.499998	-0.124992	-0.124723	-0.124723	-0.124723
Exact value	-0.500000	-0.125000	-0.125000	-0.125000	-0.125000

Calculated H_2 energy levels (R=1.4)

Gaussian basis set	$H_2(X\ ^1\Sigma_g^+)$	$H_2(b\ ^3\Sigma_u^+)$
10s/8s, 4p	-1.170045	-0.782718
12s/7s, 4p, 1d	-1.173652	-0.783904
KW[b]	-1.174474	-0.784150

a: The energies are in hartree and the bond lenth of diatom is in bohr.

b: Accurate values from W. Kolos and L. Wolniewicz[37].

$(x,\ y,\ z)$ coordinate system, another along the positive x axis and the third in the $x\ y$ half plane with y positive. The ground state $2p\ ^2E'(1)$, and the excited states $2p\ ^2E'(2)$, and $2s\ ^2A_1'$ are symmetric under that symmetry operation ($z \rightarrow -z$), while the $2p_z\ ^2A_2''$ state is anti-symmetric.

We place sets of GTOs (as listed in Tables 1 and 2) at each of the three nuclei. There are 20 basis functions for the $(10s/8s,\ 4p)$ basis set and 25 for the $(12s/7s,\ 4p,\ 1d)$ basis set, where there is one function for each s type GTO, three for each p type GTO and six for each d type GTO. Because we have three nuclei, the total numbers of basis functions are 60 for the first case and 75 for the second.

We obtain the energies and wavefunctions for the ensemble of states symmetric with respect to reflection through the nuclear plane in one calculation and the antisymmetric ensemble in another one. The energy threshold is 2.0×10^{-6} hartree for the symmetric ensemble, for both sets of basis functions. For the antisymmetric ensemble, the energy threshold is 0.5×10^{-6} hartree for the $(12s/7s,\ 4p, 1d)$ basis set and 1.0×10^{-6} hartree for the $(10s/8s,\ 4p)$ one. Since the choice of reference configurations depends on the nuclear geometry, we had to adjust it through a trial and error process for each nuclear geometry. Generally speaking, we used about 45 to 49 reference configurations in the calculation of the symmetric ensemble, and about 20 in the calculation of the antisymmetric one.

In Tables 4 and 5, we list the energies of the first four electronic states with the equilateral triangle nuclear geometry for each basis set. These results are plotted in Figures 2 and 3. In Tables 6 and 7, we list the electric transition dipole moments for this geometry. Comparison of the results from the $(12s/7s,\ 4p,\ 1d)$ basis set for the $2p\ ^2E'(1,2)$ states with those of the DMBE calculation[22] shows that our curve is nearly parallel to the DMBE one with an upward shift of about 0.003 hartree. Comparison between the results of the $(10s/8s,\ 4p)$ basis set and those in Ref. 28 shows good agreement (except at R = 2.6 bohr). GTO functions located at the the center of mass of three nuclei have been used in Ref. 28, while a larger set of basis functions located at each nucleus is used in present calculation. Comparison of Tables 4 and 5 shows that the results with the two basis sets listed in Tables 1 and 2 are not parallel to each other. This indicates that it is necessary for us to use the larger basis set $(12s/7s,\ 4p.\ 1d)$ in our final production runs in order to get a potential energy surface having the correct shape.

The C_s symmetry ensures that the electric transition dipole moments between the antisymmetric $2p_z\ ^2A_2''$ state and the symmetric $2p\ ^2E'(1)$, $2p\ ^2E'(2)$ and $2s\ ^2A_1'$ states have

Table 4

Electronic potential energies (in hartree) of the first four electronic states of H_3[a] for the (10s/8s, 4p) bas

R[b]	$2p\ ^2E'(1)$	$2p\ ^2E'(2)$	$2s\ ^2A_1'$	$2p_z\ ^2A_2''$
1.0	-1.273839	-1.273825	-1.267978	-1.245835
1.2	-1.431537	-1.431503	-1.404972	-1.388900
1.4	-1.510877	-1.510886	-1.462253	-1.451243
1.6	-1.549290	-1.549231	-1.477925	-1.470966
1.64	-1.553811	-1.553849	-1.478022	-1.471764
1.8	-1.564752	-1.564771	-1.471242	-1.467687
2.0	-1.568660	-1.568710	-1.452355	-1.451797
2.2	-1.565200	-1.565174	-1.427605	-1.429583
2.4	-1.558467	-1.558474	-1.400492	-1.404303
2.6	-1.550885	-1.550780	-1.373003	-1.378150
2.8	-1.542112	-1.542476	-1.345840	-1.352258
3.0	-1.534483	-1.534565	-1.319509	-1.327177

a: The origin of energy is that of the six particles (three electrons and three protons) at infinite separation. The energy of three independent $H(1s)$ is -1.500000 hartree. These three nuclei form an equilateral triangle.

b: in bohr.

Table 5

Electronic potential energies (in hartree) of the first four electronic states of H_3[a] for the (12s/7s, 4p, 1d) basis set.

R[b]	$2p\ ^2E'(1)$	$2p\ ^2E'(2)$	$2s\ ^2A_1'$	$2p_z\ ^2A_2''$
1.0	-1.286448	-1.286430	-1.280663	-1.258265
1.2	-1.441703	-1.441650	-1.415028	-1.398848
1.4	-1.518046	-1.518017	-1.468988	-1.458043
1.6	-1.554349	-1.554268	-1.482113	-1.475586
1.64	-1.558556	-1.558507	-1.481895	-1.475080
1.8	-1.569022	-1.568989	-1.474258	-1.471001
2.0	-1.571945	-1.571928	-1.455205	-1.454669
2.2	-1.568548	-1.568561	-1.430550	-1.432079
2.4	-1.561349	-1.561420	-1.403023	-1.406783
2.6	-1.552813	-1.552907	-1.375206	-1.380527
2.8	-1.544312	-1.544450	-1.347990	-1.354630
3.0	-1.536907	-1.536859	-1.322044	-1.329407

a: The origin of energy is that of the six particles (three electrons and three protons) at infinite separation. The energy of three independent $H(1s)$ is -1.500000 hartree. These three nuclei form an equilateral triangle.

b: in bohr.

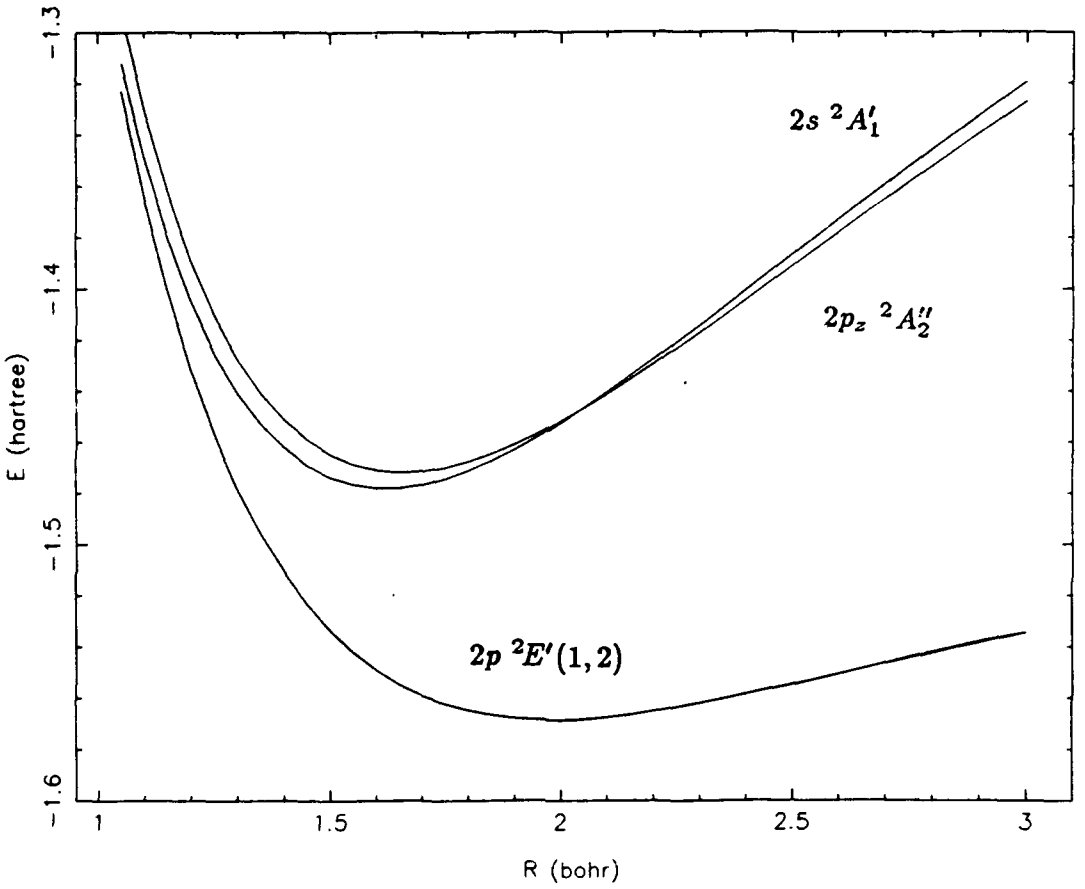

Figure 2: Potential Energy Curves for Equilateral H_3. R is the length of the side of the triangle. The $(10s/8s,\ 4p)$ basis set was used. The $2p\ ^2E'(1)$ and $2p\ ^2E'(2)$ curves are not completely degenerate with each other because of inaccuracies introduced by the limited basis set. But the difference between them can not be discerned on the scale of the plot (see Table 4).

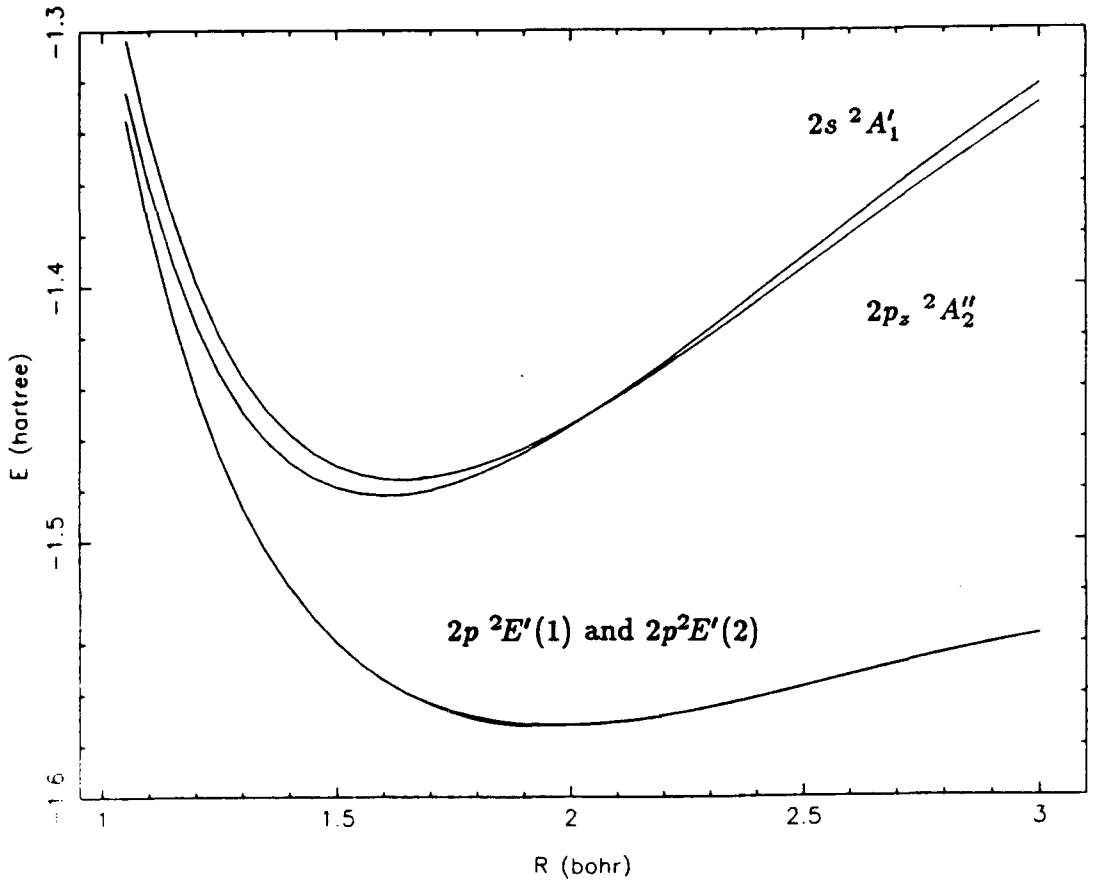

Figure 3: Potential Energy Curves for Equilateral H_3. R is the length of the side of the triangle. The $(12s/7s,\ 4p,\ 1d)$ basis set was used. The $2p\ ^2E'(1)$ and $2p\ ^2E'(2)$ curves are not completely degenerate with each other because of inaccuracies introduced by the limited basis set (see Table 5).

Table 6

Transition dipole moment[a] (in atomic units) among the first four electronic states of H_3 for the $(10s/8s,\ 4p)$ basis set.

R[b]	T41(z)	T42(z)	T43(z)
1.0	0.769(-3)	0.451(-3)	2.61
1.2	-0.632(-3)	0.230(-3)	2.63
1.4	0.642(-4)	0.705(-3)	2.65
1.6	0.101(-2)	-0.593(-4)	2.66
1.64	-0.108(-5)	0.148(-3)	2.66
1.8	0.376(-3)	-0.486(-3)	2.66
2.0	-0.159(-3)	0.204(-3)	2.69
2.2	0.596(-3)	-0.751(-4)	2.70
2.4	0.120(-2)	-0.116(-2)	2.73
2.6	0.707(-3)	0.102(-2)	2.76
2.8	0.531(-3)	0.677(-3)	2.78
3.0	-0.349(-3)	0.271(-3)	-2.80

R[b]	T31(x)	T31(y)	T32(x)	T32(y)	T21(x)	T21(y)
1.0	1.70	-1.48	1.48	1.70	-0.759(-2)	-0.590(-1)
1.2	1.64	1.24	-1.24	1.64	-0.269(-1)	0.935(-1)
1.4	-0.673(-1)	-1.85	1.85	-0.651(-1)	0.139	0.974(-2)
1.6	1.44	-0.803	0.803	1.44	-0.938(-1)	-0.152
1.64	1.11	1.19	-1.19	1.11	0.136(-1)	0.186
1.8	-0.628	1.35	1.35	0.627	-0.142	0.168
2.0	1.29	-0.290	.290	1.29	-0.226	-0.108
2.2	1.12	0.360	-0.359	1.12	-0.218	0.158
2.4	0.953	0.443	-0.440	0.956	-0.179	0.212
2.6	0.373	0.840	0.841	-0.371	-0.180	-0.198
2.8	0.393	0.733	0.730	-0.389	-0.140	-0.209
3.0	-0.177	-0.720	-0.718	0.174	-0.194	-0.101

a: Tij is the transition dipole vector for equilateral triangle configurations. The indices (1, 2, 3, 4) refer to the

four electronic states $(2p\ ^2E'(1),\ 2p\ ^2E'(2),\ 2s\ ^2A_1',\ 2p_z\ ^2A_2'')$ respectively.

b: in bohr.

Table 7

Transition dipole moment[a] (in atomic units) among the first four electronic states of H_3 for the $(12s/7s,\ 4p,\ 1d)$ basis set.

R[b]	T41(z)	T42(z)	T43(z)
1.0	-0.432(-3)	-0.194(-3)	-2.61
1.2	0.541(-3)	0.120(-3)	-2.63
1.4	-0.483(-3)	-0.489(-3)	-2.65
1.6	0.809(-3)	0.546(-3)	-2.68
1.64	-0.830(-3)	0.378(-3)	2.69
1.8	0.647(-3)	-0.538(-3)	-2.71
2.0	0.497(-3)	0.732(-3)	-2.74
2.2	-0.140(-3)	0.100(-2)	-2.75
2.4	0.904(-3)	-0.556(-3)	-2.78
2.6	0.152(-2)	-0.153(-3)	-2.80
2.8	0.150(-2)	-0.206(-3)	-2.81
3.0	0.710(-3)	-0.758(-4)	-2.82

R[b]	T31(x)	T31(y)	T32(x)	T32(y)	T21(x)	T21(y)
1.0	-2.25	-0.944(-1)	-0.927(-1)	2.26	0.586(-1)	-0.521(-1)
1.2	0.199	2.04	2.04	-0.198	-0.916(-1)	-0.182(-1)
1.4	-0.161	-1.83	-1.84	0.159	-0.131	-0.227(-1)
1.6	1.22	1.10	1.09	1.22	-0.202(-1)	-0.172
1.64	-1.38	0.801	0.803	1.39	0.909(-1)	0.157
1.8	0.362	1.41	1.41	0.361	0.189	0.103
2.0	0.372	1.25	1.25	-0.371	-0.207	-0.135
2.2	0.424	1.07	1.06	-0.421	-0.194	-0.182
2.4	0.474	0.918	-0.917	0.472	0.161	0.225
2.6	0.446	0.812	-0.814	0.444	0.148	-0.226
2.8	0.443	0.702	0.700	-0.439	-0.111	-0.226
3.0	-0.388	-0.639	-0.632	0.385	-0.104	-0.196

a: Tij is the transition dipole vector for equilateral triangle configurations. The indices (1, 2, 3, 4) refer to the four electronic states ($2p\ ^2E'(1)$, $2p\ ^2E'(2)$, $2s\ ^2A_1'$, $2p_z\ ^2A_2''$) respectively.

b: in borh.

only z components, and the ones between these symmetric states have no z components. Since the wavefunctions have been determined by the variational calculation up to a phase factor, all transition dipoles are subject to a possible sign change.

Although C_s is the only symmetry embedded into the calculation, when three nuclei form an equilateral triangle, the D_{3h} symmetry group associated with this geometry will manifest itself via the following features:

1: The $2p\ ^2E'(1)$ and $2p\ ^2E'(2)$ states are nearly degenerate.

2: The electric transition dipoles from the $2p_z\ ^2A_2''$ state to the $2p\ ^2E'(1)$ and $2p\ ^2E'(2)$ states are close to zero.

3: Because of the degeneracy between the $2p\ ^2E'(1)$ and $2p\ ^2E_2'$ states (under the symmetry of an equilateral triangle), they can always be written as:

$$| 2p\ ^2E'(1)\rangle = \cos\varphi \mid \phi_1\rangle + \sin\varphi \mid \phi_2\rangle \tag{10}$$

$$| 2p\ ^2E'(2)\rangle = -\sin\varphi \mid \phi_1\rangle + \cos\varphi \mid \phi_2\rangle \tag{11}$$

$| \phi_1\rangle$, $| \phi_2\rangle$ are solutions of the electronic wave equation with the same energy, which form another E' representation of the D_{3h} group. Thc phase φ is not determined by the variational method alone, and can have an arbitrary value. For two calculations with different inter-nuclear distances, the relative phase of these two electronic calculations is random, which in turn causes the x and y components of the transition dipole moments (**T31, T32,** and **T21**) to vary greatly (see Tables 6 and 7). Even so, the symmetry ensures that:

- The magnitudes of **T31, T32,** and **T21** do not depend on the phase φ and thus change smoothly with the inter-nuclear distance.
- $|$ T31 $| = |$ T32 $|$, $|$ T31(x) $| = |$ T32(y) $|$, and $|$ T31(y) $| = |$ T32(x) $|$

All of these features have been confirmed numerically by the results in Tables 6 and 7 and by Figures 4 and 5. Since the molecular properties are more sensitive to the quality of the wavefunction than the energy eigenvalues are, the results of the electric transition dipole moment calculations offer another strong indication that the wavefunctions we obtained are of good quality.

Our results for the electric transition dipole between the $2s\ ^2A_1'$ and $2p_z\ ^2A_2''$ states ($T43(z)$) show a very slow, smooth and monotonic variation with the size of the equilateral triangle. It is interesting to note that the value of this transition dipole moment is close to that between the $2s$ and $2p_z$ states of an isolated H atom (3.00 atomic units). The correlation diagram of Figure 1 shows that those two states dissociate into $H_2(X\ ^1\Sigma_g^+)$ +

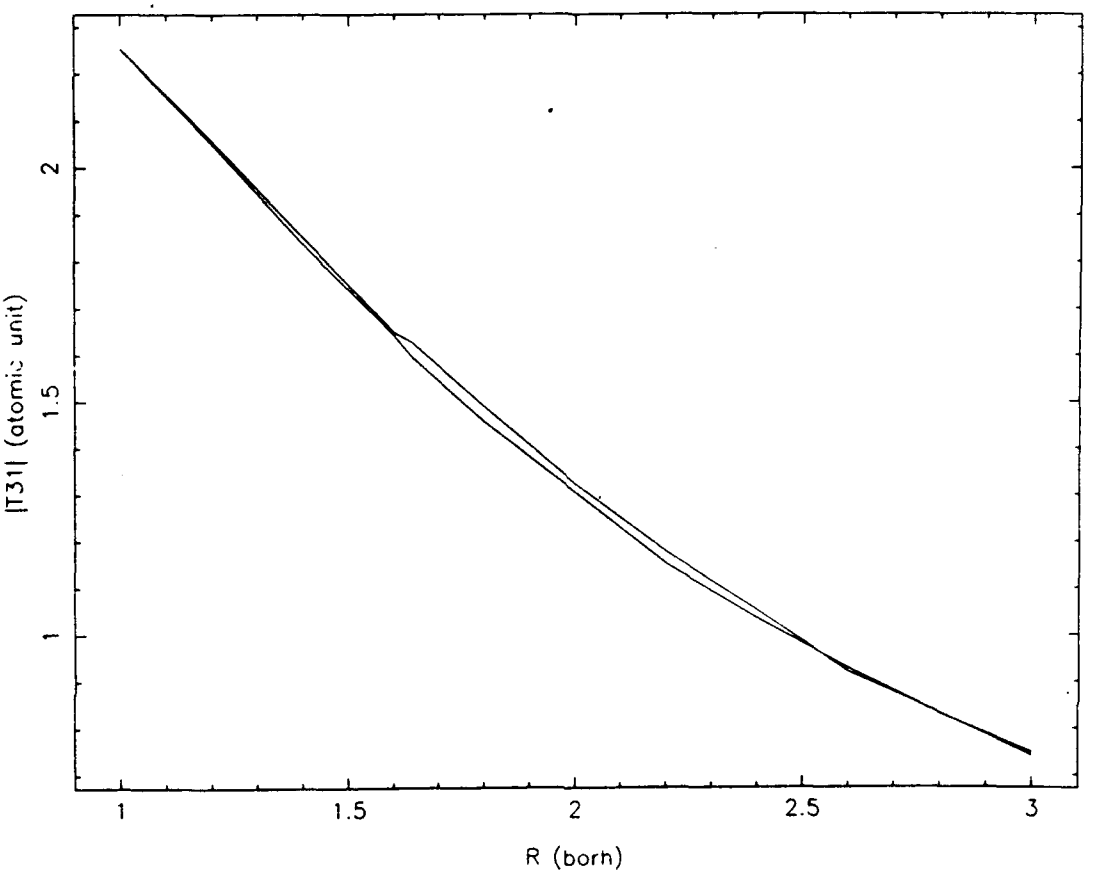

Figure 4: Length of the transition dipole moment **T31** for Equilateral H_3. R is the length of the side of the triangle. |**T31**| is the length of the **T31** transition dipole moment (see Tables 6-7 for the defination). The lower curve was obtained with the ($10s/8s$, $4p$) basis set used, and the upper one with the ($12s/7s$, $4p$, $1d$) basis set used.

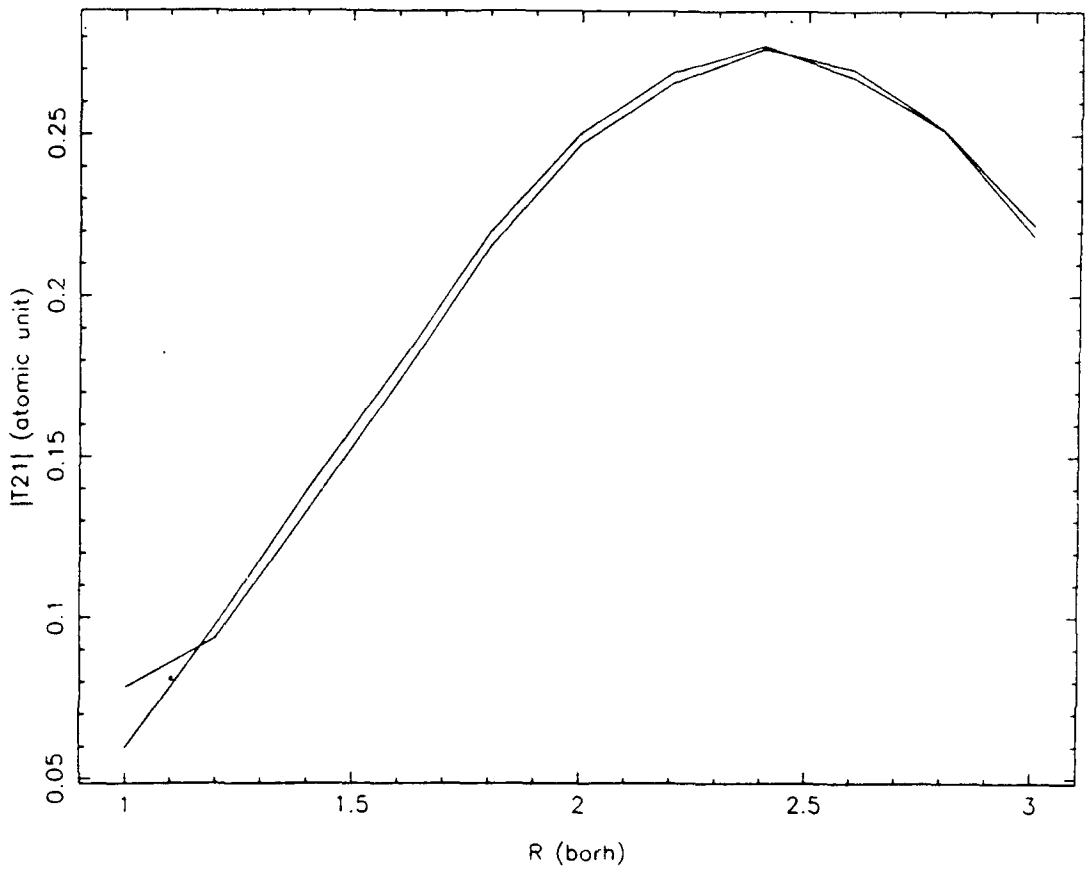

Figure 5: Length of the transition dipole moment **T21** for Equilateral H_3. R is the length of the side of the triangle. |**T21**| is the length of the **T21** transition dipole moment (see Tables 6-7 for the defination). The lower curve was obtained with the $(10s/8s,\ 4p)$ basis set used, and the upper one with the $(12s/7s,\ 4p,\ 1d)$ basis set used.

$H(2s)$ and $H_2(X\ ^1\Sigma_g^+)\ +\ H(2p_z)$ respectively, which should indeed furnish transition dipole moments around 3.00 *a.u.* As a result we can expect that this transition dipole moment will be more or less the same for all the nuclear geometries we are interested in. This turns out to be very important in making correct state assignments in our calculation.

At the equilateral triangular geometry with an inter-nuclear distance R = 1.64 bohr (corresponding approximately to the equilibrium geometry of the metastable H_3), we calculated the energy spacing between states $2s\ ^2A_1'$ and $2p\ ^2A_2''$ to be 1299 cm^{-1} with the larger basis set and 1374 cm^{-1} with the smaller one, while the best value previously calculated[32] is 1422 cm^{-1} and the experimentally estimated value[32] 1256 cm^{-1}. Both of our results for the electric transition dipole moments between these two states agree with the previous calculation[32] within one percent.

In Table 8, we present the results of of the energy calculations with the bond angle fixed at 60° and one bond length fixed at 10.0 bohr. Since the H atom is now far away from the H_2 diatomic molecule, we expect that these states of interest will correlate with dissociated states according to:

$$H_3(2p\ ^2E'(1)) \longrightarrow H_2(X\ ^1\Sigma^+) + H(1s) \tag{12}$$

$$H_3(2s\ ^2A_1') \longrightarrow H_2(X\ ^1\Sigma_g^+) + H(2s) \tag{13}$$

$$\longrightarrow H_2(X\ ^1\Sigma_g^+) + H(2p_x) \tag{14}$$

$$\longrightarrow H_2(X\ ^1\Sigma_g^+) + H(2p_y) \tag{15}$$

$$H_3(2p\ ^2A_2'') \longrightarrow H_2(X\ ^1\Sigma_g^+) + H(2p_z) \tag{16}$$

$$H_3(2p\ ^2E'(2)) \longrightarrow H_2(b\ ^3\Sigma_u^+) + H(1s) \tag{17}$$

Since the energies corresponding to the right side of Eqs 13, 14 and 15 are the same, we write Eqs 14 and 15 as a reminder that we must make the correct state assignments. The energy output listed in Table 8 confirms that the above equations describe the correct correlations (also see Figure 6). This is another indication that our GTO basis set is also appropriate for the H_2 molecule.

In the equilateral triangle geometry, the energy of the $2p\ ^2E'(2)$ state is below that of the $2s\ ^2A_1'$ state. However, for configurations in which H and H_2 are far away from each other, this is not generally true (see Figures 2, 3 and 6). The crossing of the corresponding potential energy surfaces increases the complexity of our calculation, because we have to be able to identify the states correctly, both for state assignment purposes and the correct calculation of the electric transition dipoles.

Table 8

Potential energies when H and H_2 are far away from each other[a].

	$2p\ ^2E'(1)$		$2p\ ^2E'(2)$		$2p_z\ ^2A_2''$	
R[a]	this work	KW[b]	this work	KW[c]	this work	KW[d]
1.2	-1.663260	-1.664934	-1.218675	-1.218964	-1.288093	-1.298934
1.4	-1.673015	-1.674474	-1.283682	-1.284150	-1.297616	-1.299474
1.6	-1.667196	-1.668580	-1.331255	-1.331724	-1.292109	-1.293580
1.8	-1.653721	-1.655067	-1.367693	-1.368291	-1.278657	-1.280067
2.0	-1.636826	-1.638132	-1.396762	-1.397064	-1.261499	-1.263131
3.0	-1.556159	-1.557312	-1.471696	-1.472010	-1.181171	-1.182312

a : One bond length is fixed at 10.0 Bohr. The bond angle is 60.0 degree.
R is the bond length of H_2 (in bohr).

b : Potential energy of $H_2(X\ ^1\Sigma_g^+)$ from W. Kolos and L. Wolniewicz[37] with the energy of $H(n=1)$ added.

c : Potential energy of $H_2(b\ ^3\Sigma_u^+)$ from W. Kolos and L. Wolniewicz[37] with the energy of $H(n=1)$ added.

d : Potential energy of $H_2(X\ ^1\Sigma_g^+)$ from W. Kolos and L. Wolniewicz[37] with the energy of $H(n=2)$ added.

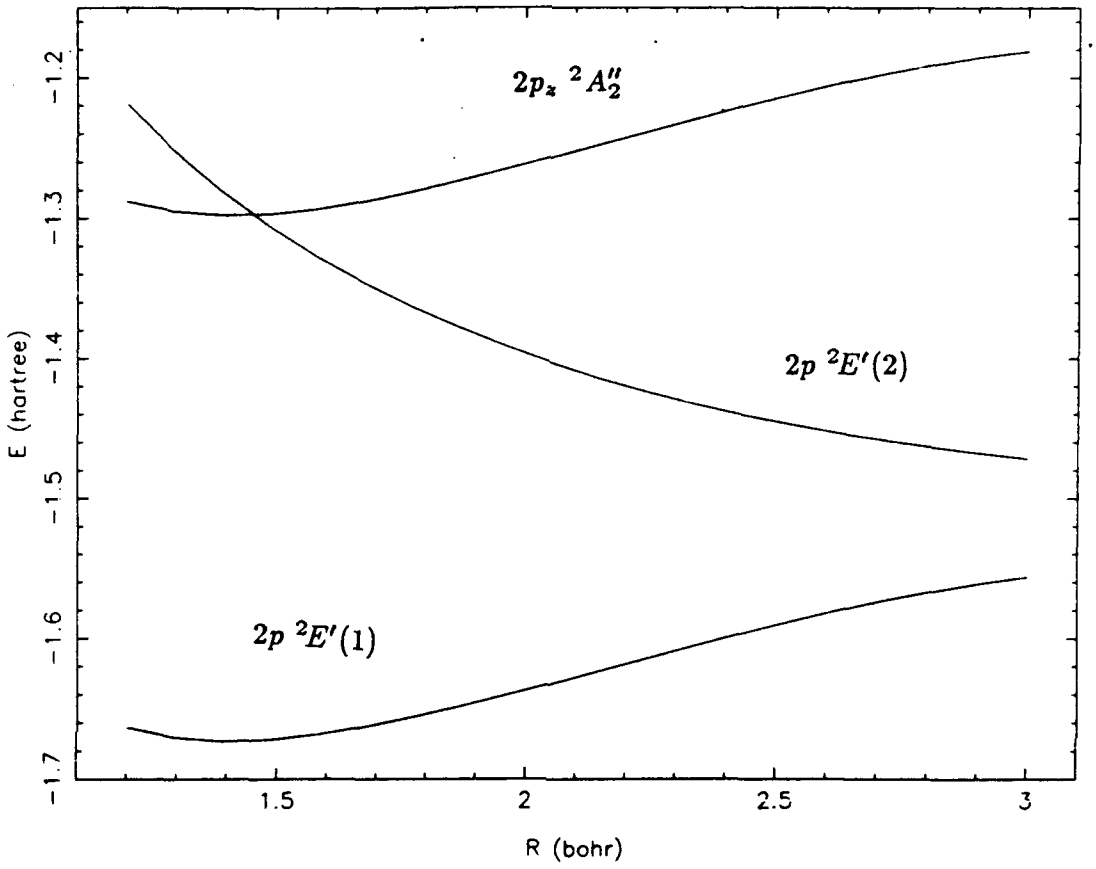

Figure 6: Potential Energy Curves for Asymmetric H_3. The geometry is defined in Table 8. R is the length of the smallest side of the triangle. The largest side of the triangle is 10.0 bohr and the bond angle between them is 60.0°. The $(12s/7s,\ 4p,\ 1d)$ basis set was used.

In order to map out the interesting part of the potential energy surfaces, we estimate that about 500 nuclear configurations with different shapes and sizes should be treated. We have at this moment about 95% of them done. After these calculations are finished, they will be fitted by a procedure developed previously[38] before being used in the bound and scattering states calculation of the nuclear motion.

The comparison between our *ab initio* results and these results from the functional extrapolation and double many body expansion (DMBE)[22] will permit us to check if this extrapolation is valid for nuclear configurations appreciably removed from equilateral triangular nuclear geometries. Recently, the $H + H_2$ system has been the subject of transition state spectroscopy (TSS) studies[39-42]. There are some theoretical calculations on the spectroscopy of the transition between the ground electronic state $2p\ ^2E'(1)$ and the excited electronic state $2p_z\ ^2A_2''$, but they are limited to either linear configurations or to $3D$ calculations using an *ad hoc* potential surface for the excited state and a constant electric transition dipole moments[43]. Our calculations of the excited surfaces and the nuclear geometry–dependent electric transition dipole moments between them will be very helpful for such theoretical studies of the transition state spectroscopy of the $H + H_2$ system.

3. Ro-vibrational Bound State Calculation for the Upper Manifold of the Electronic $2p\ ^2E'$ States of H_3

The next step towards the lifetime calculation is to obtain the ro-vibrational nuclear wavefunctions on the initial and final electronic potential surfaces. The $2p_z\ ^2A_2''$ state of H_3 supports bound ro-vibrational states which must be calculated. There are several methods for performing such calculations[44-48], most of which are based on the variational principle. A method of choice should have the following properties:

- It should be applicable to all nuclear geometries.
- It should be able to treat large vibrational amplitudes.
- It should be able to take advantage of special nuclear permutation symmetries of the triatomic system.
- It should be robust, and easy to use.

After a survey of the available methods, we chose the one developed by Tennyson and Sutcliffe[45]. Since the only previously calculated potential energy surface of H_3 which supports bound ro-vibrational states (neglecting its coupling to the ground state) is the upper manifold of the DMBE $2p\ ^2E'$ surface[22], we used it as a testing ground for the bound ro-vibrational state calculation. Because the conical intersection between this surface and the ground state one introduces the Molecular Aharonov-Bohm (MBA) effect[49-52] which needs special treatment, and since we also want to embed the correct P_3 nuclear permutation symmetry into the ro-vibrational wavefunction, we also developed a new hyperspherical coordinate propagation method which is very general and powerful. After obtaining the $2s\ ^2A_1'$ and $2p_z\ ^2A_2''$ potential energy surfaces, we will use those two methods to calculate the corresponding ro-vibrational states.

3.1 Variational Method

The coordinates used in the method of Tennyson and Sutcliffe are the scattering coordinates[45]. Let A_1, A_2, A_3 be the three atoms of the system, and (λ, ν, κ) be any cyclic permutation of (1, 2, 3). $\mathbf{r}_\lambda$ is the internuclear vector for the diatom $A_\nu A_\kappa$ and $\mathbf{R}_\lambda$ the vector of A_λ with respect to the center of mass of $A_\nu A_\kappa$. After separating the motion of the center of mass of these three atoms, the system can be described by six variables $(\alpha_\lambda,\ \beta_\lambda,\ \gamma_\lambda,\ R_\lambda,\ r_\lambda,\ \theta_\lambda)$. The three angles $(\alpha_\lambda, \beta_\lambda, \gamma_\lambda)$ are Euler angles, which describe the orientation of the tratomic molecule in space. r_λ and R_λ are the lengths of vectors $\mathbf{r}_\lambda$ and $\mathbf{R}_\lambda$ respectively and θ_λ is the angle between these two vectors.

A suitable symmetrized angular basis set for the variational calculation is chosen to

be:

$$|j,k\rangle = (1+\delta_{k,0})^{-1/2}\, 2^{-1/2}$$
$$\{\Theta_{j,k}(\theta_\lambda) D^J_{M,k}(\alpha_\lambda,\beta_\lambda,\gamma_\lambda) + (-1)^p \Theta_{j,-k}(\theta_\lambda) D^J_{M,-k}(\alpha_\lambda,\beta_\lambda,\gamma_\lambda)\} \qquad (18)$$

where $\delta_{k,0}$ equals 1 when $k = 0$ and zero otherwise. $D^J_{M,k}(\alpha_\lambda,\beta_\lambda,\gamma_\lambda)$ is the Wigner rotation function[53] and$\Theta_{j,k}(\theta_\lambda)$ is the associated Legendre function[54]. p is a quantum number that can assume the values 0 or 1. J is the total angular momentum quantum number, with M and k being the quantum numbers of its projections along the space-fixed z axis and the body-fixed z axis respectively. j is the angular momentum quantum number of the diatomic vector $\mathbf{r}_\lambda$. The Euler angules are chosen in such a way that the body-fixed z axis is along the $\mathbf{R}_\lambda$ direction and $\mathbf{r}_\lambda$ has a positive projection on the body-fixed x axis. (p, J, M) are constants of the motion for the system. The allowed values of j and k are:

$$k = (-J, -J+1, \ldots, J-1, J) \qquad (19)$$
$$j = (|k|, |k|+1, |k|+2, \ldots) \qquad (20)$$

The total parity of the spacial wavefunction under inversion through the system's center of mass is $(-1)^{J+p}$.

The basis functions for $(R_\lambda,\ r_\lambda)$ are chosen to be the analytic Morse oscillator-like functions:

$$\Psi_{m,n}(r_\lambda,\ R_\lambda) = \frac{1}{r_\lambda R_\lambda} H_m(r_\lambda) H_n(R_\lambda) \qquad (21)$$
$$m, n = \{0, 1, 2, 3, 4, \ldots\} \qquad (22)$$

where

$$H_n(r) = \beta^{1/2} N_{n,\alpha} \exp(-y/2) y^{(\alpha+1)/2} L^\alpha_n(y) \qquad (23)$$
$$A = \frac{4D}{\beta} \qquad (24)$$
$$\beta = \omega_e \left(\frac{\mu}{2D_e}\right)^{1/2} \qquad (25)$$
$$\alpha = \text{integer}(A) \qquad (26)$$
$$y = A\exp[-\beta(r - r_e)] \qquad (27)$$

$N_{n,\alpha} L^\alpha_n$ is the normalized associated Laguerre polynomial. r in Eq. 27 is either R_λ or r_λ. The parameters μ, r_e, ω_e and D_e are associated with the reduced mass, equilibrium separation, fundamental frequency and dissociation energy of the motion of coordinate r.

In practice r_e, ω_e, and D_e are usually treated as variational parameters and optimized accordingly.

It is difficult to embed the P_3 permutation symmetry of A_3-type molecules consisting of three identical nuclei in Tennyson's method. However, the P_2 permutation symmetry of AB_2-type molecules can be easily built in[45] (also see Eq. 18). Since the potential energy function of such a molecule is invariant under an interchange of these two B atoms, the Hamiltonian does not couple the angular basis functions of even j with angular basis functions of odd j, and we can treat these two cases separately[45].

If we treat an A_3-type system with only the P_2 symmetry embedded into the basis set functions, the final converged result should still satisfy the P_3 symmetry. The symmetry would manifest itself in the structure of the eigenenergy levels and in the shape of the eigenfunctions plotted in a set of appropriately symmetrized coordinates. If an eigenstate obtained from the even basis set is nondegenerate, it must belong to an A_1 irreducible representation of P_3. If an eigenstate obtained from the odd basis set is nondegenerate, then it generates an A_2 irreducible representation of P_3. If one eigenstate from the even basis set and one eigenstate from the odd basis set are degenerate with each other, they must belong to an E irreducible representation of P_3.

The Tennyson-Sutcliffe (TS) method has some nice properties. It does not depend on special molecular geometries[44], and is applicable to motions with large vibrational amplitude. The choice of known analytic basis functions makes it possible to obtain most parts of the Hamiltonian matrix elements analytically and thereby save an appreciable amount of computation time. The only computation–intensive part of the calculation is the diagonolization of the Hamiltonian matrix.

Numerical details and results

The code we used for the variational state calculation is called TRIATOM, and was obtained from the CPC Program Library of Queen's University, Belfast, Northern Ireland[45]. We initially made small test runs on Sun workstations and a micro VAX. The major part of the calculations was done on the SCS-40 mini-supercomputer of the San Diego Supercomputer Center (SDSC).

The ro-vibrational motion of the H_3^+ ion has been treated by Tennyson *et al.* [55–57]. Since this molecule has some resemblance with the H_3 system in which we are interested, we repeated part of the calculation for H_3^+ with total angular momentum $J = 0$ for gaining experience with this code. We adopted the same values of the parameters r_e, ω_{r_e}, D_{r_e}, R_e, ω_{R_e} and D_{R_e} used previously[55–56], which are listed in Table 9. The

Table 9

Optimized parameters of the Morse–like functions in R_λ and r_λ for H_3^+ with $J = 0$.

	$D_e(au)$	$\omega_e(au)$	$r_e(au)$
$J = 0$	0.230 [a]	0.0085 [a]	1.71 [a]
$J = 0$	0.205 [b]	0.0118 [b]	2.10 [b]

a: Parameters for the Morse–like functions in R_λ.

b: Parameters for the Morse–like functions in r_λ.

H_3^+ potential surface used in our calculation is that included in the TRIATOM package for code testing[58]. It is different from the one used in previous publications[55-57]. As a consequence, our results should not be in perfect agreement with the latter. The convergence test and the final results are listed in Tables 10 and 11, which show that the lowest ten states are well converged, with the size of the largest basis set being the same as that used previously[55-57].

For H_3, the only currently available potential energy surface which supports bound ro-vibrational states of nuclear motion is the upper manifold of the DMBE surfaces[22] for the $2p\ ^2E'$ electronic states, if coupling between these two manifolds is neglected. We calculated the ro-vibrational bound states with total angular momenta $J = 0$ and 1.

Initially we used small sets of basis functions to optimize the r_e, ω_{r_e}, D_{r_e}, R_e, ω_{R_e} and D_{R_e} parameters. Since it had been showed previously that the optimized parameters for even j basis are more or less the same as those for odd j basis[45], we only did the optimization for the even j basis calculation. This optimization was done with the basis set defined to be $m_{max} = 8$, $n_{max} = 8$, $j_{max} = 16$, and $N_{total} = 576$ for $J = 0$, and $m_{max} = 6$, $n_{max} = 6$, $j_{max} = 15$, and $N_{total} = 382$ for $J = 1$. For the case of $J = 0$, we put the emphasis on the lower 5 states, while for $J = 1$ we considered the average effect of the parameter tuning on the lower 12 states. Because the optimization process is actually done manually, in a finite range of the six dimensional parameter space, with limited guidance from physical considerations of Eqs. 23 to 27, it is possible that a local minimum may be accepted as the global minimum since there is no sure indication that the global minimum has been reached. Fortunately, the larger the basis set, the less sensitive the results are to changes of those parameters. The results of the optimized parameters are listed in Table 12.

We then increased the size of the basis set and tested the results for convergence. We analyzed the importance of each basis function for a given basis size carefully, and let the results guide us to achieve an efficient way of increasing the size of the basis set. The convergence test results for the H_3 molecule are listed in Table 13, which shows that the energy levels are not well converged as for H_3^+. In general the lower states are better converged than the upper ones. The calculation turned out to be limited by the amount of computer memory we could access at that time, which was 3 Mwords. The final results for H_3 are listed in Table 14, with the sizes of basis set in the range of 1100 to 1600 and SCS-40 CPU times ranging from 10 minutes to 30 minutes. The results agree with those from the hyperspherical coordinate propagation method well, as discussed in the next section.

One of the most important reasons why we need such a large basis set for the H_3

Table 10

Convergence test of H_3^+ with $J = 0$ and even j basis functions for the lower ten states[a,b].

H_3^+, with $J = 0$ and even j basis functions		
m=9, n=7, L=14 N = 340	m=10, n=8, L=14 N = 616	m=11, n=8, L=18 N = 880
-7.067955	-7.067967	-7.067977
-6.816079	-6.816119	-6.816119
-6.750378	-6.750436	-6.750437
-6.590602	-6.590784	-6.590786
-6.567921	-6.568055	-6.568060
-6.512097	-6.512965	-6.512967
-6.441278	-6.441708	-6.441708
-6.367264	-6.367514	-6.367530
-6.338421	-6.338839	-6.338893
-6.290215	-6.290872	-6.290870

a : The unit of energy is 10^4 cm^{-1}.

b : See reference 45 for the definitions of (m, n, L) and N.

Table 11: H_3^+ $J = 0$ bound state energies[a].

Even basis			Odd basis	
Tennyson's[b] results	present[c] results	Symmetry	Tennyson's[b] results	present[c] results
0.00000	0.00000	A_1		
0.24944	0.25185	E	0.24943	0.25139
0.31911	0.31753	A_1		
0.47250	0.47718	A_1		
0.49583	0.49991	E	0.49580	0.49990
0.55453	0.55500	E	0.55449	0.55485
0.62768	0.62626	A_1		
0.69444	0.70044	A_1		
0.72350	0.72907	E	0.69433	0.70030
		A_2	0.74513	0.75069
0.77403	0.77710	A_1		

a: The energy is in 10^4 cm^{-1} and its origin is the ground state energy.

b: See references 55–57.

c: See text and reference 58.

Table 12

Optimized parameters of the Morse–like functions in R_λ and r_λ for H_3 with $J = 0$ and $J = 1$.

	$D_e(au)$	$\omega_e(au)$	$r_e(au)$
$J = 0$	0.230 [a]	0.0130 [a]	1.96 [a]
$J = 1$	0.262 [a]	0.0100 [a]	2.01 [a]
$J = 0$	0.262 [b]	0.0122 [b]	2.09 [b]
$J = 1$	0.232 [b]	0.0102 [b]	2.32 [b]

a: Parameters for the Morse–like functions in R_λ.

b: Parameters for the Morse–like functions in r_λ.

Table 13

Convergence test of H_3 with $J = 0$ and even j basis functions for the lower ten states[a,b].

H_3, with $J = 0$ and even j basis functions		
m=15, n=13, L=16 N = 757	m=16, n=13, L=18 N = 1067	m=19, n=19, L=26 N = 1368
-0.824614	-0.826261	-0.827333
-0.662336	-0.664153	-0.665618
-0.512776	-0.514696	-0.516372
-0.376072	-0.377987	-0.379855
-0.369457	-0.369877	-0.370206
	-0.253486	-0.256018
	-0.236860	-0.237305
	-0.134838	-0.140441
	-0.119736	-0.120358
	-0.049332	-0.053411

a : The unit of energy is 10^4 cm^{-1}.

b : See reference 45 for the definitions of (m, n, L) and N.

Table 14

Bound state energies without consideration of the geometric phase[a].

$J = 0^b$			$J = 1$ even parity[b]			$J = 1$ odd parity[c]		
3.7210	A_1	3.7218	3.7282	A_2	3.7294	3.7264	E	3.7276
3.9216	A_1	3.9223	3.9284	A_2	3.9297	3.9266	E	3.9281
4.1067	A_1	4.1073	4.1130	A_2	4.1145	4.1114	E	4.1131
4.2759	A_1	4.2766	4.2817	A_2	4.2839	4.2802	E	4.2831
4.4282	A_1	4.4301	4.4336	A_2	4.4386	4.4322	E	4.4398
4.5621	A_1	4.5734	4.5665	A_2	4.5803	4.5656	E	4.5894
4.2886	E	4.2886	4.2955	E	4.2956	4.2971	A_1	4.2975
						4.2969	A_2	4.2972
						4.2904	E	4.2908
4.4533	E	4.4533	4.4596	E	4.4598	4.4610	A_1	4.4618
						4.4608	A_2	4.4615
						4.4550	E	4.4557
4.5980	E	4.5983	4.6036	E	4.6048	4.6049	A_1	4.6083
						4.6047	A_2	4.6093
						4.5996	E	4.6028
4.7212	E		4.7261	E	4.7349	4.7272	A_1	4.7370
						4.7270	A_2	4.7355
						4.7225	E	
4.6806	A_1	4.6813	4.6871	A_2	4.6893	4.6842	E	4.6878

a: The energy is in eV and its origin corresponds to the bottom of the ground electronic state of the isolated H_2 molecule.

b: The left column gives the results of the hyperspherical coordinate propagation method and the right column the TS method results. The central column gives the irreducible representation of the permutation group of the nuclei to which the spacial part of the nuclear wavefunction belongs.

system is that the upper manifold of the H_3 $2p\ ^2E'$ surface has a cone-shape structure with a sharp tip at the equilateral triangle nuclear geometry, while the H_3^+ surface has a nice smooth round shape instead. The Morse-type basis set functions are good for representing the harmonic-like oscillation of the H_3^+ ion. However they are not good for representing the motion on such a conically shaped surface. As a result, more basis functions are needed to obtain converged results H_3 than for H_3^+, if the same degree of convergence is required. For the $2s\ ^2A_1'$ and $2p_z\ ^2A_2''$ electronic states, the H_3 is really like a H_3^+ core plus a Rydberg electron in $2s$ and $2p_z$ states respectively, which interact weakly with the H_3^+ core. For this reason the shapes of the potential energy surfaces of those two electronic states should be similar to that of the H_3^+ in its ground electronic state. This suggests that a small basis sets (of size about 800) should give converged results for the $2s\ ^2A_1'$ and $2p_z\ ^2A_2''$ potential energy surfaces.

Finally, let us consider the shapes of the ro–vibrational wavefunctions to see if the final converged calculations yield wavefunctions with the right P_3 symmetry. We ploted the wavefunctions in a system of symmetrized coordinates[59]. Figure 7 contains contour lines of the wavefunctions for H_3^+ with total angular momentum $J = 0$ and basis set size N=880, and Figure 8 for H_3 with $J = 0$ and basis set size N=1363. The plots show that the wavefunctions do not display P_3 (*i.e.*, C_{3v}) symmetry, even for the highly converged state of H_3^+. The reason for this behavor is that in general, the convergence of the eigenvector is poorer than that of the eigenvalue in a numerical eigenvalue-eigenvector problem. In order to get the right symmetry with a reasonable basis set size, the symmetry has to be embeded into this basis set before the variational calculation is performed. This is difficult to do with Tennyson's code, so we developed a new method to achive this, which is described in section 3.2.

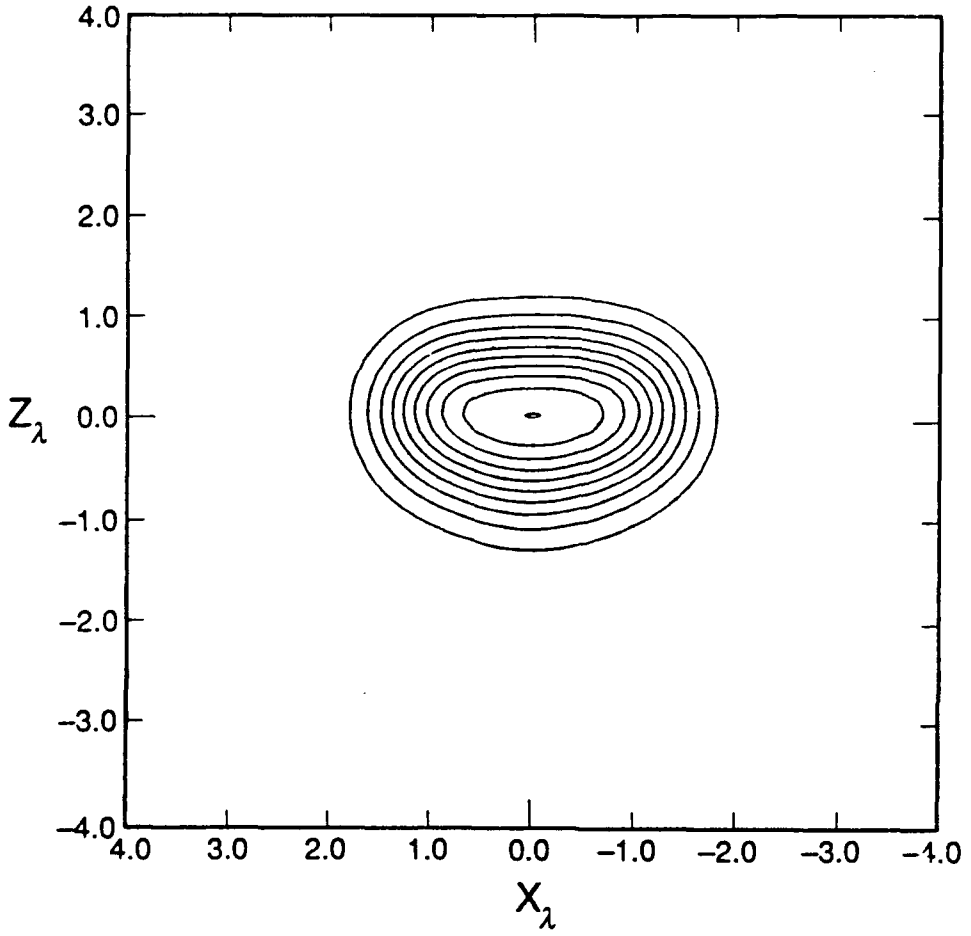

Figure 7: Contour plot of the wavefunction Ψ for the lowest $J = 0$, A_1-type H_3^+ ro-vibrational state, in symmetrized hyperspherical coordinates[59]. Depicted is a cut at constant Y_λ chosen to be 2.1 bohr, for which the potential energy function of H_3^+ has a minimum (at $X_\lambda = Z_\lambda = 0$). The maximum (near the center of the plot) of the wavefunction was set equal to 1.0, and contours for $\Psi = 0.9$ to 0.1 in steps of 0.1 are displayed. The X_λ and Z_λ coordinates are in bohr.

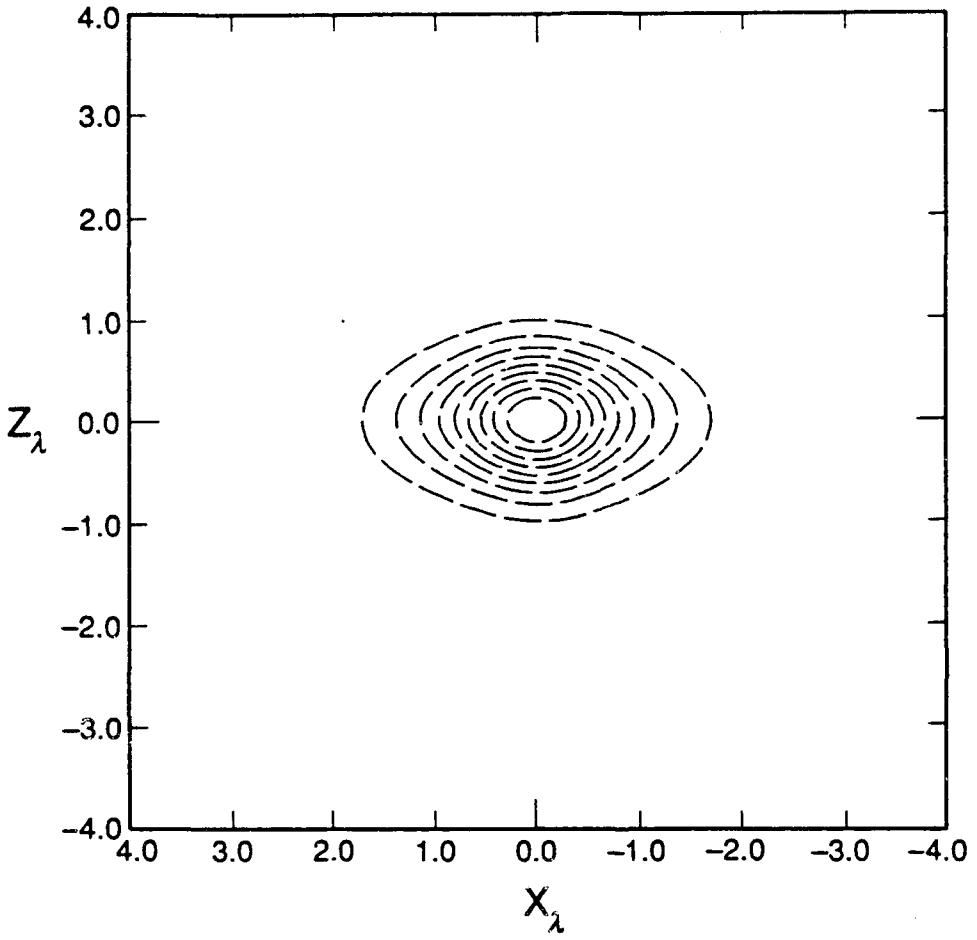

Figure 8: Contour plot of the wavefunction Ψ for the lowest $J = 0$, A_1-type H_3 ro-vibrational state, in symmetrized hyperspherical coordinates[59]. Depicted is a cut at constant Y_λ chosen to be 1.967 bohr, for which the potential energy function of H_3 has a minimum (at $X_\lambda = Z_\lambda = 0$). The maximum (near the center of the plot) of the wavefunction was set equal to 1.0, and contours for $\Psi = 0.9$ to 0.1 in steps of 0.1 are displayed. The X_λ and Z_λ coordinates are in bohr.

3.2 Hyperspherical Coordinate Propagation Method

The hyperspherical coordinate approach has been successfully used in recent years for the calculation of bound ro-vibrational[60-61] and scattering[62-67] states of triatomic systems. Our motivations of using it to study the bound ro-vibrational motion of H_3 in its upper manifold of the electronic $2p\ ^2E'$ states are three-fold:

1. The full P_3 nuclear permutation symmetry of the identical triatomic system can be easily embedded into the basis set functions so that the final wavefunctions of the ro-vibrational states will have the correct symmetry. This, as seen in the previous section, is difficult to achieve with the Tennyson-Sutcliffe variational method.

2. The ground electronic state $2p\ ^2E'(1)$ of H_3 has a conical intersection with the first excited electronic state $2p\ ^2E'(2)$ at equilateral triangle nuclear configurations[19,22]. The Born-Oppenheimer real electronic wavefunctions undergo a sign change when one follows a close path in nuclear configuration space around the line along which the two states conically intersect[19,22,49-52]. Since the total electro-nuclear wavefunction is continuous and single valued, there has to be a compensating sign change on the nuclear part of the wavefunction[49-52]. This is referred to in the literatures as the Molecular Aharonov–Bohm (MAB) effect[51-52]. This effect will modify the energy levels of the bound ro-vibrational states of the upper electronic state $2p\ ^2E(2)$ which would exist in the absence of interaction with the ground state. It is easy to take this MAB effect into account with the symmetrized hyperspherical coordinate propagation method described below, while this is not possible with the TS variational method in its present format. Our results should help to solve the controversy as to whether these ro-vibrational bound states have been experimentally detected or not[2-4].

3. The corresponding wavefunctions will be needed to calculate the overlap integrals with the ground state scattering wavefunctions (see Eqs. 1 and 2). Since we calculate the latter using hyperspherical coordinates, it makes sense to obtain the bound state wavefunctions with the same coordinates.

In the absence of coupling between these two electronic states, the excited $2p\ ^2E'(2)$ surface should support bound ro-vibrational states. Initially, without including the MBA effect, we computed those states using a symmetrized hyperspherical coordinate propagation method, and compared the results with those of the variational method (TS), for total angular momentums $J = 0$ and $J = 1$. Then we did the calculation including the MAB effect, and obtained completely different energy levels[68]. The MAB effect also modifies the scattering calculation in $H + H_2$ system[69].

The Method

Let $A_\alpha, A_\beta, A_\gamma$ be the atoms of the system, and (λ, ν, κ) be any cyclic permutation of (α, β, γ). $\mathbf{r}_\lambda$ is the mass-scaled[70] internuclear vector for the diatom $A_\nu A_\kappa$ and $\mathbf{R}_\lambda$ the mass-scaled vector of A_λ with respect to the center of mass of $A_\nu A_\kappa$. The hyperspherical method uses the hyper-radius $\rho = (R_\lambda^2 + r_\lambda^2)^{\frac{1}{2}}$ to describe the global size of the triatomic system and a set of five angles ς to describe its shape and orientation in space[62-67,70]. In the Born-Oppenheimer approximation, the electro-nuclear wavefunction can be written as a product of the electronic part ψ_e, which we choose to be real, and the nuclear part. The latter can be factored into a nuclear spin part and a spatial part $\psi^{JM\Pi\Gamma}$. J is the total nuclear angular momentum quantum number, M its projection onto a laboratory-fixed z axis, Π the parity with respect to inversion of the nuclear coordinates through their center of mass and Γ the irreducible representation of the nuclear permutation group (P_3) to which $\Psi^{JM\Pi\Gamma}$, the electro-nuclear wavefunction excluding the nuclear spin part, belongs:

$$\Psi^{JM\Pi\Gamma} = \psi^{JM\Pi\Gamma}(\rho, \varsigma)\psi_e(\vec{q}_e; \rho, \varsigma) \tag{28}$$

$\vec{q}_e$ refers to the set of all electronic coordinates (spacial and spin). $\psi^{JM\Pi\Gamma}$ is an eigenfunction of the nuclear motion Hamiltonian

$$H = -\frac{\hbar^2}{2\mu}\rho^{-5}\frac{\partial}{\partial\rho}\rho^5\frac{\partial}{\partial\rho} + \frac{\hat{\Lambda}^2}{2\mu\rho^2} + V(\rho, \varsigma) \tag{29}$$

where μ is the three-body reduced mass, $\hat{\Lambda}$ the grand canonical angular momentum and V the Born-Oppenheimer electronic potential energy function. The nuclear function $\psi^{JM\Pi\Gamma}$ is expanded in a basis of local hyperspherical surface functions (LHSF) $\Phi_n^{JM\Pi\Gamma}$:

$$\psi^{JM\Pi\Gamma}(\rho, \varsigma) = \frac{1}{\rho^{\frac{5}{2}}}\sum_n F_n^{J\Pi\Gamma}(\rho; \bar{\rho})\Phi_n^{JM\Pi\Gamma}(\varsigma; \bar{\rho}) \tag{30}$$

The LHSF are defined as the eigenfunctions of the nuclear Hamiltonian at fixed hyperradius $\bar{\rho}$:

$$[\frac{\hat{\Lambda}^2}{2\mu\bar{\rho}^2} + V(\bar{\rho}, \varsigma)]\Phi_n^{JM\Pi\Gamma}(\varsigma; \bar{\rho}) = \epsilon_n^{J\Pi\Gamma}(\bar{\rho})\Phi_n^{JM\Pi\Gamma}(\varsigma; \rho) \tag{31}$$

The coefficients $F_n^{J\Pi\Gamma}$ in Eq. 30 are solutions of a set of coupled differential equations in ρ, which we solve using piece-wise diabatic bases[62-67]. For assumed values of the rovibrational energies, the solutions are propagated forward and backward from small and large ρ values where they have negligible amplitudes. The energy is scanned iteratively until the forward and backward solutions match smoothly at an intermediate value of ρ.

In the present study, we use the Whitten–Smith[71-72] definition of the five angular coordinates ς as modified by Johnson[73]. Three Euler angles $(\alpha\beta\gamma)$ specify the orientation of the body frame in space. The axes of this frame lie along the principle axes of inertia. The Z axis is parallel to $\mathbf{r}_\lambda \times \mathbf{R}_\lambda$ and the X axis is associated to the smallest moment of inertia and is oriented such that $r_{\lambda X} \geq 0$. Two angles $(\theta, \varphi_\lambda)$ describe the shape of the molecular triangle and are defined by:

$$r_{\lambda X} = \rho\cos(\frac{\pi}{4} - \frac{\theta}{2})\sin(\frac{\varphi_\lambda}{2}) \tag{32}$$

$$r_{\lambda Y} = -\rho\sin(\frac{\pi}{4} - \frac{\theta}{2})\cos(\frac{\varphi_\lambda}{2}) \tag{33}$$

$$R_{\lambda X} = \rho\cos(\frac{\pi}{4} - \frac{\theta}{2})\cos(\frac{\varphi_\lambda}{2}) \tag{34}$$

$$R_{\lambda Y} = \rho\sin(\frac{\pi}{4} - \frac{\theta}{2})\sin(\frac{\varphi_\lambda}{2}) \tag{35}$$

The ranges for these angles are $0 \leq \theta \leq \frac{\pi}{2}$ and $0 \leq \varphi_\lambda \leq 2\pi$. $\theta = 0$ corresponds to the symmetric top configuration (an equilateral triangle for three identical particles) in which the principal axes of inertia X and Y are undefined.

The grand canonical angular momentum is given explicitly by[67-69]:

$$\begin{aligned}\hat{\Lambda}^2 = &-4\hbar^2\{\frac{1}{\sin 2\theta}\frac{\partial}{\partial\theta}\sin 2\theta\frac{\partial}{\partial\theta} + \frac{1}{\sin^2\theta}\frac{\partial^2}{\partial\varphi_\lambda^2}\} + \frac{4i\hbar\cos\theta}{\sin^2\theta}\hat{J}_Z\frac{\partial}{\partial\varphi_\lambda} \\ &+ \frac{2[\hat{J}^2 - \hat{J}_Z^2]}{\cos^2\theta} + \frac{\hat{J}_Z^2}{\sin^2\theta} + \frac{\sin\theta}{\cos^2\theta}[\hat{J}_+^2 + \hat{J}_-^2]\end{aligned} \tag{36}$$

where $\hat{J}_Z$ is the body-fixed Z component of the total angular momentum $\hat{J}$, and $\hat{J}_\pm = \hat{J}_X \pm i\hat{J}_Y$.

Eq. 31 is solved variationally by expansion in a body-fixed basis $\chi_{n_\theta n_\varphi}^{JMK}$ built with products of simple analytical functions[66] :

$$\chi_{n_\theta n_\varphi}^{JMK} = e^{in_\varphi\varphi_\lambda} f_{n_\theta}(\theta) D_{MK}^J(\alpha\beta\gamma) \tag{37}$$

D_{MK}^J is a Wigner rotation matrix[53] and n_φ is integer or half of an odd integer. $f_{n_\theta}(\theta)$ are simple trigonometric functions, such that the LHSF have correct behaviors near the singularities of the kinetic energy operator $\theta = 0$ and $\frac{\pi}{2}$. In practice, the f_{n_θ} can be chosen as the functions $\cos(n_\theta\theta)$ or $\sin(n_\theta\theta)$, with n_θ integer or half odd integer, in terms of which the hyperspherical harmonics (whose θ dependence is usually written as a polynomial in $\cos(\theta)$) can be written.

We now focus attention on the special case of three identical nuclei and describe how to build electro-nuclear wavefunctions $\Psi^{JM\Pi\Gamma}$ which are bases for the irreducible representations of the permutation group of the nuclei (P_3). The operations of this group correspond to simple changes in φ_λ (which are related to the isomorphism between P_3 and C_{3v}) as indicated in Table 15. If $\epsilon^e_{\nu\kappa}(=\pm 1)$ is the symmetry of the electronic wavefunction with respect to the $\nu \leftrightarrow \kappa$ permutation, then the linear combinations defined by

$$\chi^{JMK\epsilon^{en}_{\nu\kappa}}_{n_\theta|n_\varphi|} = \chi^{JMK}_{n_\theta|n_\varphi|} + \epsilon^{en}_{\nu\kappa}\epsilon^{e}_{\nu\kappa}(-1)^{J+K+2n_\varphi}\chi^{JM,-K}_{n_\theta,-|n_\varphi|} \tag{38}$$

give electro-nuclear wavefunctions $\Psi^{JM\Pi\Gamma}$ (Eq. 28) having $\epsilon^{en}_{\nu\kappa}(=\pm 1)$ symmetry with respect to the $\nu \leftrightarrow \kappa$ permutation.

If there is no conical intersection between electronic states, the electronic wavefunction $\psi_e(\vec{q}_e;\rho,\varsigma)$ belongs to a one dimensional representation of the nuclear permutation group (A_1 for $\epsilon^e_{\nu\kappa} = +1$, or A_2 for $\epsilon^e_{\nu\kappa} = -1$). Table 16 indicates how the total angular momentum, the parity and the irreducible representation Γ of P_3 to which $\Psi^{JM\Pi\Gamma}$ belongs determines the set of quantum numbers n_φ.

The hyperspherical method uses 20 n_θ values, between 4 (A_1 or A_2 symmetry) and 8 (E symmetry) $|n_\varphi|$ values (Eqs. 37 and 38), and between 6 (A_1 or A_2 symmetry) and 12 (E symmetry) LHSF (Eqs. 30 and 31). The LHSF have been computed at typically 50 $\bar{\rho}$ values between 1.5 bohr and 6.5 bohr. The convergence of the LHSF and rovibrational energies is of the order of 10^{-4} eV. The compactness of the hyperspherical expansion comes from the fact that the potential energy around the Y_λ axis ($\theta = 0$) is nearly cylindrical (small number of $n_{|\varphi|}$ values) and from the steep increase of the the potential as a function of θ (small number of LHSF).

Results and Conclusions

Figure 9 illustrates the main features of the electronic potential energy surface in an internal configuration space[59]. The energy levels obtained from the calculation in the hyperspherical coordinates are converged to within 1 cm^{-1}, and are very close to those gotten by using the **TS** variational method, with the former one more converged and more accurate. The hyperspherical coordinates propagation method makes the symmetry assignment of these levels much easier. Table 14 compares the ro-vibrational energy levels obtained by these two methods excluding the MAB effect. Table 17 gives the energy levels when the MAB effect is included, obtained from the hyperspherical coordinate propagation method only. Comparison between Tables 14 and 17 shows that this effect is very important. Figure 10 is the graphic representation of Tables 14 and 17. (μ_1, μ_2, l) are the quantum numbers assigned to those states[68].

Table 15

Effect of permutations of the nuclei on the angle φ_λ.

Permutation	$P_{\lambda\nu\kappa}$ [a]	$P_{\nu\kappa\lambda}$ [b]	$P_{\kappa\lambda\nu}$ [c]	$P_{\nu\kappa}$ [d]	$P_{\lambda\nu}$ [d]	$P_{\lambda\kappa}$ [d]
Value of φ_λ [e]	φ_λ	$\varphi_\lambda + \frac{2\pi}{3}$	$\varphi_\lambda + \frac{4\pi}{3}$	$2\pi - \varphi_\lambda$	$\frac{2\pi}{3} - \varphi_\lambda$	$\frac{4\pi}{3} - \varphi_\lambda$

a : $P_{\lambda\nu\kappa}$ is the identity permutation.
b : $P_{\nu\kappa\lambda}$ refers to the cyclic permutation $\lambda\nu\kappa \longrightarrow \nu\kappa\lambda$.
c : $P_{\kappa\lambda\nu}$ refers to the cyclic permutation $\lambda\nu\kappa \longrightarrow \kappa\lambda\nu$.
d : P_{ij} refers to the pairwise permutation of nuclei i and j.
e : The changes in φ_λ are true modulo 2π, since φ_λ must remain in the range $[0,2\pi]$.

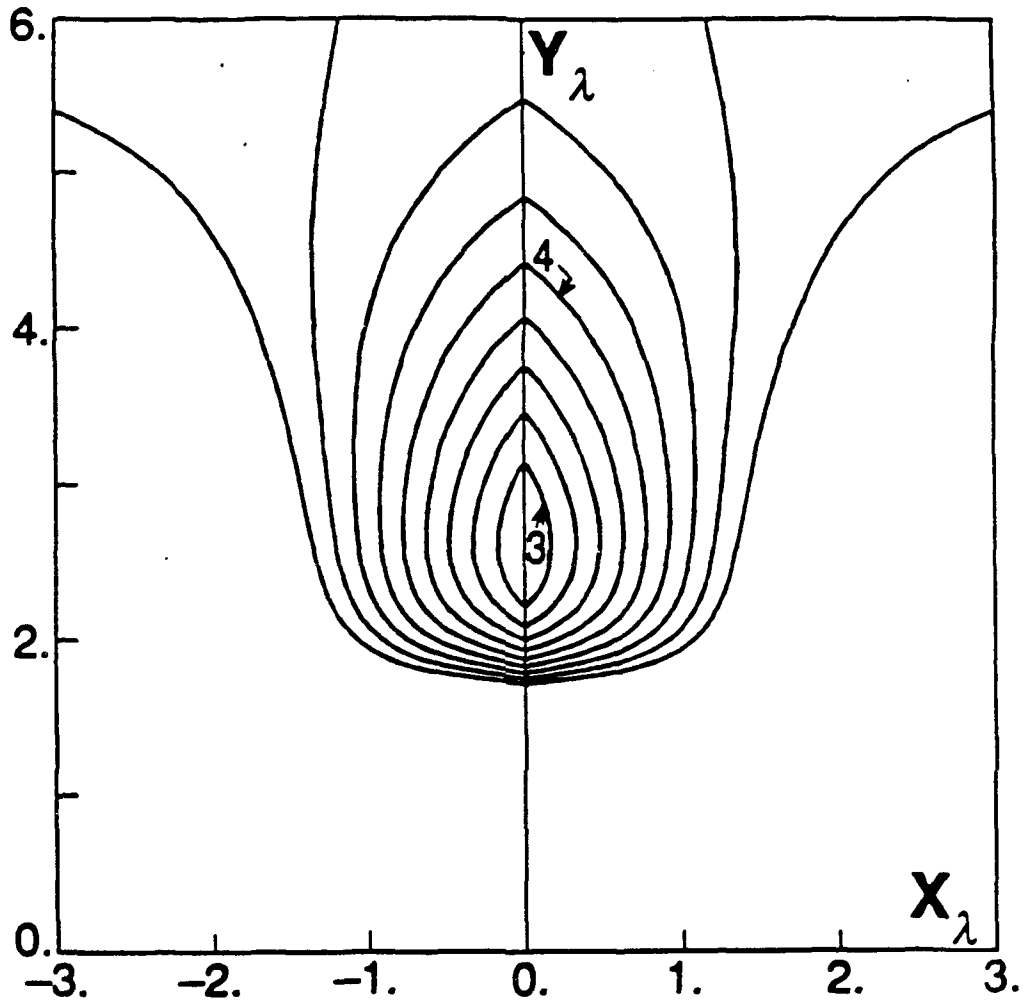

Figure 9: The two dimensional plot of the upper sheet of the DMBE potential surfaces[22]. The hyperspherical coordinates are used[59]. The Z_λ value is zero. The conical intersection of those two electronic states happens along the Y_λ axis. The equipotentials are equally spaced by 0.25 eV from 3.0 eV to 5.0 eV. X_λ and Y_λ are given in bohr.

Table 16

Choice of n_φ for each parity Π and irreducible representation Γ of the nuclear permutation group P_3.

Π	Γ [c]	n_φ
Even,without phase[a] Odd,with phase[b]	A_1/A_2 E	$3m$[d] $3m \pm 1$[d]
Even,with phase[b] Odd,without phase[a]	A_1/A_2 E	$3m + \frac{3}{2}$[d] $3m \pm \frac{1}{2}$[d]

a : without consideration of the geometric phase due to the conical intersection.
b : with consideration of the geometric phase due to the conical intersection.
c : Γ is the irreducible representation of P_3 to which $\Psi^{JM\Pi\Gamma}$ belongs.
d : m is a non-negative integer.

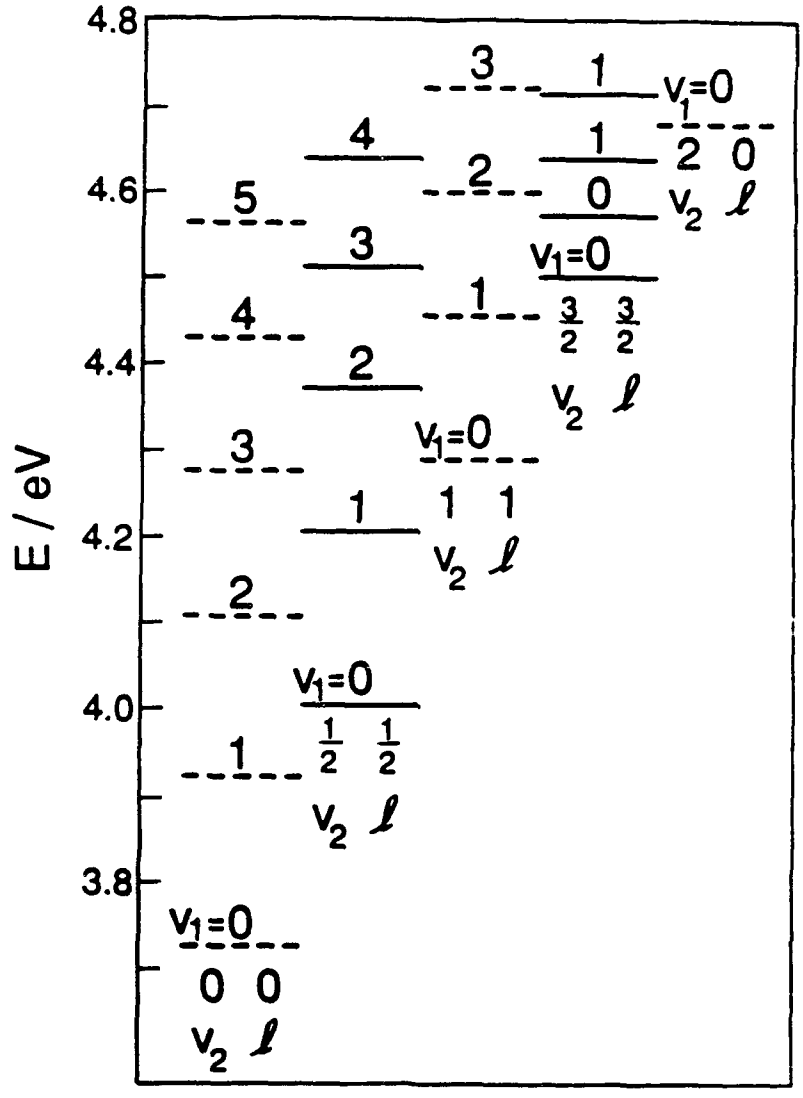

Figure 10: Ro-vibronic energy levels associated to the upper sheet of the DMBE potential surfaces of H_3[22]. The full lines are the levels including the effect of the geometric phase while the dashed ones exclude that effect. The quantum numbers v_1, v_2 and l are defined in reference 68. The origin for the energy scale is the bottom of the isolated ground electronic H_2 potential energy curve. These levels are for the $J = 0$ states, but the $J = 1$ levels are nearly degenerate with them, the splitting being of the order of 10^{-2} eV. Their nuclear permutation symmetries depend on J and on the parity Π, as well as whether the geometric phase is or is not included (see Table 15 and Table 16). There are two levels for each of the sets of quantum numbers $(v_1 = 0, v_2 = l = \frac{3}{2})$ and $(v_1 = 1, v_2 = l = \frac{3}{2})$, which would be degenerate if the potential were exactly cylindrically symmetric around the Y_λ axis (see text and Figure 9).

We have described in this section a new hyperspherical coordinate propagation method for the calculation of bound ro-vibrational states of triatomic system. This method is well adapted to systems of three identical particles, because it allows easy inclusion of the full permutation symmetry of the system and of the effect of conical intersections on the phase of the nuclear wavefunction (MAB effect). Since there is not MAB effect for the $2s\ ^2A_1'$ and $2p_z\ ^2A_2''$ electronic potential energy surfaces, we can use both methods in the study of their bound ro-vibrational states. The **TS** method can easily furnish the approximate locations of the ro-vibrational eigen-energies, while the hypersperical one permits us to scan energies near those approximate ones and obtain quickly more accurate levels and their corresponding wavefunctions, having the exact P_3 symmetry built in. This work has been published recently[68].

4. Scattering Wavefunction

4.1 General Considerations

In the theoretical treatment of predissociation processes[11,12] and of transition state spectroscopy (TTS)[39], the unbound scattering wavefunction with a proper physical boundary condition and normalization is required.

In a typical quantum scattering calculation, the scattering matrix S is obtained instead of the physical wavefunction with proper boundary conditions and normalization. The reason is that the scattering matrix S contains all the information about the state-to-state scattering cross sections (which can be compared with experimental results), and therefore makes the construction of the physical wavefunction unnecessary. Many methods of scattering calculation take advantage of this fact and obtain the S matrix without constructing the physical wavefunctions[62-67,69]. Only a few calculations involved with scattering wavefunctions have been published for triatomic systems, both for collinear[74] and 3D[75] cases.

Because the S matrix involves the ratio between the the in-coming parts and the out-going ones of the scattering wavefunctions in the asymptotic regions (where the triatomic system becomes a free atom plus a diatomic molecule, and the wavefunctions can be expressed as a sum of products of the ro-vibration wavefunctions of the diatomic molecule and the plan-wave functions of the free atom with respect to the center of mass of the diatomic molecule), it allows the determination of the physical wavefunction in the asymptotic regions for a given choice of the in-coming parts. This furnishes the explicit boundary problem of the Schrodinger equation. The solution will correspond to the real physical process of interest.

Using the coupled-channel method in hyperspherical coordinates, the wavefunction can be expressed as an expansion in basis set functions of the hyperangles with coefficients as functions of the hyperradius, the Schrodinger (partial differential) equation can be transformed into a set of second order ordinary coupled equations as

$$[\mathbf{I}\frac{d^2}{d^2x} + \mathbf{Q}(x)]\Psi(x) = 0 \tag{39}$$

with

$$\mathbf{Q}(x) = (2\mu/\hbar^2)[E\mathbf{I} - \mathbf{V}(x)] \tag{40}$$

where $\mathbf{I}$ is the identity matrix, and $\mathbf{V}(x)$ the interaction matrix. E is the known total energy of the system. $\Psi(x)$ the expansion coefficient matrix[62-67,76]. Here x is the hyperradius. Detail of the definitions of those matrices can be found elsewhere[62-67,76]

Once scattering matrix S has been determined by a forward integration method, the physical wavefunction $\Psi(x)$ can be calculated from a backward integration of Eq. 39. The initial conditions are obtained by projecting the wavefunction in the asymptotic region, which is obtained from S, into the hyperspherical surface function at large hyperradius. The backward integration is then conducted to a small hyperradius where the interaction is strongly repulsive and the wavefunction vanishes.

Previous calculations[62-64] are all based on the logarithmic derivative method[77] which is not suitable for the construction of the physical wavefunction in the backward propagation because it furnishes the logarithmic derivative matrix rather than the wavefunction matrix itself. We have chosen the renormalized Numerov method[78] for that backward integration.

4.2 Renormalized Numerov Method

In the renormalized Numerov method, the Eq. 39 is transformed into

$$[\mathbf{I} - \mathbf{T}_{n+1}]\Psi_{n+1} - [2\mathbf{I} - \mathbf{T}_n]\Psi_n + [\mathbf{I} - \mathbf{T}_{n-1}]\Psi_{n-1} = 0 \tag{41}$$

by using finite difference scheme, where

$$\Psi_n = \Psi(x_n) \tag{42}$$

and

$$\mathbf{T}_n = -(h^2/12)\mathbf{Q}(x_n) \tag{43}$$

Here h is the spacing between the $N+1$ equally spaced grid point (x_0, x_1, .. , x_N) and $\mathbf{Q}(x)$ is defined by Eq. 40. The $\mathbf{F}_n$ matrix is defined as

$$\mathbf{F}_n = [\mathbf{I} - \mathbf{T}_n]\Psi_n \tag{44}$$

If we substitute Eq. 44 back into Eq. 41, we have

$$\mathbf{F}_{n+1} - \mathbf{U}_n\mathbf{F}_n + \mathbf{F}_{n-1} = 0 \tag{45}$$

with

$$\mathbf{U}_n = (\mathbf{I} - \mathbf{T}_n)^{-1}\,(2\mathbf{I} + 10\mathbf{T}_n) \tag{46}$$

Next, a ratio matrix $\mathbf{R}$ is defined as

$$\mathbf{R}_n = \mathbf{F}_{n+1}\mathbf{F}_n^{-1} \tag{47}$$

This transforms Eq. 45 into the two term recurrence relation

$$\mathbf{R}_n = \mathbf{U}_n - \mathbf{R}_{n-1}^{-1} \tag{48}$$

This is the basic propagation relation for this method.

At large hyperradii (say, x_0 and x_1), the wavefunction is known, so are the expansion coefficient matrices Ψ_0 and Ψ_1 which are obtained by the wavefunction projection in the asymptotic regions. The matrices $\mathbf{F}_0$ and $\mathbf{F}_1$ are obtained by using Eq. 44, and then $\mathbf{R}_0$ by using Eq. 47. Then the backward propagation can be started following Eq. 48, and all Ψ_n be generated accordingly.

We have implemented the renormolized Numerov propagation scheme in the collinear H_3 scattering calculation on its ground potential energy surface in order to test our version of this propagator. The code is currently being debugged and compared with previous results for forward integration[79]. Once this is completed, the backward integration method for determined the physical wave function will be extended to three dimensions.

5. Decay Mechanisms for the H_3 System

The metastable H_3 molecule in the $2p_z\ ^2A_2''$ electronic state can decay via radiative processes to the lower $2s\ ^2A_1'$, $2p\ ^2E'(2)$ and $2p\ ^2E'(1)$ electronic states and by the predissociation to the unbound $2p\ ^2E'(1)$ ground electronic state. In this section, we discuss the calculation of the lifetime via each of these decay channels.

5.1 Radiative Decay and Selection Rules

By coupling to the radiation field, the H_3 molecule can emit radiation as it undergoes a transition from an upper state to a lower one. The general theory of the interaction between a molecular system and a radiation field is beyond the scope of this report and can be found elsewhere[17]. We will consider here three important kinds of transition: electric dipole moment (**E1**), magnetic dipole moment (**M1**) and electric quadrupole moment (**E2**). The lifetime τ associated to each is inversely proportional to the square of the corresponding transition moments:

$$\tau_X \propto |\langle \Psi^i \mid \mathbf{X} \mid \Psi^f \rangle|^{-2} \tag{49}$$

where Ψ^i and Ψ^f are the initial and final wavefunctions for the molecule and $\mathbf{X}$ the transition moment operator under consideration (which can be **E1**, **M1** or **E2**).

The equilibrium geometries of the bound ro-vibrational states of the $2s\ ^2A_1'$, $2p_z\ ^2A_2''$ and the upper manifold of the $2p\ ^2E'$ states (in the absence of John-Teller distortions[19,27]) are of that of an equilateral triangle. For this reason, the wavefunctions of those electronic states display (to zeroth order) D_{3h} symmetry. Using this symmetry, and with the assumption that the transition dipole moments do not change with nuclear geometry, Herzberg *el.al.* have discussed the selection rules for the electric dipole radiative transitions among those four electronic states[5,7]. We have extended their considerations of the electric dipole transition (**E1**), to that of the magnetic dipole (**M1**), and electric quadrupole (**E2**).

We use the same assumption that the multipole moments do not change with nuclear geometry. Under this condition, the integral in Eq. 49 can be separated into a electronic part and a nuclear part, which permits us to rewrite Eq. 49 as:

$$\tau_X \propto |\langle \Psi_e^i \mid X \mid \Psi_e^f \rangle|^{-2} |\langle \Psi_n^i \mid X \mid \Psi_n^f \rangle|^{-2} \tag{50}$$

where Ψ_e and Ψ_n stand for the electronic and nuclear wavefunctions respectively. The electric dipole moment **E1** (being a vector) forms an $A_2'' + E'$ representation of the D_{3h} group, the magnetic dipole moment **M1** (being a skew vector) forms an $A_2' + E''$ one,

and the electric quadrupole moment **E2** (as a second rank tensor) an $A_1' + E' + E''$ one. The symmetry requires that for the integral over electronic coordinates in the right hand side of Eq. 50 not to vanish, it is necessary that the integrand (the product of the initial electronic state, the moment operator and the final electronic state) in that integral must have an A_1' component. Using the properties of the D_{3h} group, this furnishes the selection rules for the transitions between those four electronic states.

For the electric transition dipole moment (**E1**), the transition can have non-zero intensity

- between the $2p_z\ ^2A_2''$ and $2s\ ^2A_1'$ states,
- and between the $2s\ ^2A_1'$ and $2p_{x,y}\ ^2E'(1,2)$ states.

For the magnetic transition dipole moment (**M1**), it can have non-zero intensity

- between the $2p_z\ ^2A_2''$ and $2p_{x,y}\ ^2E'(1,2)$ states.

For the electric transition quadrupole moment (**E2**), it can have non-zero intensity

- between the $2s\ ^2A_1'$ and $2p_{x,y}\ ^2E'(1,2)$ states,
- and between the $2p_z\ ^2A_2''$ and $2p_{x,y}\ ^2E'(1,2)$ states.

Since we have calculated the potential energies of the $2p_z\ ^2A_2''$ and $2s\ ^2A_1'$ states and the electric transition dipole moment between them, we can estimate the lifetime of this decay process. Our estimation was done at $R = 1.64$ bohr (R being the length of the side of the equilateral H_3) where the nuclear configuration is very close to the minima of both potential energy surfaces, using

$$\tau_{i,f}^{-1} = 2.02586 \times 10^{-6} (\Delta E)^3 \mathrm{T}_{i,f}^2 \tag{51}$$

where ΔE is the transition energy ($\Delta E = E_i - E_j$, in cm^{-1}), and $\mathrm{T}_{i,f}$ is the transition dipole moment (in atomic unit) between the initial state ($2s\ ^2A_1'$) to the final state ($2p_z\ ^2A_2''$), and the dipole transition lifetime $\tau_{i,f}$ is in seconds. Our calculated transition energy is 1299 cm^{-1} and the corresponding electric transition dipole moment is 2.68 *a.u.* which yields lifetime of about 31 μs. This compares with the results of 1422 cm^{-1}, 2.69 *a.u.* and 23 μs from Petsalakis *et al.*[32] , and 1988 cm^{-1}, 2.85 *a.u.* and 7.7 μs from King and Morokuma[27]. The lifetime is very sensitive to the transition energy. If the experimental transition energy (of 993 cm^{-1}) is used (which includes the difference between the zero point energies of the nuclei motion on the $2s\ ^2A_1'$ and $2p_z\ ^2A_2''$ potential energy surfaces), the resulting lifetime estimations are 70 μs (this calculation), 62 μs (King and Morokuma) and 70 μs (Petsalakis *et al.*) and all agree with the experimental estimated value reported as being in excess of 40 μs[14].

When the ro-vibrational motion of the nuclei distorts the shape of the molecule away from equilateral triangle, the D_{3h} is no longer the symmetry group of the electronic wavefunction, so that those selection rules should not be observed exactly. For a molecular system, the strength of the coupling with the radiation field generally decreases in the order 1) electric transition dipole, 2) magnetic transition dipole, 3) electric transition quadrupole, and so on. Only if some selection rule prevents the stronger coupling to be non-zero, can the weaker coupling have a chance to show its contribution. When H_3 does not have equilateral triangular geometry, the electric transition dipole coupling can contribute to each of the possible transition between those lowest four electronic states. Therefore, it is appropriate for us to study the electric dipole transition first. With the potential energy surfaces and electric transition dipole moments obtained by the electronic calculation described in section 2, the nuclear ro-vibrational bound states can be obtained by the methods described in section 3, and then the radiative lifetime of $2p_z\ ^2A_2'' \rightarrow 2s\ ^2A_1'$ can be calculated.

5.2 Predissociation

Predissociation can occur as a result of coupling between two Born-Oppenheimer electronically adiabatic potential energy surfaces associated with two electronic states of a molecular system. The Born-Oppenheimer wavefunctions of the system are not in this case true eigenstates of the total molecular Hamiltonian. Interaction between the quasi-bound states of the nuclear motion of an upper surface and the unbound(*i.e.*, scattering) ones of a lower surface can cause a quantum leakage from the former to the latter[15-16]

5.2.1 Fano's Theory[16]

In the simplest case, there are two quantum states associated with the Hamiltonian H. One is bound and denoted as $\mid \phi_n\rangle$ and the other one unbound and denoted as $\mid E\rangle$. They are not exact eigenstates of H and satisfy the following conditions:

$$\langle \phi_n \mid \phi_n \rangle = 1 \tag{52}$$

$$\langle \phi_n \mid E \rangle = 0 \tag{53}$$

$$\langle E \mid E' \rangle = \delta(E - E') \tag{54}$$

$$\langle \phi_n \mid H \mid \phi_n \rangle = E_n \tag{55}$$

$$\langle E \mid H \mid E' \rangle = E\delta(E - E') \tag{56}$$

$$\langle \phi_n \mid H \mid E \rangle = V_n(E) \tag{57}$$

where n designates the set of quantum number which label the bound state, and E is the energy for the unbound state. $V_n(E)$ is the coupling between the bound state and the

unbound state and is usually very small. We expand the true eigenstate of H as

$$\mid \Psi_n(E)\rangle = A_n(E) \mid \phi_n\rangle + \int B_n(E', E) \mid E'\rangle dE' \tag{58}$$

where

$$H \mid \Psi_n(E)\rangle = E \mid \Psi_n(E)\rangle \tag{59}$$

It satisfies the normalization condition

$$\langle \Psi_n(E) \mid \Psi_n(E')\rangle = \delta(E - E') \tag{60}$$

After replacing Eq. 58 into Eqs. 59 and 60, the result is

$$\mid A_n(E) \mid^2 = \frac{\mid V_n(E_n) \mid^2}{(E - E_n - \Delta_n)^2 + \pi^2 \mid V_n(E_n) \mid^4} \tag{61}$$

$$\Delta_n = \mathrm{P} \int \frac{\mid V_n(E') \mid^2}{E - E'} dE' \tag{62}$$

Let us adopt the time-dependent description and prepare the system in state $\mid \phi_n\rangle$ at $t = 0$. We now let the system evolve with time and ask what is the probability $P_n(t)$ of finding the system still in state $\mid \phi_n\rangle$ state at time t? The answer is

$$P_n(t) = \exp(-t/\tau_n) \tag{63}$$

where

$$\tau_n = \frac{\hbar}{2\pi \mid V_n(E_n) \mid^2} \tag{64}$$

The above discussion can be easily generalized into the case in which one bound state is coupled with many unbound states $\mid E, m\rangle$, as happens when the final predissociated system can be characterized by the set of quantum numbers m describing the internal states of the fragments. The result is

$$\tau_n = \frac{\hbar}{2\pi \sum_m \mid V_n^m(E_n) \mid^2} \tag{65}$$

with the coupling between the bound state $\mid \phi_n\rangle$ and the mth unbound state $\mid E, m\rangle$ as

$$V_n^m(E) = \langle \phi_n \mid H \mid E, m\rangle \tag{66}$$

5.2.2 The Form of Coupling Element in Nuclear Coordinates

We now discuss the nature of the coupling elements which appear in Fano's formulas (Eqs. 57, 66). The Hamiltonian of a molecular system has the form:

$$H = H_e + T_N \tag{67}$$

where electronic H_e is the Hamiltonian (with the nuclear variables as parameters) which contains the Coulombic interactions between all charged particles (including nuclei) in the molecule, and T_N is the nuclear kinetic energy operator. We assume that the spin-containing terms are negligible compared with the Coulombic terms as is the case for H_3. We can define a set of electronic basis functions $\phi_n(\mathrm{r},\mathrm{R})$ which satisfy

$$H_e\phi_n(\mathbf{r};\mathbf{R}) = V(\mathbf{R})\phi_n(\mathbf{r};\mathbf{R}) \tag{68}$$

$$\langle\phi_n \mid \phi_{n'}\rangle_{\mathbf{r}} = \delta_{n,n'} \tag{69}$$

where the $\mathbf{r}$ denotes the set of all electronic coordinates and $\mathbf{R}$ the set of all nuclear coordinates. n is the set of quantum numbers which describe the eigenstates of H_e. In order to solve the total Schrodinger equation

$$H\Psi(\mathbf{r},\mathbf{R}) = E\Psi(\mathbf{r},\mathbf{R}) \tag{70}$$

We expand the wavefunction Ψ in the ϕ_n basis set:

$$\Psi = \sum_n \chi_n(\mathbf{R})\phi_n(\mathbf{r};\mathbf{R}) \tag{71}$$

From Eqs. 67-71, we get

$$\sum_n T_N\{\chi_n(\mathbf{R})\phi_n(\mathbf{r};\mathbf{R})\} = \sum_n (E - V_n(\mathbf{R}))\chi_n(\mathbf{R})\phi_n(\mathbf{r},\mathbf{R}) \tag{72}$$

In Eq. 72, the nuclear kinetic operator acts upon both nuclear $\chi_n(\mathbf{R})$ and electronic $\phi_n(\mathbf{r};\mathbf{R})$ wavefunctions. No choice of reference frame and coordinate system used to describe the molecular system is so far implied.

In the laboratory reference frame, the nuclear kinetic energy operator T_N is given by

$$T_N = \sum_i -\frac{\hbar^2}{2\mu_i}\nabla_i^2 \tag{73}$$

where the sum is over all nuclei with μ_i as their masses. When Eq. 73 is put into Eq. 72 with the help of Eqs. 68 and 69, we get the equations which χ_n satisfy:

$$T_N \chi_n + \sum_{n',i} -\frac{\hbar^2}{\mu_i} \phi_n \nabla_i \phi_{n'} \cdot \nabla_i \chi_{n'} + \sum_{n'} \phi_n T_N \phi_{n'} \chi_{n'} = (E - V_n)\chi_n \qquad (74)$$

In the normal treatment of the nuclear motion, only one term is retained and the coupled nuclear equations are replaced by a set of uncoupled equations

$$T_N \chi_n^{\mathrm{BO}}(\mathbf{R}) = (E - V_n(\mathbf{R}))\chi_n^{\mathrm{BO}}(\mathbf{R}) \qquad (75)$$

The corresponding electro-nuclear wavefunction is then

$$\Psi_n^{\mathrm{BO}}(\mathbf{r}, \mathbf{R}) = \chi_n^{\mathrm{BO}}(\mathbf{R}) \phi_n(\mathbf{r}; \mathbf{R}) \qquad (76)$$

It is easy to show that the matrix element of the total Hamiltonian H between a pair of wavefunctions in the form of Eq. 76 but with different electronic states is:

$$\langle \chi_n^{\mathrm{BO}} \phi_n \mid H \mid \phi_{n'} \chi_{n'}^{\mathrm{BO}} \rangle = \langle \chi_n^{\mathrm{BO}} \mid \sum_i \langle \phi_n \mid \frac{-\hbar^2}{\mu_i} \nabla_i \mid \phi_{n'} \rangle \cdot \nabla_i + \langle \phi_n \mid T_N \mid \phi_{n'} \rangle \mid \chi_{n'}^{\mathrm{BO}} \rangle \qquad (77)$$

In our application to predissociation, the initial nuclear bound state and the final nuclear unbound state are Born-Oppenheimer solutions (on different electronic potential energy surfaces), and the corresponding predissociation coupling matrix elements needed for application of the Fano's theory are, in Cartesian coordinates, those shown in Eq. 77.

In practice, the reference frame for the electronic motion is usually chosen to be the body-fixed frame of the nuclei and the translational motion of the center of mass of the system is removed. Because of the large mass difference between the nuclei and electrons, the center of mass of the molecule is very close to the center of mass of the nuclei, and their difference can be safely neglected for the present purposes. The coupling elements appearing in Eq. 77 can be expressed in terms of elements of the type

$$\langle \phi_n \mid \frac{\partial}{\partial x} \mid \phi_{n'} \rangle \cdot \frac{\partial}{\partial x} \qquad (78)$$

and

$$\langle \phi_n \mid \frac{\partial^2}{\partial x^2} \mid \phi_{n'} \rangle \qquad (79)$$

where x can be one of the internal nuclear hyperspherical variables (ρ, ω_λ, γ_λ) *i.e.* the hyperradius and the two internal hyperangles. The elements $\langle \phi_n \mid \frac{\partial}{\partial x} \mid \phi_{n'} \rangle$ and $\langle \phi_n \mid \frac{\partial^2}{\partial x^2} \mid \phi_{n'} \rangle$ must now be calculated with the help of the corresponding electronic wavefunctions.

6. Summary

In order to assess its potential as a future rocket propellant, the lifetime and decay mechanisms of the H_3 molecule in its metastable $2p_z\ ^2A_2''$ electronic state must be understood. We initiated a theoretical study of this decay lifetime, in parallel with the experimental work on the properties of this species.

We have identified the necessary steps for the theoretical investigation. We initiated the calculation of the H_3 electronic potential energy surfaces for the lowest four electronic states ($2p_{x,y}\ ^2E'(1,2)$, $2s\ ^2A_1'$ and $2p_z\ ^2A_2''$) , and of the electric transition dipole moments among them. These calculations will be completed in the near future.

We have developed a very general and powerful hyperspherical coordinate propagation method to obtain the ro-vibrational nuclear bound states, especially useful for A_3 systems (like H_3) having three identical nuclei, for which nuclear permutation symmetry plays an important role. We also used for such calculations the variational method developed by Tennyson and Sutcliffe as a general and robust way to treat the triatomic ro-vibrational motion. Both methods have been tested on the upper manifold of the DMBE surfaces[22] ($2p\ ^2E'(2)$), with or without inclusion of the molecular Aharanov-Bohm effect[68]. We have performed scattering calculations on the lower manifold, up to energies of 2.4 eV, using hyperspherical coordinates[62-64,69], and also showed how to use parallel computers for such calculations[80].

We have developed a numerical methods for generating scattering wavefunctions via backward propagation, once the scattering matrix has been calculated. Such wavefunctions are needed for the predissociation lifetime calculations of interest.

After the ro-vibrational wavefunctions on both the $2s\ ^2A_1'$ and $2p_z\ ^2A_2''$ potential surfaces, and the electric transition dipole moment between them become known, the radiative lifetime calculation of the $2p_z\ ^2A_2''$ state to the $2s\ ^2A_1'$ state can be finally performed accurately. Calculation of the predissociative lifetime of the $2p_z\ ^2A_2''$ state will require a calculation of the appropriate coupling elements to the ground and first excited electronic states.

7. References

1. F.M. Devienne and J.C. Rousteau, "Physique Moléculaire-Déttermination de l'existence et de certaines propriétés de jets moléculaire triatomiques d'hudrogéne," Comptes Rendus Academie Des Sciences Paris Series B : Science Physiques, **Vol. 263**, No. 25, pp. 1389-1392, December 19, 1966.

2. M. Vogler, "Observation of an Electronically Excited State of H_3 and Determination of Its Vibrational Level Structure," Physical Review A, **Vol. 19**, No. 1, pp. 1-5, Janurary 1979.

3. J. Watson, "Predissociation Spectrum of an Excited Electronic States of the H_3 Molecule," Physical Review A, **Vol. 22**, No. 5, pp. 2279-2280, November, 1980.

4. G. Gellene and R. Porter, "Experimental Observation of Excited Dissociative and Metastable States of H_3 in Neutralized Ion Beams," Journal of Chemical Physics, **Vol. 79**, No. 12, pp. 5975-5981, December 15, 1983.

5. G. Herzberg, "A Spectrum of Triatomic Hydrogen," Journal of Chemical Physics, **Vol. 70**, No. 10, pp. 4806-4807, May 15, 1979.

6. G. Herzberg, H. Lew, J. J. Sloan, and J. K. G. Watson, "The Electronic Emission Spectrum of Triatomic Hydrogen. IV. Infrared Perpendicular Bands Near 3600 cm^{-1}," Canadian Journal of Physics, **Vol. 59**, No. 3, pp. 428-440, March 1981.

7. I. Dabrowski and G. Herzberg, "The Electronic Emission Spectrum of Triatomic Hydrogen. I. Paralle Bands of H_3 and D_3 Near 5600 and 6025 Å," Canadian Journal of Physics, **Vol. 58**, No. 8, pp. 1238-1249, August 1980.

8. G. Herzberg and J.K.G. Watson, "The Electronic Emission Spectrum of Triatomic Hydrogen. II. Perpendicular Bands Near 7100 Å," Canadian Journal of Physics, **Vol. 58**, No. 8, pp. 1250-1258, August 1980.

9. G. Herzberg, J.T. Hougen, and J.K.G. Watson, "The Electronic Emission Spectrum of Triatomic Hydrogen. IV. Visible Bands Near 5800 Å and Infrared Bands Near 3950 cm^{-1}," Canadian Journal of Physics, **Vol. 60**, No. 9, pp. 1261-1284, September 1982.

10. H. Helm, "Observation of High-n Rydberg Series ($7 < n < 40$) of the H_3 Molecule", Physical Review Letters, Vol. 56, No. 1, pp. 42-45, 6 January 1986.

11. H. Helm, "Measurement of the Ionization Potential of Triatomic Hydrogen", Physical Review A, Vol. 38, no. 7, pp. 3425-3429, October 1988.

12. P.C. Cosby and H. Helm, "Photodissociation of the Triatomic Hydrogen", Physical Review Letters, Vol. 61, no. 3, pp. 298-301, 18 July 1988.

13. H. Helm, L.J. Lembo, P.C. Cosby, and D.L. Huestis, "Photoionization and Dissociation of the Triatomic Hydrogen Molecule", Fundamentals of Laser Interactions II, Ehlotzky (editor), pp. 264-287, Springer–Verlag, 1989

14. J.F. Garvey and A. Kuppermann, "An Intensive Beam of Metastable H_3 Molecules," Chemical Physics Letter, Vol. 107, No.6, pp. 491-495, June 15, 1984.

15. Hélène Lefebvre-Brion and Robert W. Field, "Perturbations in the Spectra of Diatomic Molecules," Chapter 6, **Predissociation**, pp. 331-382, Academic Press, Inc. (1986)

16. U. Fano, "Effect of Configuration Interaction on Intensities and Phase Shifts," Physcal Review, Vol. 124, No. 6, pp. 1866-1878, December 15, 1961.

17. M. Weissbluth, **Atoms and Molecules**, pp. 510, Academic Press (1978)

18. M. Born and R. Oppenheimer, Ann. Phys., Vol. 84, pp. 457, 1927.

19. R. N. Porter, R. M. Stevens and M. Karplus, "Symmetric H_3: A Semi-empirical *Ab Initio* Study of a Simple Jahn-Teller System," Journal of Chemical Physics, Vol. 49, No. 11, pp. 5163-5178, December 1, 1968.

20. P. Siegbahn and B. Liu, "An Accurate Three-dimensional Potential Energy Surface for H_3," Journal of Chemical Physics, Vol. 68, No. 5, pp. 2457-2465, March 1. 1978.

21. D.G. Truhlar and C.J. Horowitz, "Fuctional Representation of Liu and Siegbahn's Accurate *Ab Initia* Potential Energy Calculations for H + H_2," Journal of Chemical Physics, Vol. 68, No. 5, pp. 2466-2476, March 1, 1978.

22. A. J. C. Varandas, F. B. Brown, C. A. Mead, D. G. Truhlar, "A Double Many-body Expansion of the Two Lowest-energy Potential Surfaces and Nonadiabatic Coupling for H_3," Journal of Chemical Physics, **Vol. 86**, No. 11, pp. 6258-6269, July 1, 1987.

23. K.D. Jordan, "Construction of Potential Energy Curves in Avoided Crossing Situations," Chemical Physics, **Vol. 9**, pp. 199-204, 1975

24. A.J.C. Varandas, "A Double Many-body Expansion of Molecular Potential Energy Functions," Molecular Physics, **Vol. 53**, No. 6, pp. 1303-1325, 1984

25. A.J.C. Varandas, "A General Approach to the Potential Energy Functions of Small Polyatomic System: Molecules and Van Der Waals Molecules," Journal of Molecular Structure, **Vol. 120**, pp. 401-424, 1985.

26. T.C. Thompson and C.A. Mead, "Adiabatic Electronic Energies and Nonadiabatic Couplings to all Orders for System of Three Identical Nuclei with Conical Intersection," Journal of Chemical Physics, **Vol. 82**, No. 5, pp. 2408-2417, March 1, 1985.

27. H.F. King and K. Morokuma, "Theory of the Rydberg Spectrum of Triatomic Hydrogen," Journal of Chemical Physics, **Vol. 71**, No. 8, pp. 3213-3220, October 15, 1979.

28. R.L. Martin, "Rydberg States of H_3," Journal of Chemical Physics, **Vol. 71**, No. 8, pp. 3541-3542, October 15, 1979.

29. M. Junsen, "Rydberg States of H_3," Journal of Chemical Physics, **Vol. 71**, No. 8, pp. 3540-3541, October 15, 1979.

30. C.H. Nager and M. Junsen, "Potential Surfaces for the Rydberg States of H_3," Chemical Physics, **Vol. 70**, pp. 189-198, 1982.

31. K.C. Kulander and M.F. Guest, "Excited Electronic States of H_3 and Their Roles in the Dissociative Recombination of H_3^+," Journal of Physics B : Atomic and Molecular Physics, **Vol. 12**, No. 16, pp. L501-L504, August 1979.

32. I.D. Petsalakis, G.Theodorakopoulos and J.S. Wright, "Theoretical Calculation on Electronic Transitions for H_3, Including Rydberg and Transition State Spectra,"

Journal of Chemical Physics, Vol. 89, No. 11, pp. 6850-6859, December 1, 1988.

33. R.J. Buenker, S.D. Peyerimhoff and W. Butshuer, "Applicability of the Multi-reference Double-excitation CI (MRD-CI) Method to the Calculation of Electronic Wavefunctions and Comparison with Related Techniques," Molecular Physics, Vol. 35, No. 3, pp. 771-791, 1978.

34. R.J. Buenker and S.D. Peyerimhoff, "Individualized Configuration Selection in CI Calculations with Subsequent Energy Extrapolation," Theoret. Chim. Acta (Berl.), Vol. 35, pp. 33-58, 1974.

35. S. Huzinaga, "Gaussian-Type Functions for Poly-atomic Systems I", Journal of Chemical Physics, Vol. 42, No. 4, pp. 1293-1302, February 15, 1965.

36. Dahbia Talbi and R.P. Saxon, "Theoretical Study of Excited Singlet States of H_3^+: Potential Surfaces and Transition Moments," Journal of Chemical Physics, Vol. 89, No. 4, pp. 2235-2241, August 15, 1988.

37. W. Kolos and L. Wolniewicz, "Potential-Energy Curves for the $X\ ^1\Sigma_g^+$, $b\ ^3\Sigma_u^+$, and $C\ ^1\Pi_u$ States of the Hydrogen Molecule", Journal of Chemical Physics, Vol. 43, No. 7, pp. 2429-2441, October 1965.

38. G.C. Schatz, "The Analytical Representation of the Electronic Potential-energy surfaces," Review of Modern Physics, Vol. 61, pp. 669-688, 1989.

39. A.B. Raksit and R.F. Poter, and W.P Garver and J.J. Leventhal, "Bound-Free Ultraviolet Emission from Triatomic Hydrogen," Physical Review Letters, Vol. 55, No. 4, pp. 378-381, July 22, 1985.

40. B.A. Collings, J.C. Polanyi, M.A. Smith, A. Stolow, and A.W. Tarr, "Observation of the Transition State HD_2^* in Collisions, $H + D_2$," Physical Review Letters, Vol. 59, No. 22, pp. 2551-2554, November 30, 1987.

41. H.R. Mayne, R.A. Poirier, and J.C. Polanyi, "Spectroscopy of the Transition State (Theory). II. Absorption by H_3^* in $H + H_2 \rightarrow H_3^* \rightarrow H_2 + H$," Journal of Chemical Physics, Vol. 80, No. 9, pp. 4025-4034, May 1, 1984.

42. V. Engel and Horia Metiu, "The Relative Kinetic Energy Distribution of the Hydrogen Atoms Formed by the Dissociation of the Electronically Excited H_2 Molecule," Journal of Chemical Physics, Vol. 89, No. 4, pp. 1986-1993, August 15, 1988.

43. T. Seideman and M. Shapiro, "Three-dimensional Quantum Theory of the $H + H_2$ Transition-state Spectrum", Journal of Chemical Physics, Vol. 92, No. 4, pp. 2328-2341, October 1989; and references therein.

44. S. Carter and N.C. Handy, "The Variational Method for the Calculation of Rovibrational Energy Levels," Computer Physics Reports, Vol. 4, pp. 115-172, 1986.

45. J. Tennyson, "TRIATOM, SELECT and ROTLEV- for the Calculation of the Rovibrational Levels of Triatomic molecules," Computer Physics Communication, Vol. 42, pp. 257-270, 1986; "The Calculation of the Vibration-Rotation Energies of Triatomic Molecules Using Scattering Coordinates," Computer Physics Reports, Vol. 4, pp. 1-36, July 1, 1986.

46. F.R. Burden and A. Cuno, "A Variational Description of the Rotational and Vibrational States of Triatomic Molecules Using Numerical Wavefunctions," Molecular Physics, Vol. 62, No. 1, pp. 33-44, 1987.

47. S.L. Holmgren, M. Waldman, and W. Klemperer, "Internal Dynamics of Van Der Waals Complexes.I. Born-Oppenheimer Separation of the Radial and Angular Motion," Journal of Chemical Physics, Vol. 67, pp. 4414-4422, November 15, 1977.

48. S. Carter, P. Rosmus, N.C. Handy, S. Miller, J. Tennyson, and B.T. Sutcliffe, "Benchmark Calculations of First Principles Rotational and Vibrational Line Strengths," Computer Physics Reports, Vol. 55, pp. 71-75, 1989.

49. H.C. Longuet-Higgins, U. Öpik, M.H.L. Pryce and R.A. Sack, "Studies of the Jahn-Teller Effect II. The Dynamical Problem," Proceedings Royal Society, Vol. 244A, pp. 1-16, Februray 25,1958.

50. G. Herzberg and H.C. Longuet-Higgins, "Intersection of Potential Surfaces in Polyatomic Molecules," Discussions Faraday Society, Vol. 35, pp. 77-80, 1963.

51. C.A. Mead and D.G. Truhlar, "On the Determination of Born-Oppenheimer Nuclear Motion Wave Functions Including Complications due to Conical Intersections and

Identical Nuclei," Journal of Chemical Physics, Vol. 70, No. 5, pp. 2284-2296, March 1, 1979.

52. C.A. Mead, "The Molecular Aharonov-Bohm Effect in Bound States," Chemical Physics, Vol. 49, pp. 23-32, 1979.

53. A.S. Davydov, **Quantum Mechanics**, second edition, pp. 151-161, Pergamon Press, Oxford, 1976

54. M. Weissbluth, **Atoms and Molecules**, pp. 3-5, Academic Press, 1978

55. J. Tennyson and B.T. Sutcliffe, "On the Rovibrational Levels of the H_3^+ and H_2D^+ Molecules," Molecular Physics, Vol. 51, No. 4, pp. 887-906, 1984.

56. J. Tennyson and B.T. Sutcliffe, "The Infrared Spectrum Of H_3^+ and its Isotopomers," Journal of Chemical Society, Farady Transaction2, Vol. 82, pp. 1151-1162, 1986.

57. B. Martire and P.G. Burton, "The Vibrational Spectra of H_3^+ and D_3^+: Improved Values from New Representations of *Ab Initio* Surfaces," Chemical Physics Letters, Vol. 121, pp. 479, 1985.

58. R. Schinke, M. Dupuis and W.A. Lester, Jr., "Proton-H_2 Scattering on An *Ab Initio* CI Potential Energy Surface.I. Vibrational Excitation at 10 eV," Journal of Chemical Physics, Vol. 72, No. 7, pp. 3909-3915, April 1, 1980.

59. Aron Kuppermann, "A Useful Mapping of Triatomic Potential Energy Surfaces," Chemical Physics Letters, Vol. 32, pp. 374-375, 1975.

60. J.G. Frey and B.J. Howard, "The Calculation of the Ground State Energy of Weakly Bound Van Der Waals Trimers Using the Method of Hyperspherical Harmonics.I. The Born-Oppenheimer and Adiabatic Approximations," Chemical Physics, Vol. 99, pp. 415-426, 1985.

61. J.M. Hutson and S. Jain, "On the Coupled-channel Calculation of Bound States for Triatomic Systems using Hyperspherical Coordinates," Journal of Chemical Physics, Vol. 91, No. 7, pp. 4197-4203, October 1, 1989.

62. A. Kuppermann and P.G. Hipes, "Three-dimensional quantum mechanical reactive scattering using symmetrized hyperspherical coordinates", Journal of Chemical Physics, Vol. 84, No. 10, pp. 5962, May 1986.

63. S.A. Cuccaro, P.G. Hipes and A. Kuppermann, "Hyperspherical Coordinate Reactive Scattering Using Variational Surface Functions," Chemical Physics Letters, Vol. 154, No. 2, pp. 155-163, January 13, 1989.

64. S.A. Cuccaro, P.G. Hipes and A. Kuppermann, "Symmetry Analysis of Accurate $H + H_2$ Resonances for Low Partial Waves", Chemical Physics Letters, Vol. 157, No. 5, pp. 440-446, 19 May 1989.

65. R.T. Pack and G.A. Parker, "Quantum Mechanical Scattering in Three Dimensions Using Hyperspherical (APH) Coordinates. Theory", Journal of Chemical Physics, Vol. 87, No. 7, pp. 3888-3921, October 1987;
G.A. Parker, R.T. Pack, B.J. Archer, and R.B. Walker, "Quantum Reactive Scattering in Three Dimensions Using Hyperspherical (APH) Coordinates. Tests on $H + H_2$ and $D + H_2$", Chemical Physics Letters, Vol. 137, No. 6, pp. 564-568, 3 July, 1987;
R.T. Pack and G.A. Parker, "Quantum Reactive Scattering in Three Dimensions Using Hyperspherical (APH) Coordinates. III. Small θ Behavior and Corrigenda", Journal of Chemical Physics, Vol. 90, No. 7, pp. 3511-3519, April 1989.

66. J.M. Launay and M. Le Dourneuf, "Hyperspherical Coordinates Close-coupling Calculation of Integral Cross Section for the Reactive $H + H_2 \rightarrow H_2 + H$," Chemical Physics Letters, Vol. 163, pp. 178, 1989.

67. J.M. Launay and B. Lepetit, "Three-dimensional Quantum Study of the Reaction $H + FH(\nu j) \rightarrow HF(\nu' j') + H$ in Hyperspherical Coordinates," Chemical Physics Letters, Vol. 144, pp. 346, 1988.

68. B. Lepetit, Z. Peng, and A. Kuppermann, "Calculation of Bound Rovibrational States on the First Electronically Excited State of the H_3 System," Chemical Physics Letters, Vol. 166, No. 5,6 pp. 572-580, March 1990.

69. B. Lepetit and A. Kuppermann, "Numerical study of the geometric phase in the $H + H_2$ reaction", Chemical Physics Letters, Vol. 166, No. 5,6 pp. 581-588, March 1990.

70. L.M. Delves, "Tertiary and General-order Collision I", Nuclear Physics, **Vol. 9**, pp. 391, 1959; "Tertiary and General-order Collision II", Nuclear Physics, **Vol. 20**, pp. 275, 1960.

71. R.C. Whitten and F.T. Smith, "A Symmetric Representation for Three-body Problems. II Motion in Space*," Journal of Mathematical Physics, **Vol. 9**, pp. 1103-1113, 1969.

72. F.T. Smith, "A Symmetric Representation for Three-body Problems.I. Motion in Plane," Journal of Mathematical Physics, **Vol. 3**, pp. 735-748, 1962.

73. B.R. Johnson, "On Hyperspherical Coordinates and Mapping the Internal Configurations of a Three Body System," Journal of Chemical Physics, **Vol. 73**, No. 10, pp. 5051-5058, November 15, 1980; "The Quantum Dynamics of the Three Particles in Hyperspherical Coordinates," Journal of Chemical Physics, **Vol. 79**, No. 4, pp. 1916-1925, August 15, 1983.

74. J.A. Kaye, "Theoretical Studies of Chemical Reaction Dynamics", Ph.D Thesis, California Institute of Technology, 1982. pp. 653-727

75. G.C. Schatz, "A Three Dimensional Reactive Scattering Study of the Photodetachment Spectrum of $ClHCl$," Journal of Chemical Physics, **Vol. 90**, No. 7, pp. 3582-3589, April 1, 1988; "A Three Dimensional Quantum Reactive Scattering Study of the $I + HI$ reaction and of the IHI^- Photo-detachment Spectrum," Journal of Chemical Physics, **Vol. 90**, No. 9, pp. 4847-4854, May 1, 1989.

76. A. Kuppermann, Theoretical Physics : advances and perspectives, **6A**, pp. 79, 1981; and references therein.

77. LBL-9501, UC-4, CONF-790696, NRCC Proceedings No. **5**, Vol I, **Algorithms and Computer Codes for the Atomic and Molecular Quantum Scattering Theory.** pp. 86, edited by Lowell Thomas, Lawrence Berkeley Laboratory, University of California, Berkeley, 1979

78. B.R. Johnson, "The Renormalized Numerov Method Applied to Calculating Bound States of the Coupled-channel Schrodinger Equation," Journal of Chemical Physics, **Vol. 69**, pp. 4678, 1978.

79. A. Kuppermann, J.A. Kaye, and J.P. Dwyer, "Hyperspherical Coordinates in Quantum Mechanical Collinear Reactive Scattering", Chemical Physics Letters, Vol. 74, pp. 257-262, 1980.

80. Y.S.M. Wu, S.A. Cuccaro, P.G. Hipes, and A. Kuppermann, "Quantum Mechanical Reactive Scattering Using a High-performance Distributed-memory Parallel Computer", Chemical Physics Letters, Vol. 168, No. 5, pp. 429-440, 11 May, 1990.

8. Reprints

The following five papers have been published , describing part of the work supported by this contract:

1. S.A. Cuccaro, P.G. Hipes and A. Kuppermann, "Hyperspherical Coordinate Reactive Scattering Using Variational Surface Functions," Chemical Physics Letters. **Vol. 154**, No. 2, pp. 155-163, January 13, 1989.

2. S.A. Cuccaro, P.G. Hipes and A. Kuppermann, "Symmetry Analysis of Accurate $H + H_2$ Resonances for Low Partial Waves", Chemical Physics Letters, **Vol. 157**, No. 5, pp. 440-446, 19 May 1989.

3. B. Lepetit, Z. Peng, and A. Kuppermann, "Calculation of Bound Rovibrational States on the First Electronically Excited State of the H_3 System," Chemical Physics Letters,, **Vol. 166**, No. 5,6 pp. 572-580, March 1990.

4. B. Lepetit and A. Kuppermann, "Numerical study of the geometric phase in the $H + H_2$ reaction", Chemical Physics Letters,, **Vol. 166**, No. 5,6 pp. 581-588, March 1990.

5. Yi-Shuen M. Wu, S.A. Cuccaro, P.G. Hipes, and A. Kuppermann, "Quantum Mechanical Reactive Scattering Using a High-Performance Distributed-Memory Parallel Computer", Chemical Physics Letters, **Vol. 168**, No. 5, pp. 429-440, 11 May, 1990.

HYPER-SPHERICAL COORDINATE REACTIVE SCATTERING USING VARIATIONAL SURFACE FUNCTIONS

Steven A. CUCCARO [1], Paul G. HIPES [2] and Aron KUPPERMANN

Arthur Amos Noyes Laboratory of Chemical Physics, Division of Chemistry and Chemical Engineering [3], California Institute of Technology, Pasadena, CA 91125, USA

Received 3 October 1988; in final form 11 October 1988

An efficient numerical method of calculating surface functions for accurate quantum mechanical three-dimensional reactive scattering using symmetrized hyper-spherical coordinates has been developed. This method is at least 20 times faster than the finite-element method used previously and its accuracy is demonstrated for the $H+H_2$ system.

1. Introduction

Accurate quantum solutions for three-dimensional reactive scattering for triatomic systems were first calculated in the mid 1970s for the system $H+H_2$ [1–5]. The difficulty and computational expense of these calculations has, until recently, precluded extension to higher energies and more complex systems; however, the development of more efficient algorithms coupled with increased access to supercomputers has resulted in a resurgence of activity in this field [6–17]. In particular, the use of symmetrized hyper-spherical coordinates (SHC) and local hyper-spherical surface functions (LHSF) [18,19] is a very promising approach.

The first accurate calculations of 3D reactive scattering matrices using a hyper-spherical coordinate method were recently performed on the total angular momentum $J=0$ partial wave of the $H+H_2$ system [6]. This method, applied to the PK2 potential energy surface [20], involved the calculation of sets of LHSF using a two-dimensional finite-element (FE) approach. The FE method is accurate and reliable for this system, and has been used to extend the range of energies at which the corresponding $J=0$ partial wave scattering matrices have been calculated to 1.6 eV [11]; however, extension to higher values of J and to less symmetric systems requires an excessive increase in computational effort. As a consequence, there was a need to develop a more efficient method for calculating these LHSF.

In this paper we present a new variational method for calculating LHSF. The formalism is described in section 2. Section 3 discusses the numerical parameters used and section 4 compares the results of LHSF and scattering calculations for the $J=0$ partial wave on both the PK2 and LSTH [21,22] potential energy surfaces with those of previous calculations using a finite-element method [6,11,23] to obtain the surface functions. In addition, some comparison of the $J=1$ PK2 scattering results with those of the matching method [3] are made. A summary is given in section 5.

[1] Work performed in partial fulfillment of the requirements for the Ph.D. degree in Chemistry at the California Institute of Technology.

[2] Current address: 216 Synchrotron Laboratory 206-49, California Institute of Technology, Pasadena, CA 91125, USA.

[3] Contribution No. 7865.

2. Formalism of variational surface functions

The SHC coordinate system used in this calculation has been described previously [6,11,18,19]. Let A_α, A_β, A_γ be the atoms of a triatomic system and λ, ν, κ an arbitrary permutation of α, β, γ. The λ SHC for this system are

$$\rho=(r_\lambda^2+R_\lambda^2)^{1/2},\quad \omega_\lambda=2\arctan\frac{r_\lambda}{R_\lambda},\quad \gamma_\lambda=\arccos\frac{\boldsymbol{R}_\lambda\cdot\boldsymbol{r}_\lambda}{R_\lambda r_\lambda},\qquad 0\leqslant\omega_\lambda,\gamma_\lambda\leqslant\pi\,, \tag{1}$$

where $\boldsymbol{r}_\lambda$ is the mass-scaled [24,25] internuclear vector for the diatom $A_\nu A_\kappa$ and $\boldsymbol{R}_\lambda$ the position vector of the atom A_λ with respect to the center of mass of $A_\nu A_\kappa$. The orientation of the system in space is determined by the Euler angles θ_λ, ϕ_λ (the polar angles of $\boldsymbol{R}_\lambda$ with respect to a space-fixed OZ axis), and ψ_λ (the angle between the $\boldsymbol{R}_\lambda,\boldsymbol{r}_\lambda$ and $\boldsymbol{R}_\lambda,OZ$ half-planes). In this coordinate system the Hamiltonian is expressed as

$$\hat{H}_\lambda=-\frac{\hbar^2}{2\mu}\rho^{-5/2}\frac{\partial^2}{\partial\rho^2}\rho^{5/2}+\frac{\hat{\Lambda}^2}{2\mu\rho^2}+V(\rho,\omega_\lambda,\gamma_\lambda)+\frac{15\hbar^2}{8\mu\rho^2}\,, \tag{2}$$

in which the global reduced mass μ is defined as $[m_\lambda m_\nu m_\kappa/(m_\lambda+m_\nu+m_\kappa)]^{1/2}$. The generalized or grand canonical angular momentum operator $\hat{\Lambda}^2$ is defined by

$$\hat{\Lambda}^2=\hat{L}_\lambda^2+\frac{\hat{l}_\lambda^2}{\cos^2(\frac{1}{2}\omega_\lambda)}+\frac{\hat{j}_\lambda^2}{\sin^2(\frac{1}{2}\omega_\lambda)}\,, \tag{3}$$

where $\hat{l}_\lambda^2$ and $\hat{j}_\lambda^2$ are the angular momentum operators associated with the vectors $\boldsymbol{R}_\lambda$ and $\boldsymbol{r}_\lambda$, respectively, and

$$\hat{L}_\lambda^2=\frac{-4\hbar^2}{\sin\omega_\lambda}\left(\frac{\partial^2}{\partial\omega_\lambda^2}+1\right)\sin\omega_\lambda \tag{4}$$

is an angular momentum associated with the hyper-angle ω_λ. The term $V(\rho,\omega_\lambda,\gamma_\lambda)$ is the potential energy function of the electronically adiabatic triatomic system.

The equation that defines the LHSF $\Phi_n^{J\mathcal{M}\Pi\Gamma}$ with associated eigenvalues $\epsilon_n^{J\Pi\Gamma}$ is

$$\left(\frac{\hat{\Lambda}^2}{2\mu\rho^2}+V(\rho,\omega_\lambda,\gamma_\lambda)\right)\Phi_n^{J\mathcal{M}\Pi\Gamma}(\zeta_\lambda;\rho)=\epsilon_n^{J\Pi\Gamma}(\rho)\,\Phi_n^{J\mathcal{M}\Pi\Gamma}(\zeta_\lambda;\rho)\,, \tag{5}$$

in which ζ_λ stands for the set of five hyper-spherical angles $(\omega_\lambda,\gamma_\lambda,\theta_\lambda,\phi_\lambda,\psi_\lambda)$. The indices J, M, Π, Γ are, respectively, the quantum numbers of the total angular momentum of the system, its projection on the space-fixed OZ axis, the inversion parity of the triatomic system through its center of mass, and the irreducible representation of the surface function in the permutation group of the system (P_3 for $H+H_2$). The boundary conditions for eq. (5) are the usual "well-behavedness" ones (single valuedness, continuity, non-divergence, differentiability, etc.). The index n denotes a quantum number which, in addition to J, M, Π, Γ, uniquely labels the LHSF. A set of two-dimensional surface functions $\psi_{n\Omega}^{J\Pi\Gamma}(\omega_\lambda,\gamma_\lambda;\rho)$ independent of the orientation of the system in space can be defined by expansion of the LHSF in terms of Wigner rotation matrices $D_{M\Omega}(\phi_\lambda,\theta_\lambda,\psi_\lambda)$ [26]:

$$\Phi_n^{J\mathcal{M}\Pi\Gamma}(\zeta_\lambda;\rho)=\sum_{\Omega=0}^{J}\mathcal{S}_{M\Omega}^{J\Pi}(\phi_\lambda,\theta_\lambda,\psi_\lambda)\,\psi_{n\Omega}^{J\Pi\Gamma}(\omega_\lambda,\gamma_\lambda;\rho)\,, \tag{6}$$

where

$$\mathcal{S}_{M\Omega}^{J\Pi}(\phi_\lambda,\theta_\lambda,\psi_\lambda)=\mathcal{N}_{J\Omega}[D_{M\Omega}^{J}(\phi_\lambda,\theta_\lambda,\psi_\lambda)+(-1)^{J+\Pi+\Omega}D_{M,-\Omega}^{J}(\phi_\lambda,\theta_\lambda,\psi_\lambda)]$$

and $\mathcal{N}_{J\Omega}$ is a normalization constant. $\mathcal{S}_{M\Omega}^{\Pi}$ is even (odd) with respect to inversion of the system through its

center of mass for $\Pi=0$ (1), and in the case of $\Omega=0$ is zero when $J+\Pi$ is odd. The boundary conditions for the $\psi^{J\Pi\Gamma}_{n\Omega}(\omega_\lambda, \gamma_\lambda; \rho)$ which result from the "well-behavedness" of the $\Phi^{JM\Pi\Gamma}_n$ are that

$$\psi^{J\Pi\Gamma}_{n\Omega}(\omega_\lambda, \gamma_\lambda=\{0, \pi\}; \rho)=0 \qquad \text{for } \Omega\neq 0$$

and

$$\frac{\partial}{\partial\gamma_\lambda}[\psi^{J\Pi\Gamma}_{n\Omega}(\omega_\lambda, \gamma_\lambda; \rho)]|_{\gamma_\lambda=\{0,\pi\}}=0 \qquad \text{for } \Omega=0 .$$

Furthermore, the potential function $V(\rho, \omega_\lambda, \gamma_\lambda)$ has in general extrema at $\gamma_\lambda=\{0, \pi\}$ (corresponding to collinear configurations of the system). As a result of these considerations, the $\psi^{J\Pi\Gamma}_{n\Omega}$ can be factored as a function of ω_λ times a normalized [2] associated Legendre function $\mathscr{P}^\Omega_j(\cos\gamma_\lambda)$ in the vicinity of $\gamma_\lambda=0$ and π. This makes it both convenient and desirable (because of the presence in eq. (3) of the operator $\hat{j}^2_\lambda$) to expand these $\psi^{J\Pi\Gamma}_{n\Omega}$ according to

$$\psi^{J\Pi\Gamma}_{n\Omega}(\omega_\lambda, \gamma_\lambda; \rho)=\sum_{j=\Omega}^{\infty}\mathscr{P}^\Omega_j(\cos\gamma_\lambda)\frac{\phi^{J\Pi\Gamma}_{nj\Omega}(\omega_\lambda; \rho)}{\sin\omega_\lambda}, \tag{7}$$

where the coefficients $\phi^{J\Pi\Gamma}_{nj\Omega}(\omega_\lambda; \rho)$ are called one-dimensional surface functions. Replacement of eqs. (7) and (6) into eq. (5) leads to the equation satisfied by these functions:

$$\frac{\hbar^2}{2\mu\rho^2}\left\{\left[-4\left(\frac{\partial^2}{\partial\omega_\lambda^2}+1\right)+\frac{J(J+1)+j(j+1)-2\Omega^2}{\cos^2(\frac{1}{2}\omega_\lambda)}+\frac{j(j+1)}{\sin^2(\frac{1}{2}\omega_\lambda)}\right]\phi^{J\Pi\Gamma}_{nj\Omega}(\omega_\lambda; \rho)\right.$$

$$\left.-\frac{\hbar^2}{\cos^2(\frac{1}{2}\omega_\lambda)}[\xi_+(J, \Omega)\,\xi_+(j, \Omega)\,\phi^{J\Pi\Gamma}_{nj,\Omega+1}(\omega_\lambda; \rho)+\xi_-(J, \Omega)\,\xi_-(j, \Omega)\,\phi^{J\Pi\Gamma}_{nj,\Omega-1}(\omega_\lambda; \rho)]\right\}$$

$$+\sum_{j=\Omega}^{\infty}V^\Omega_{jj'}(\rho, \omega_\lambda)\,\phi^{J\Pi\Gamma}_{nj\Omega}(\omega_\lambda; \rho)=\epsilon^{J\Pi\Gamma}_n(\rho)\,\phi^{J\Pi\Gamma}_{nj\Omega}(\omega_\lambda; \rho) . \tag{8}$$

The multiplicative factor $(\sin\omega_\lambda)^{-1}$ has been introduced into eq. (7) because of the form of eq. (4). The presence of this term forces the boundary conditions $\phi^{J\Pi\Gamma}_{nj\Omega}(\omega_\lambda=\{0, \pi\}; \rho)=0$ for eq. (8). These conditions are necessary for $\psi^{J\Pi\Gamma}_{n\Omega}$ not to diverge at $\omega_\lambda=\{0, \pi\}$ but may not be sufficient; however, in practice they have indeed sufficed for $H+H_2$, and we do not anticipate problems with other systems. In eq. (8), $\xi_\pm(i, k)=[i(i+1)-k(k\pm1)]^{1/2}$ and the term $V^\Omega_{jj'}$ is given by

$$V^\Omega_{jj'}(\rho, \omega_\lambda)=\int_0^\pi\mathscr{P}^\Omega_{j'}(\cos\gamma_\lambda)\,V(\rho, \omega_\lambda, \gamma_\lambda)\,\mathscr{P}^\Omega_j(\cos\gamma_\lambda)\sin\gamma_\lambda\,d\gamma_\lambda . \tag{9}$$

It is important to note that for eq. (8) to be valid, the functions $\phi^{J\Pi\Gamma}_{nj\Omega}$ with $\Omega=0$ must be defined to be identically equal to zero when $J+\Pi$ is odd. The set of equations (6), (7), and (8) are equivalent to eq. (5).

The variational basis set is suggested by the expansion equation (7) and by eq. (8). We define functions $t^{J\lambda}_{ij\Omega}(\omega_\lambda; \rho)$ with associated eigenvalues $e^J_{ij\Omega}(\rho)$ which satisfy the latter after the Ω and j coupling is removed:

$$\left[-\frac{2\hbar^2}{\mu\rho^2}\left(\frac{\partial}{\partial\omega_\lambda^2}+1-\frac{J(J+1)+j(j+1)-2\Omega^2}{4\cos^2(\frac{1}{2}\omega_\lambda)}-\frac{j(j+1)}{4\sin^2(\frac{1}{2}\omega_\lambda)}\right)+V^\Omega_{jj'}\right]t^{J\lambda}_{ij\Omega}=e^J_{ij\Omega}t^{J\lambda}_{ij\Omega} . \tag{10}$$

These functions are required to satisfy the same boundary conditions as the $\phi^{J\Pi\Gamma}_{nj\Omega}$: $t^{J\lambda}_{ij\Omega}(0; \rho)=t^{J\lambda}_{ij\Omega}(\pi; \rho)=0$. We now define a five-dimensional variational basis set by

$$F^{JM\Pi}_{\lambda ij\Omega}(\zeta_\lambda; \rho)=\mathscr{D}^{J\Pi}_{M\Omega}(\phi_\lambda, \theta_\lambda, \psi_\lambda)\,\mathscr{P}^\Omega_j(\cos\gamma_\lambda)\,f^{J\lambda}_{ij\Omega}(\omega_\lambda; \rho) , \tag{11}$$

where for notational convenience we have defined $f^{J\lambda}_{ij\Omega}(\omega_\lambda; \rho)=t^{J\lambda}_{ij\Omega}(\omega_\lambda; \rho)/\sin\omega_\lambda$. Since this basis set is con-

centrated in the λ arrangement channel region when ρ is sufficiently large, accurate representation of the surface functions concentrated in the ν and κ channels may require a large number of terms at such values of ρ. To overcome this difficulty, a new basis set is constructed which consists of the union of the basis sets $F^{JM\Pi}_{\lambda i j\Omega}$, $F^{JM\Pi}_{\nu i j\Omega}$ and $F^{JM\Pi}_{\kappa i j\Omega}$. Furthermore, for systems containing either two or three identical atoms we construct symmetrized basis sets which belong to irreducible representations Γ of the P_2 or P_3 permutation groups, respectively. For the three identical atom case, these symmetrized variational basis sets are given by

$$F^{JM\Pi\Gamma}_{ij\Omega}(\zeta_\lambda;\rho)=\sum_{\lambda'} c^{\Gamma}_{\lambda' j} F^{JM\Pi}_{\lambda' ij\Omega}(\zeta_{\lambda'};\rho)\,, \tag{12}$$

where the sum in λ' is over λ, ν and κ, the $c^{\Gamma}_{\lambda' j}$ are easily determined constants, and the sets of angles ζ_ν and ζ_κ are considered to be functions of ζ_λ. The functions $F^{JM\Pi\Gamma}_{ij\Omega}$ will be referred to as primitives to distinguish them from the unsymmetrized basis functions $F^{JM\Pi}_{\lambda ij\Omega}$. The five-dimensional LHSF are now expanded in terms of these primitives:

$$\Phi^{JM\Pi\Gamma}_{n}(\zeta_\lambda;\rho)=\sum_{ij\Omega} a^{J\Pi\Gamma}_{ij\Omega n}(\rho)\, F^{JM\Pi\Gamma}_{ij\Omega}(\zeta_\lambda;\rho)\,. \tag{13}$$

The primitive basis set is not orthogonal, since the variational basis sets with different λ' overlap; therefore, calculation of the $a^{J\Pi\Gamma}_{ij\Omega n}$ coefficients requires the determination of overlap integrals for the variational basis set as well as integrals involving the Hamiltonian. Integration over the three Euler angles θ_λ, ϕ_λ, and ψ_λ is analytic, leaving two-dimensional quadratures to be done numerically. These quadratures are the most expensive part of the entire computation. Any quadrature scheme may be employed; the one we used is discussed in section 3.

Once all of the necessary integrals have been calculated, the $a^{J\Pi\Gamma}_{ij\Omega n}$ coefficients are determined by a generalized eigenvalue–eigenvector procedure. With sufficienty large basis sets, the overlap matrix between the primitives becomes nearly singular as a consequence of near linear dependence; for this reason it was necessary to develop a method for dealing with this situation. The primitive overlap matrix is diagonalized, and eigenvectors corresponding to eigenvalues smaller than a tolerance parameter (for the calculations described below, this parameter was set to zero) are eliminated from consideration. The remaining set of eigenvectors is used to transform the Hamiltonian matrix to yield a new eigenvalue problem from which the linear dependence effects have been removed.

From eqs. (6), (12), and (13), the expansion of the two-dimensional surface functions $\psi^{J\Pi\Gamma}_{n\Omega}(\omega_\lambda,\gamma_\lambda;\rho)$ in terms of the one-dimensional functions $f^{J\lambda}_{ij\Omega}$ can be shown to be

$$\psi^{J\Pi\Gamma}_{n\Omega}(\omega_\lambda,\gamma_\lambda;\rho)=\sum_{ij\Omega'} a^{J\kappa\Gamma}_{ij\Omega' n}\{c^{\Gamma}_{\lambda j}\delta^{\Omega}_{\Omega'}[1+(-1)^{J+\Pi}\delta^{\Omega}_{0}]\mathscr{P}^{\Omega}_{J}(\cos\gamma_\lambda) f^{J\lambda}_{ij\Omega}(\omega_\lambda;\rho)$$

$$+c^{\Gamma}_{\nu j} d^{J\Pi}_{\Omega\Omega'}(\Delta_{\nu\lambda})\,\mathscr{P}^{\Omega'}_{J}(\cos\gamma_\nu) f^{J\nu}_{ij\Omega'}(\omega_\nu;\rho)+c^{\Gamma}_{\kappa j}(-1)^{\Omega+\Omega'} d^{J\Pi}_{\Omega\Omega'}(\Delta_{\lambda\kappa})\,\mathscr{P}^{\Omega'}_{J}(\cos\gamma_\kappa) f^{J\kappa}_{ij\Omega}(\omega_\kappa;\rho)\,. \tag{14}$$

The functions $d^{J\Pi}_{\Omega\Omega}(\Delta)=d^{J}_{\Omega\Omega}(\Delta)+(-1)^{J+\Pi+\Omega} d^{J}_{\Omega,-\Omega}(\Delta)$, where $\mathbf{d}^J$ is the Wigner little d matrix [24], they appear in eq. (14) because of the integration of products of two $\mathscr{D}^{J\Pi}_{ij\Omega}$ functions depending on different Euler angles. The angles $\Delta_{\nu\lambda}$ between the vectors $\boldsymbol{R}_\lambda$ and $\boldsymbol{R}_\nu$ and $\Delta_{\lambda\kappa}$ between the vectors $\boldsymbol{R}_\kappa$ and $\boldsymbol{R}_\lambda$ are functions of ω_λ and γ_λ only.

The same formalism is used in determining the surface functions at values of ρ for which the surface function amplitude is negligible in regions of configuration space in the interstices between the arrangement channel regions. For such values of ρ, the overlap between $f^{J\lambda}_{ij\Omega}$ and $f^{J\nu}_{ij\Omega}$ vanishes, making the set of primitive functions be automatically orthogonal; this greatly reduces the numerical work necessary for the LHSF calculation, because the basis set includes only the λ basis functions.

The calculations of the six-dimensional scattering wavefunction $\Psi^{JM\Pi\Gamma}$ is done by expanding it in terms of the five-dimensional LHSF:

$$\Psi^{JM\Pi\Gamma}(\rho,\zeta_\lambda)=\sum_n b_n^{J\Pi\Gamma}(\rho;\bar\rho)\,\Phi_n^{JM\Pi\Gamma}(\zeta_\lambda;\bar\rho)\,. \tag{15}$$

The $\Phi_n^{JM\Pi\Gamma}$ are determined at a set of discrete values of $\bar\rho$, labeled $\bar\rho_i$. Substituting eq. (15) into the (time-independent) Schrödinger equation corresponding to the Hamiltonian defined by eq. (2) and using eq. (5), the coefficients $b(\rho;\bar\rho_i)$ are found to satisfy

$$\left(-\frac{\hbar^2}{2\mu}\frac{1}{\rho^{5/2}}\frac{d^2}{d\rho^2}\rho^{5/2}+\frac{15\hbar^2}{8\mu\rho^2}+\left(\frac{\bar\rho_i}{\rho}\right)^2\epsilon_n^{J\Pi\Gamma}(\bar\rho_i)-E\right)\delta_n^{n'}\,b_{n'}^{J\Pi\Gamma}(\rho;\bar\rho_i)+\sum_{n'}b_{n'}^{J\Pi\Gamma}(\rho;\bar\rho_i)\,[\mathcal{I}^{J\Pi\Gamma}]_{n'}^{n}(\rho;\bar\rho_i)=0\,, \tag{16}$$

in which the interaction matrix $\mathcal{I}^{J\Pi\Gamma}$ is defined by

$$\begin{aligned}[\mathcal{I}^{J\Pi\Gamma}]_{n'}^{n}(\rho;\bar\rho_i)&=\langle\Phi_n^{JM\Pi\Gamma}(\zeta_\lambda;\bar\rho_i)\,|\,\bar V(\rho,\omega_\lambda,\gamma_\lambda;\bar\rho_i)\,|\,\Phi_{n'}^{JM\Pi\Gamma}(\zeta_\lambda;\bar\rho_i)\rangle\\&=\sum_{\upsilon j\Omega}\sum_{\upsilon' j'\Omega'}a_{\upsilon j\Omega n}^{J\Pi\Gamma}(\bar\rho_i)\,a_{\upsilon' j'\Omega' n'}^{J\Pi\Gamma}(\bar\rho_i)\langle F_{\upsilon j\Omega}^{JM\Pi\Gamma}(\zeta_\lambda;\bar\rho_i)\,|\,\bar V(\rho,\omega_\lambda,\gamma_\lambda;\bar\rho_i)\,|\,F_{\upsilon' j'\Omega'}^{JM\Pi\Gamma}(\zeta_\lambda;\bar\rho_i)\rangle\,,\end{aligned} \tag{17}$$

with $\bar V(\rho,\omega_\lambda,\gamma_\lambda;\bar\rho_i)=V(\rho,\omega_\lambda,\gamma_\lambda)-(\bar\rho_i/\rho)^2V(\bar\rho_i,\omega_\lambda,\gamma_\lambda)$. The integrals in the right-most part of eq. (17) are obtained from linear combinations of related integrals involving the variational basis set (11).

The coefficients $b(\rho;\bar\rho_i)$ are calculated as a function of ρ in a region near $\bar\rho_i$ corresponding to a hyper-spherical shell. The smooth matching of the scattering wavefunction across the boundary $\rho_{i,i+1}$ of adjacent hyper-spherical shells is accomplished by imposing the conditions

$$b_n^{J\Pi\Gamma}(\rho_{i,i+1};\bar\rho_{i+1})=\sum_{n'}b_{n'}^{J\Pi\Gamma}(\rho_{i,i+1};\bar\rho_i)\,[\mathcal{C}^{J\Pi\Gamma}]_{n'}^{n}(\bar\rho_{i+1},\bar\rho_i)\,, \tag{18}$$

$$\left(\frac{\partial b_n^{J\Pi\Gamma}(\rho;\bar\rho_{i+1})}{\partial\rho}\right)_{\rho\to\rho(i,i+1)}=\sum_{n'}\left(\frac{\partial b_{n'}^{J\Pi\Gamma}(\rho;\bar\rho_i)}{\partial\rho}\right)_{\rho\to\rho(i,i+1)}[\mathcal{C}^{J\Pi\Gamma}]_{n'}^{n}(\bar\rho_{i+1},\bar\rho_i)\,, \tag{19}$$

in which the overlap matrices $\mathcal{C}^{J\Pi\Gamma}$ are defined by

$$\begin{aligned}[\mathcal{C}^{J\Pi\Gamma}]_{n'}^{n}(\bar\rho_{i+1},\bar\rho_i)&=\langle\Phi_n^{JM\Pi\Gamma}(\zeta_\lambda;\bar\rho_{i+1})\,|\,\Phi_{n'}^{JM\Pi\Gamma}(\zeta_\lambda;\bar\rho_i)\rangle\\&=\sum_{\upsilon j\Omega}\sum_{\upsilon' j'\Omega'}a_{\upsilon j\Omega n}^{J\Pi\Gamma}(\bar\rho_{i+1})\,a_{\upsilon' j'\Omega' n'}^{J\Pi\Gamma}(\bar\rho_i)\langle F_{\upsilon j\Omega}^{JM\Pi\Gamma}(\zeta_\lambda;\bar\rho_{i+1})\,|\,F_{\upsilon' j'\Omega'}^{JM\Pi\Gamma}(\zeta_\lambda;\bar\rho_i)\rangle\,.\end{aligned} \tag{20}$$

The methodology described above is closely related in spirit to the method independently developed by Schatz [17], which was published after the present work was completed. The major differences are in the selection of reference potential for calculation of the ω_λ-dependent portion of the basis set and in the method for dealing with overcompleteness of the basis set. Our reference potential, denoted by the term V_{ij}^{Ω} in eq. (10), is the potential energy surface at fixed $\bar\rho$ averaged over the diatomic rotation; the choice of this reference potential naturally follows from the expression for the one-dimensional surface functions $\phi_{\upsilon j\Omega}^{J\Pi\Gamma}$ of eq. (8). We allow for the large amount of linear dependence which is produced by this reference potential at small values of $\bar\rho$ by the method for solution of the generalized eigenvalue problem described above. This does not increase the time required for the calculation. Schatz, on the other hand, chooses for his reference potential $V(\bar\rho,\omega_\lambda,\gamma_\lambda=\pi/2)$ for $\bar\rho\geq 3.3$ bohr and $V(\bar\rho=3.3\text{ bohr},\omega_\lambda,\gamma_\lambda=\pi/2)$ for $\bar\rho<3.3$ bohr; the change in the reference potential at small $\bar\rho$ avoids problems with linear dependence.

3. Numerical parameters

One of the most important parameters in the calculations performed is the number of primitives used to expand the surface functions. In addition to the indices J, M, Π and Γ which label the LHSF, the basis functions and the primitives formed from them are labelled by indices υ, j, and Ω, which asymptotically correspond re-

spectively to the diatom vibrational, total rotational and helicity rotational projection quantum numbers [2,3]. The range of (v, j, Ω) included in the calculation of a desired set of LHSF is selected by preliminary calculations at a small subset of the values of $\bar{\rho}$ to be used in the full calculation. For these initial calculations, the basis set is deliberately chosen to be larger than necessary for the accuracy and number of surface functions desired. The number of accurate surface functions obtained by this method is determined by comparison of two such calculations with different size basis sets at each value of $\bar{\rho}$. Examination of the coefficients of the basis functions contributing to each surface function considered allows selection of a smaller basis set which can be used with minimal loss of accuracy. This method becomes complicated with larger variational basis sets, due to increasing linear dependence among some of the primitive functions; however, the overall pattern of important coefficients is still effective in optimizing the choice of basis sets for succeeding calculations. When this method of selection is used, the number of good surface functions of each symmetry which are produced is approximately one half the number of primitives of that symmetry used in the calculation.

To obtain the results presented below, the one-dimensional numerical functions $t^{J\lambda}_{v'j\Omega}(\omega_\lambda;\rho)$ from eq. (10) are calculated on a grid of 450 ω_λ points using a one-dimensional finite element method. Each element is quadratic and uses two Gauss–Legendre points. The reference potential V^{Ω}_{jj} for these functions is determined by a Gauss–Legendre quadrature with 96 γ_λ points. The grid for the two-dimensional integrals is the direct product of these two independent quadrature grids. Convergence of the surface function energies with the fineness of the mesh is to four decimal places.

For the system $H+H_2$, the dependence of the basis functions eq. (11) in the ν and κ coordinates is the same as that for the λ channel functions, so it is not necessary to repeat the calculation for $t^{J\nu}_{v'j\Omega}$ and $t^{J\kappa}_{v'j\Omega}$. In addition, the integrals between products of functions in the λ and ν channels equal the integrals between the corresponding functions in the ν and κ channels, so the integration need only be done for λ,ν pairs to obtain the overlap integrals for all three regions.

LHSF are calculated every 0.2 bohr from $\bar{\rho}=2.0$ to 12.0 bohr, and interaction matrices $\mathcal{J}^{J\Pi\Gamma}$ (see eqs. (16) and (17)) are determined at five evenly spaced values of ρ for every value of $\bar{\rho}_i$. One overlap matrix $\mathcal{C}^{J\Pi\Gamma}$ (see eqs. (18)–(20)) is calculated between sets of the LHSF at each pair of adjacent $\bar{\rho}$ values. For $\bar{\rho}\geq 6.2$ bohr the variational basis functions in arrangement channel λ are orthogonal to those in ν and κ because we set the maximum value of ω_λ equal to the physically reasonable value $2\arcsin(3.0\,\text{bohr}/\bar{\rho})$, which at $\bar{\rho}=6.2$ bohr equals 57.9°. This value of ω_λ is deep in a classically forbidden region for all γ_λ for the total energies discussed below. As a result, the time needed for the surface function calculation in this region is small compared to that for the $\rho<6.2$ bohr region. The initial value problem described by eq. (16) is solved using a logarithmic derivative propagator [27] with a step size of $\Delta\rho=0.025$ bohr and a constant-ρ projection [6,11,28] at 12.2 bohr. These parameters were chosen to achieve a calculation accuracy about equal to that described previously [6,11].

The five-dimensional basis functions are generated from the functions $f^{J\lambda}_{v'j\Omega}$ according to eq. (11). For each of the potential energy surfaces and for $J=0$, a set of $(v, j, \Omega=0)$ quantum numbers was chosen to give a variational basis set of 152 functions. This set has a maximum of 12 vibrational functions for the value $j=0$, with monotonically decreasing number of vibrations for each succeeding value of j to the maximum of $j=23$ for which only one vibrational function is used. Symmetrization of this basis set yielded 76 A_1, 76 A_2 and 152 E primitives.

For the LSTH potential energy surface, the scattering results were obtained from 36 A_1, 35 A_2, and 69 E LHSF at each value of $\bar{\rho}$. The calculation of each LHSF (including the evaluation of all the associated overlap and interaction matrices for the solution of the propagation equation (16)) requires an average of 0.27 s on a Cray X-MP/48. The timings are very similar for the PK2 potential energy surface.

For $J=0$, the variational LHSF calculation is about a factor of 20 faster than the finite-element method one for equivalent accuracy [6,11]. We estimate that the numerical effort required for the finite-element calculation of the LHSF will increase with J as $(J+1)^a$ with $2<a\leq 3$, whereas for the variational method $a\approx 2$; therefore, the speed of the variational LHSF calculation with respect to that of the finite-element one is expected to increase with increasing J.

Table 1
Comparison of surface function energies (in eV) for finite-element (FE) and variational (V) methods – $J=0$

$\bar{\rho}$ (a_0)	PK2								LSTH							
	A1			A2 [a]		E			A1			A2			E		
	n	FE	V	n	V	n	FE	V	n	FE	V	n	FE	V	n	FE	V
2.0	1	3.0031	3.0029	1	3.7612	1	3.1562	3.1558	1	3.1988	3.1987	1	4.0947	4.0937	1	3.3938	3.3935
	5	4.5951	4.5586	5	5.8307	10	5.2093	5.1996	5	4.7962	4.7918	5	6.1193	6.1104	10	5.4317	5.4247
	10	5.8126	5.7980	10	7.1675	20	6.5485	6.5309	10	6.0898	6.0795	10	7.6127	7.5981	20	6.8744	6.8608
	15	6.8547	6.8247	15	8.5371	30	7.7914	7.7361	15	7.2700	7.2574	15	9.1025	9.0699	30	8.1385	8.1159
	20	7.9175	7.8703	20	9.5651	40	8.9223	8.8574	20	8.3031	8.2787	20	10.137	10.088	40	9.3596	9.3065
3.0	1	0.61272	0.61267	1	0.80296	1	0.61277	0.61272	1	0.72438	0.72435	1	0.96023	0.96011	1	0.72440	0.72437
	5	1.1472	1.1463	5	1.3912	10	1.3210	1.3192	5	1.2819	1.2814	5	1.5368	1.5357	10	1.4473	1.4464
	10	1.6735	1.6679	10	2.0120	20	1.8613	1.8573	10	1.7585	1.7550	10	2.1531	2.1463	20	1.9919	1.9877
	15	2.0847	2.0788	15	2.5986	30	2.3244	2.3082	15	2.2466	2.2432	15	2.7673	2.7604	30	2.4375	2.4328
	20	2.5316	2.5219	20	3.0725	40	2.8049	2.7933	20	2.6695	2.6638	20	3.2483	3.2368	40	2.9494	2.9377
4.0	1	0.41158	0.41118	1	0.41563	1	0.41169	0.41129	1	0.43738	0.43713	1	0.44677	0.44658	1	0.43753	0.43728
	5	0.88557	0.88426	5	0.89775	10	0.89821	0.89670	5	0.87687	0.87631	5	0.90314	0.90240	10	0.90160	0.90082
	10	1.2436	1.2413	10	1.3507	20	1.3192	1.3158	10	1.2080	1.2068	10	1.3431	1.3410	20	1.2916	1.2895
	15	1.5936	1.5868	15	1.7777	30	1.6246	1.6193	15	1.5617	1.5583	15	1.7631	1.7583	30	1.6026	1.5994
	20	1.8317	1.8234	20	2.0267	40	1.9527	1.9428	20	1.8025	1.7976	20	1.9981	1.9925	40	1.9166	1.9110
5.0	1	0.32308	0.32230	1	0.33328	1	0.32308	0.32230	1	0.29753	0.29702	1	0.31150	0.31112	1	0.29753	0.29702
	5	0.83267	0.82921	5	0.83878	10	0.84158	0.83878	5	0.79821	0.79600	5	0.80894	0.80723	10	0.80894	0.80723
	10	1.1443	1.1394	10	1.2899	20	1.2973	1.2899	10	1.1107	1.1069	10	1.2614	1.2562	20	1.2614	1.2562
	15	1.4603	1.4506	15	1.6199	30	1.6060	1.5974	15	1.4218	1.4149	15	1.5910	1.5821	30	1.5579	1.5526
	20	1.8092	1.7972	20	1.9166	40	1.8322	1.8190	20	1.7572	1.7510	20	1.8734	1.8665	40	1.7837	1.7756

[a] For PK2 A2 there are no FE data available.

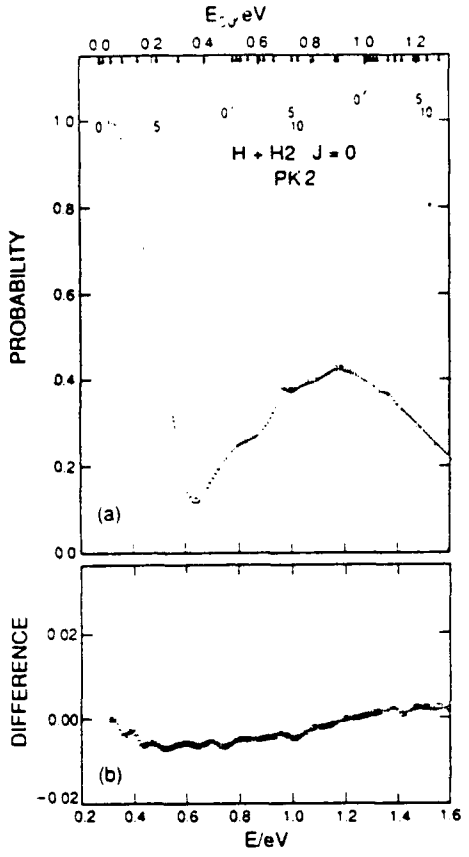

Fig. 1. Probabilities (a) and probability differences (b) as a function of total energy E (lower abscissa) and initial relative translational energy E_{00} (upper abscissa) for the $J=0$ (0, 0, 0) → (0, 0, 0) E symmetry transition in $H+H_2$ collisions on the PK2 potential energy surface. The symbol (v, j, Ω) labels an asymptotic state of the $H+H_2$ system in which v, j and Ω are the quantum numbers of the initial or final H_2 states as defined in the text. The vertical arrows on the upper abscissa denote the energies at which the corresponding $H_2(v, j)$ states open up. The length of those arrows decreases as v spans the values 0, 1, and 2, and the numbers 0, 5, and 10 associated with the arrows define a labelling for the value of j. The square symbols in (a) are the current variational surface function results and the solid line are the FE results [11]. The differences between the former and the latter are plotted in (b).

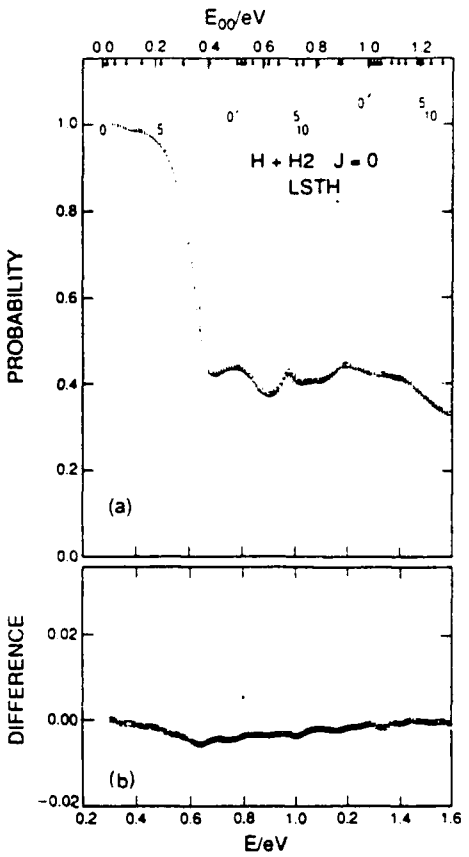

Fig. 2. Same as for fig. 1 for the LSTH potential energy surface. The FE results are taken from ref. [22].

4. Results and discussion

As can be seen in table 1, the present variational (V) LHSF energies consistently fall below those calculated by the finite-element method (FE) [11,23], with a maximum reduction of about 65 meV for the higher energy LHSF. As both methods obey a minimum principle, this implies better quality of the LHSF in the current method.

Flux is conserved for the PK2 surface to better than 1% for energies less than 1.55 eV for the scattering calculations using FE LHSF [11] and for energies below 1.74 eV for the current calculations. For the LSTH surface, flux is conserved to better than 2% below 1.55 eV for the FE results [23] and, for the current results, to better than 1% below 1.68 eV and to better than 2% between 1.68 and 1.74 eV. Examination of the scattering matrices produced by each method shows good agreement between the two below the first resonance at 0.97 eV, with a difference which is usually no greater than 2% for probabilities greater than 10^{-2}. Above this energy the agreement between the results for the $v=0$ to $v'=0$ state transitions remains equally good; however, the agreement for $v=1$ to $v'=1$ transitions is not as good, with a difference usually no greater than 4% in the probabilities greater than 10^{-2} for these transitions. On the basis of the lower LHSF energies and the better scattering matrix unitarities of the current method, we believe that the current scattering calculations are more accurate than the ones using FE LHSF. A comparison of $J=0$ probability curves generated by the two methods is plotted in fig. 1 for the PK2 surface and in fig. 2 for the LSTH surface, together with the difference of the results of the two methods. The relative differences for the probabilities of these figures never exceed 6% for the PK2 or 2% for the LSTH potential energy surface; the greater maximum relative difference for the former is due to the smaller minimum value of the probability itself rather than to a greater difference between the results.

The scattering results calculated from the variational LHSF are converged with respect to number of surface functions used in the propagation to 2% in the probabilities greater than 0.1 and 1.5° in the corresponding scattering matrix element phases. The energies of the LHSF corresponding to asymptotically open states are converged to 0.5% with respect to size of the basis set used in their calculation, and thus the scattering results are also well converged with respect to this parameter.

Calculations were also performed for both parities of the $J=1$ partial wave and are of similar quality. $J=1$ probabilities in excess of 0.1 generally agree with the matching method ones [3] (which were obtained up to 0.7 eV only) to better than about 3%. In none of these calculations have we encountered the difficulties previously predicted [10]. A detailed analysis of the $J=1$ results, up to 1.75 eV, and of the corresponding resonances will be the subject of a separate publication.

5. Summary

A new general variational method for calculating local LHSF was described. It is about a factor of 20 more efficient than the finite-element method for the $J=0$ partial wave of $H+H_2$; this relative efficiency is expected to increase with increasing J. The results of the two methods agree well at the LHSF level, and at the scattering matrix level agree well for energies below 0.97 eV and moderately well for higher energies; the variational ones are believed to be the more accurate ones.

Acknowledgement

The work described in this paper was supported in part by DOE grant DE-AS03-83ER and AFAL contract F04611-86-K-0067. One of the authors (SAC) also thanks NSF for a Graduate Fellowship. Most of the calculations were performed on the Cray X-MP/48 and SCS-40 machines at the NSF San Diego Supercomputing Center.

References

[1] A. Kuppermann and G.C. Schatz, J. Chem. Phys. 62 (1975) 2502.
A. Kuppermann, G.C. Schatz and M. Baer, J. Chem. Phys. 65 (1976) 4596;
G.C. Schatz and A. Kuppermann, J. Chem. Phys. 65 (1976) 4624.
[2] G.C. Schatz and A. Kuppermann, J. Chem. Phys. 65 (1976) 4642.
[3] G.C. Schatz and A. Kuppermann, J. Chem. Phys. 65 (1976) 4668.
[4] A.B. Elkowitz and R.E. Wyatt, J. Chem. Phys. 62 (1975) 2504; 63 (1975) 702.
[5] R.B. Walker, E.B. Stechel and J.C. Light, J. Chem. Phys. 69 (1978) 2922.
[6] A. Kuppermann and P.G. Hipes, J. Chem. Phys. 84 (1986) 5962
[7] F. Webster and J.C. Light, J. Chem. Phys. 85 (1986) 4744.
[8] G.C. Schatz, in: Theory of chemical reactions dynamics, ed. D.C. Clary (Reidel, Dordrecht, 1986) p. 1
[9] M. Baer, J. Phys. Chem. 91 (1987) 5846.
[10] G.A. Parker, R.T Pack, B.J. Archer and R.B. Walker, Chem. Phys. Letters 137 (1987) 564;
R.T Pack and G.A. Parker, J. Chem. Phys. 87 (1987) 3888.
[11] P.G. Hipes and A. Kuppermann, Chem. Phys. Letters 133 (1987) 1.
[12] J. Linderberg and B. Vessal, Intern. J. Quantum Chem. 31 (1987) 65.
[13] D.W. Schwenke, K. Haug, D.G. Truhlar, Y. Sun, J.Z.H. Zhang and D.J. Kouri, J. Phys. Chem. 91 (1987) 6080.
[14] J.Z.H. Zhang and W.H. Miller, Chem. Phys. Letters 140 (1987) 329;
J.Z.H. Zhang, S.-I. Chu and W.H. Miller, J. Chem. Phys. 88 (1988) 4549.
[15] J.Z.H. Zhang, D.J. Kouri, K. Haug, D.W. Schwenke, Y. Shima and D.G. Truhlar, J. Chem. Phys. 88 (1988) 2492.
[16] M. Mladenovic, M. Zhao, D.G. Truhlar, D.W. Schwenke, Y. Sun and D.J. Kouri, Chem. Phys. Letters 146 (1988) 358.
[17] G.C. Schatz, Chem. Phys. Letters 150 (1988) 92.
[18] A. Kuppermann, Chem. Phys. Letters 32 (1975) 374.
[19] R.T. Ling and A. Kuppermann, in: Electronic and Atomic Collisons, Abstracts of Papers of the 9th International Conference on the Physics of Electronic and Atomic Collisions, Seattle, Washington, 24–30 July 1975, Vol. 1, eds. J.S. Risley and R. Geballe (Univ. Washington Press, Seattle, 1975) pp. 353, 354.
[20] R.N. Porter and M. Karplus, J. Chem. Phys. 40 (1964) 1105.
[21] B. Liu, J. Chem. Phys. 58 (1973) 1925;
P. Siegbahn and B. Liu, J. Chem. Phys. 68 (1978) 2457.
[22] D.G. Truhlar and C.J. Horowitz, J. Chem. Phys. 68 (1978) 2468; 71 (1979) 1514 (E).
[23] P.G. Hipes and A. Kuppermann, unpublished results.
[24] L.M. Delves, Nucl. Phys. 9 (1959) 391; 20 (1960) 275.
[25] A. Kuppermann, in: Theoretical chemistry – theory of scattering: papers in honor of Henry Eyring, Vol. 6, part A, ed. D. Henderson (Academic Press, New York, 1981) ch. 2, pp. 70–164.
[26] A.S. Davydov, Quantum mechanics, 2nd Ed. (Pergamon Press, Oxford, 1976) pp. 151–161.
[27] B.R. Johnson, J. Compl. Phys. 49 (1973) 23; J. Chem. Phys. 67 (1977) 4086; NRCC Workshop, Lawrence Berkeley Laboratory, Report No. LBL-9501 (1979).
[28] D.M. Hood and A. Kuppermann, in: Theory of chemical reaction dynamics, ed. D.C. Clary (Reidel, Dordrecht, 1986) pp. 193–214; unpublished results.

SYMMETRY ANALYSIS OF ACCURATE $H+H_2$ RESONANCES FOR LOW PARTIAL WAVES

Steven A. CUCCARO [1], Paul G. HIPES [2] and Aron KUPPERMANN

Arthur Amos Noyes Laboratory of Chemical Physics, Division of Chemistry and Chemical Engineering [3], California Institute of Technology, Pasadena, CA 91125, USA

Received 20 January 1989; in final form 28 February 1989

We have performed accurate quantum mechanical three-dimensional reactive scattering calculations for both parities of the $J=1$ partial wave of the $H+H_2$ system up to total energies of 1.75 eV. The collision lifetime resonance spectra for both $J=0$ and $J=1$ are discussed in terms of the characteristics of the system's potential energy surface and of a simple physical model involving its symmetry properties.

1. Introduction

We have recently developed a new variational technique [1] for calculating the local hyperspherical surface functions (LHSF) necessary for performing three-dimensional (3D) quantum mechanical reactive scattering calculations by the symmetrized hyperspherical coordinate method. We have shown that this technique produces results of similar quality as the finite element (FE) one previously used [2,3], with significantly less numerical effort. Using the LHSF generated by this variational method, we have performed 3D reactive scattering calculations for the $H+H_2$ system on the PK2 [4] and LSTH [5,6] potential energy surfaces for the $J=0$ and both parities of the $J=1$ partial waves. The calculations are of sufficiently high quality for resonance analysis using the collision lifetime matrix formalism [7]. We briefly describe the parameters used in the calculation, and follow with a presentation and analysis of the results. Other recent hyperspherical calculations for $J=1$ $H+H_2$ have been published by Schatz [8] and by Pack, Parker and coworkers [9], over a more limited energy range. In addition, results using different methods have been obtained by Mladenovic et al. [10] and by Zang and Miller [11].

2. Method

The details of the partial wave methodology for arbitrary J and the parameters used for the $J=0$ calculation have been presented previously [1]; therefore, only a few relevant points will be mentioned here. The $J=0$ and $J=1$ calculations use the same values for many numerical parameters: the choice of grid is the same, as are the number and location of the sets of LHSF. The basis set for $J=0$ is formed from a choice of quantum numbers $(v, j, \Omega=0)$ [1,12], yielding a total of 152 functions. This basis is symmetrized according to the irreducible representations of the P_3 symmetry group of $H+H_2$, to give 76 A_1, 76 A_2, and 152 E "primitive" functions. These are used as a variational basis for calculation of the LHSF of the corresponding symmetry. The same set of v and j quantum numbers is used for the $J=1$ calculations; in addition, making Ω equal to both 0 and 1 produces a variational basis set of 292 functions. From these, a primitive basis set is generated consisting of 64 A_1, 76 A_2 and 140 E primitives for the even parity $\Pi=0$ (which for $J=1$ contains only

[1] Work performed in partial fulfillment of the requirements for the Ph.D. Degree in Chemistry at the California Institute of Technology.

[2] Current address: Mail code 206-49, California Institute of Technology, Pasadena, CA 91125, USA.

[3] Contribution No. 7909.

0 009-2614/89/$ 03.50

$\Omega=1$ functions) and another with 140 A_1, 152 A_2 and 292 E primitives for the odd parity $\Pi=1$ (containing both $\Omega=0$ and $\Omega=1$ functions).

The $J=1$ scattering results on the PK2 surface were obtained from 31 A_1, 31 A_2, and 64 E LHSF for $\Pi=0$ and 67 A_1, 62 A_2, and 133 E LHSF for $\Pi=1$. The calculation of each $J=1$ LHSF and all associated matrices used in the logarithmic derivative propagation [13] required an average of 13.1 s on an SCS-40 minisupercomputer, as compared to 6.9 s for $J=0$. Similarly, the $J=1$ scattering calculations for the LSTH surface used 32 A_1, 32 A_2 and 64 E LHSF for $\Pi=0$ and 74 A_1, 70 A_2, and 127 E LHSF for $\Pi=1$, with an average time of 12.5 s per LHSF, compared to 6.6 s for $J=0$. The corresponding maximum deviation from flux conservation is never greater than 1% for the PK2 and 2% for the LSTH surface.

3. Results and discussion

From our irreducible representation scattering matrices we have calculated distinguishable atom $J=1$ state-to-state reaction probabilities over the energy range 0.3 to 1.73 eV for the PK2 potential energy surface. The coupled channel (CC) results published by Schatz at 0.5 and 0.6 eV [8] and ours agree to within 10%, which is reasonable since he used a much smaller basis set than ours. Schatz also made calculations based on the coupled states (CS) approximation using a larger basis set than in this CC method. These CS probabilities are closer to our highly converged values than the CC ones, indicating that the CS approximation for his larger basis set is more accurate than the CC results using his smaller basis set. Our $J=1$ results agree with the LSTH calculations of Zhang and Miller [11] at 1.14 eV to about 2% or better.

We performed lifetime matrix analysis [3,7,14] of each of the matrices $S^{J\Pi\Gamma}$ for $\Gamma=A_1$, A_2, E, $\Pi=0$, 1, and $J=0$, 1. We label the resonances obtained by the notation appropriate for vibrational states of linear triatomic molecules, (v_1, v_2^K, v_3), where v_1, v_2, and v_3 denote respectively the quantum numbers for the symmetric, bend and asymmetric vibrations and K is the quantum number of the vibrational angular momentum [15] [#1]. For the resonance state, v_1, v_2 and v_3 denote approximate constants of the motion; their values are chosen on the basis of the energy spacing of the resonances. In the present paper, as well as in all previous ones using this labeling, it has been customary to set $v_3=0$ [3,16,17], implying that such resonances have no asymmetric stretch character. However, modeling of collinear H_3 resonances (for which only v_1 and v_3 are defined) has shown that they may have significant asymmetric as well as symmetric stretch character. The vibrationally adiabatic model suggests that the lowest collinear H_3 resonance be assigned the quantum numbers $v_1=1$, $v_3=0$ [18], whereas the hyperspherically adiabatic model leads to the assignment $v_1=0$, $v_3=2$ [19,20], corresponding to the second excited state of the asymmetric stretch and asymptotically correlating to the $v=1$ state of the isolated diatom. Therefore, the nodal structures of the corresponding model wavefunctions are completely different, and neither should be assumed correct without further comparison with the accurate resonance wavefunction. The assignment $v_3=0$ used in this paper corresponds to a vibrationally adiabatic description, but is a matter of notation rather than of physical validity.

Lifetime matrix analyses of the $J=0$ scattering matrices for the PK2 surface were previously performed up to 1.6 eV using the FE method for calculating the LHSF [3]. They were recalculated using the variational LHSF approach, and the results are comparable. The resonant time delays and resonance positions found for scattering matrices generated from both FE and variational LHSF are listed in table 1; the lifetime matrix eigenvalues for the current variational LHSF calculation are plotted versus energy in fig. 1. The main difference between the two calculations is the appearance of two weak reso-

[#1] In a previous paper [3] we used Ω to denote the vibrational angular momentum quantum number, in analogy to the notation of refs. [16,17]. However, we have also used Ω [1,3] to denote the quantum number for the component of the system's total angular momentum along the direction of the vector which connects the center of mass of a pair of the system's atoms to the third atom (and asymptotically corresponds to the helicity rotational quantum number). Since these two angular momentum components are in general distinct, we will for clarity use the symbol K in this paper to denote the first one (i.e. the vibrational angular momentum component), while continuing to use Ω for the second.

Table 1
Resonance characteristics for PK2 [a] potential energy surface

J	Assignment	Current results			FE [b] lifetime (fs)	RPO [c] E (eV)
		E (eV)	lifetime (fs)	E (eV)		
0, 1	(0, 0°, 0)	0.61	7	0.61		0.655
1	(0, 1¹, 0)	0.74	6			
0, 1	(0, 2°, 0)	0.85	3	0.847		0.934
0, 1	(1, 0°, 0)	0.97	41	0.971	42	0.975
1	(0, 3¹, 0)	0.97	6			
0, 1	(0, 4°, 0)	1.07	2			
1	(1, 1¹, 0)	1.08	18			
0, 1	(1, 2°, 0)	1.17	7	1.170		1.175
0, 1	(2, 0°, 0)	1.38	46	1.382	50	1.366
1	(2, 1¹, 0)	1.47	35			
0	?	1.51	7			1.542
0, 1	(2, 2°, 0)	1.56	20	1.56		
1	(2, 3¹, 0)	1.65	5			

[a] Ref. [4].
[b] Finite element results, ref. [3].
[c] Resonant periodic orbit results, ref. [21].

nances at energies of 1.07 and 1.51 eV, which were not previously reported. The first is assigned the label (0, 4°, 0); however, the resonance at 1.51 eV, indicated by an unlabeled arrow in fig. 1, does not seem to correspond to the energy of an expected state of metastable linear H_3 and as such will remain unlabeled. The lifetimes of these resonances vary greatly; the long-lived ones at 0.969, 1.381, and 1.56 eV correspond to Feshbach resonances and have lifetimes of 41, 46, and 20 fs, respectively, while the weaker peaks correspond to shape or barrier resonances [21] and have an average lifetime of 6 fs. In both calculations, the A_1 and E symmetries show the same resonance energies and lifetimes, with more numerical noise present in the E calculation due to the larger number of states, and no resonance structure is found in the A_2 symmetry.

The $J=0$ LSTH surface resonance energy and lifetimes from the current calculations and the previous FE calculations are listed in table 2, and the present lifetime matrix eigenvalues are displayed in fig. 2. The assignment of these states is the same as for those found for the PK2 surface. In addition, there is a high energy resonance at 1.72 eV, which corresponds to (2, 4°, 0); however, the lifetime analysis near this energy is obscured by numerical noise, so this energy is less reliable than the other resonance energies.

The energy spacings of each of the $v_2=0$, $v_2=2$ and $v_2=4$ series of resonances suggest that a resonance with assignment (1, 4°, 0) should exist, for the LSTH surface, at the position indicated in fig. 2. So far, this resonance has not been found. By analogy, an equivalent resonance should exist (but is not found) for PK2, as indicated in fig. 1. The latter cannot correspond to the unlabeled resonance at 1.51 eV, because of the insufficiently large spacing between the (0, 4°, 0) and (2, 4°, 0) resonances for the LSTH surface.

The $J=1$ partial wave includes resonance states with $K=1$ in addition to $K=0$. Interestingly, the lifetime matrix analysis of the $J=1$, $\Pi=1$, A_2 symmetry yields the same resonance energies as those found for the $J=0$, A_1 symmetry for both the PK2 and LSTH surfaces, with one exception; we therefore interpret these resonances as $K=0$ states. The exception is that there is no visible A_2 resonance at 1.51 eV for either surface, but it is possible that numerical noise interferes with its detection. The absence of a discernable energy shift due to the increase in J is consistent with the approximate rotational constants for linear H_3 [23]; estimates of the magnitude of the shift in going from $J=0$ to $J=1$ yields a value of about 0.002 eV, which is small compared with the accuracy to which we have determined the resonance energies.

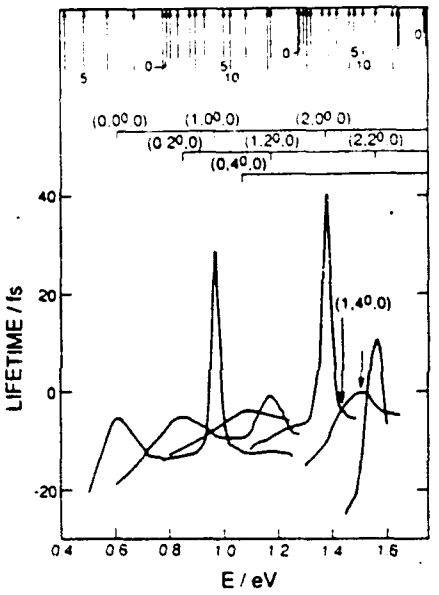

Fig. 1. Resonant lifetime as a function of energy for the A_1 symmetry of the $J=0$ partial wave of $H+H_2$ (PK2 surface). The abcissa E is the total energy and the ordinate represents the resonant eigenvalue of the collision lifetime matrix. The vertical arrows on the upper abcissa denote the energies of the $H_2(v,j)$ states. The length of these arrows decreases as v spans the values 0 through 3. The numbers 0, 5, and 10 define a labeling for the value of j. The energy grid used for these lifetime calculations was 0.001 eV in the neighborhood of the two strongest resonances $(1, 0^0, 0)$ and $(2, 0^0, 0)$ and 0.01 eV elsewhere. The labeling of the resonances at the top of the panel is described in the text. The downward pointing unlabeled vertical arrow at 1.51 eV indicates an unassigned resonance. The downward pointing arrow labeled $(1, 4^0, 0)$ corresponds to a resonance expected on the basis of energy spacings (see text) but not found in the present calculations.

Additional resonances appear in the $J=1$, $\Pi=1$, A_1 and $J=1$, $\Pi=0$, A_2 partial waves. For the PK2 surface, they occur at 0.74, 0.97, 1.08, 1.47, and 1.65 eV (fig. 3). The assignments and lifetimes are given in table 1. The v_1 and v_2 assignments are done on the basis of the energy spacings, and the K assignment on the basis of the restrictions imposed by the values of J and v_2 and the evenness of v_2 [3,25]. The corresponding values for the LSTH surface are listed in table 2 and displayed in fig. 4; they have energies of 0.77, 1.00, 1.09, 1.22, 1.45, and 1.63 eV. The strong resonances $(1, 1^1, 0)$, $(2, 1^1, 0)$ and $(2, 3^1, 0)$ were found previously with approximate models using the LSTH surface [16,17,23,24]; these results are also given in table 2 for comparison. The remaining peaks in the lifetime analysis are weak and have not been reported before. No resonances were found for the $J=1$, $\Pi=0$, A_1 symmetry on either surface. All resonances seen in the $J=1$ A_1 and A_2 symmetries with a particular parity are also seen in the $J=1$ E symmetry of the same parity. Again, the E results are of lower accuracy because of the larger number of states.

Calculations for collinear triatomic systems have previously given strong indications [19] that the characteristics of resonance spectra are closely related to the geometry of potential energy surfaces in the strong interaction region of configuration space, and that it may be possible to infer such geometry from experimentally observed resonance spectra. We will now try to obtain such relation with the $J=0$, 1 resonance at hand. Examination of the energy spacings between consecutive resonances in each of the series $(0, v_2^K, 0)$, $(1, v_2^K, 0)$, and $(2, v_2^K, 0)$ shows them to be nearly constant with respect to v_1 and v_2 and having global averages of 0.104 ± 0.013 and 0.103 ± 0.015 eV for the LSTH and PK2 surfaces, respectively. This correlates very well with the spacings of 0.11 and 0.12 eV predicted from the corresponding bending force constants [6,26] and a harmonic model.

Examining the series $(v_1, 0^0, 0)$ for $v_1=0$, 1, 2 furnishes consecutive resonance energy differences of 0.33 and 0.38 eV for LSTH and 0.36 and 0.41 eV for PK2, whereas a harmonic model based on the symmetric stretch force constant predicts constant spacing of 0.26 eV for LSTH and 0.47 eV for PK2. Not surprisingly, a symmetric stretch static model does not fit the resonance spectra well.

The energy shift between the $(0, 0^0, 0)$ LSTH and PK2 resonances should depend in part on the difference of 0.029 eV between the corresponding saddle point energies [4,6]. The observed downward shift of 0.04 eV can be totally accounted for by the difference in zero point bend energies and saddle point heights; this method of accounting does not seem to be physically reasonable, since the difference in the symmetric and/or asymmetric stretching characteristics of the potential energy surfaces should also contribute to this shift.

We conclude that bending mode force constants in the saddle point region of this system can easily be obtained from the corresponding resonance level spacings, but that static characteristics of the sur-

Table 2
Resonance characteristics for LSTH [a] potential energy surface

J	Assignment	Current results			FE [b] lifetime (fs)	RPO [c] E (eV)	SCSA [d] E (eV)	CEQB [e] E (eV)	CS [f] E (eV)
		E (eV)	lifetime (fs)	E (eV)					
0, 1	$(0, 0^0, 0)$	0.65	11	0.65	11				
1	$(0, 1^1, 0)$	0.77	9						
0, 1	$(0, 2^0, 0)$	0.88	10	0.880	10				
0, 1	$(1, 0^0, 0)$	0.98	28	0.981	28	0.981	0.98	0.97	
1	$(0, 3^1, 0)$	1.00	8						
1	$(1, 1^1, 0)$	1.09	29			1.085	1.09	1.09	1.10
0, 1	$(0, 4^0, 0)$	1.10	5						
0, 1	$(1, 2^0, 0)$	1.19	8	1.191		1.186		1.20	1.20
1	$(0, 5^1, 0)$	1.22	6						
0, 1	$(2, 0^0, 0)$	1.36	30	1.364	31	1.374	1.24	1.35	
1	$(2, 1^1, 0)$	1.45	38			1.461	1.35		
0	?	1.50	4						
0, 1	$(2, 2^0, 0)$	1.54	12	1.55 ± 0.03		1.545	1.46		
1	$(2, 3^1, 0)$	1.63	8			1.641			
0, 1	$(2, 4^0, 0)$	1.72 [g]	5			1.734			

[a] Refs. [5,6]. [b] Ref. [22]
[c] Resonant periodic orbit results, ref. [23].
[d] Small curvature semiclassical adiabatic results, ref. [24].
[e] Collinear exact quantum with adiabatic bend results, ref. [17].
[f] Coupled state results, ref. [16].
[g] This resonance energy is less accurate than the rest. See text for details.

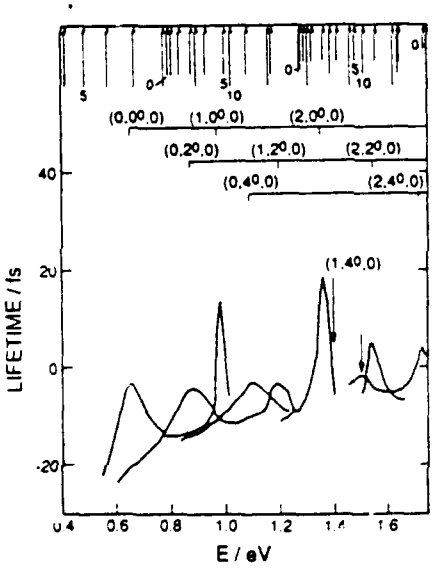

Fig. 2. Same as fig. 1 but for the LSTH surface; a constant energy grid of 0.01 eV was used throughout.

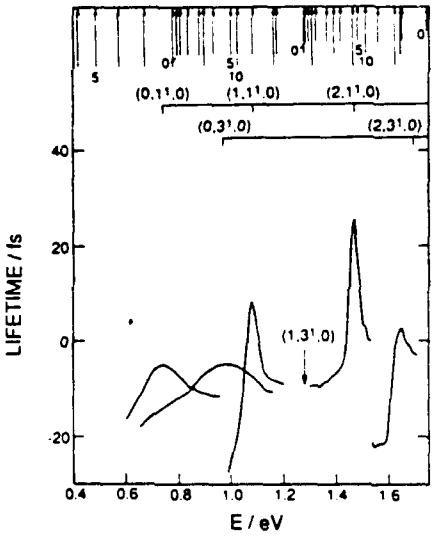

Fig. 3. Resonant lifetime as a function of energy for the A_2 symmetry of the $J=1$, $\Pi=0$ partial wave of $H+H_2$ (PK2 surface). The abcissa and ordinate are as given in fig. 1; the energy grid is 0.01 eV throughout. The downward pointing labeled arrows have similar meanings to the ones in figs. 1 and 2.

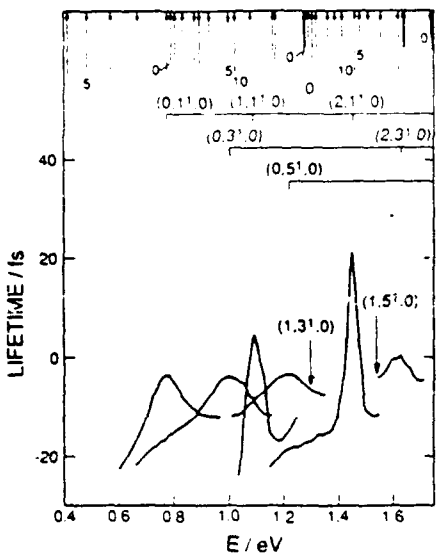

Fig. 4. Same as fig. 3 but for the LSTH surface.

Table 3
Empirical resonance selection rules

J	Π	K	A_1	A_2	E
0	0	0	yes	no	yes
1	0	1	no	yes	yes
1	1	0	no	yes	yes
1	1	1	yes	no	yes

faces are inadequate to understand the stretch motion features of the resonance spectra.

The presence or absence of resonances in each of the partial waves examined is summarized in table 3. An empirical selection rule, satisfied by the results of that table, is that resonances are present in the $\Gamma = E$ symmetry for all allowed values of K, and in $\Gamma = A_1$, A_2 when the quantity $(-1)^{\Pi+K}$ equals X_Γ, where $X_\Gamma = 1$ (-1) for $\Gamma = A_1$ (A_2). This result can be derived from a simple model. According to it, no resonances in the J, Π, Γ partial wave can exist if the scattering wavefunction vanishes identically for all configurations of the system in the vicinity of the saddle point for which the distances of the two end atoms to the central atom are equal. This is physically reasonable since we expect the resonance scattering wavefunction to have large density for symmetric displacements of the system around the saddle point.

Let us now show how this model leads to the empirical rule just mentioned. Let ABC be a linear triatom for which atoms A and C are identical. Consider a bent configuration of this system in which the distances AB and BC are equal. Let X_Γ be the eigenvalue of the operator which permutes A and C, which is equal to 1 for $\Gamma = A_1$ and to -1 for $\Gamma = A_2$. This permutation is equivalent to the product of the inversion operator and a rotation by π around the system's principle axis of inertia, and therefore application of these operations multiplies the triatom wavefunction by $(-1)^\Pi$ and $(-1)^K$, respectively. Since the wavefunction of the initial symmetric configuration cannot by assumption vanish identically if a resonance is to exist, we must have $X_\Gamma = (-1)^{\Pi+K}$, QED. For a system in which all three atoms are identical, neither of the two degenerate E symmetry wavefunctions is necessarily even or odd with respect to two-atom permutations, and when one of these wavefunctions is subjected to this permutation the result is a linear combination of both; thus the E symmetry should display the resonances found in both the A_1 and A_2 symmetry results of the same parity, as we have indeed observed.

The existence of resonances seems also to require the presence of minima in adiabatic curves as a function of an appropriate reaction coordinate [18–20,27–33]. In the particular case of hyperspherical coordinates, one examines LHSF energies including adiabatic correction terms as a function of ρ; these correction terms are large for the $H + H_2$ system. Plots of LSHF energies for the $J = 0$, 1 partial waves of each parity and symmetry do indeed show minima (even without corrections) for the symmetry–parity combinations which support resonances, but not for those combinations which have shown no resonances. A physical interpretation of the resonances depends, in addition to the symmetry arguments given above, on an explanation as to why these particular combinations of irreducible representation and inversion parity yield adiabatic energy versus ρ curves with minima.

4. Summary

Application of the variational method for calculation of LHSF to the $J = 1$ partial wave of $H + H_2$

yields results of sufficient quality for lifetime matrix analysis to give accurate resonance energies and lifetimes. The dependence of resonance energies on the bending mode characteristics of the system's potential energy surface is explained by a simple harmonic model, and the existence of patterns of resonant behavior in terms of the irreducible representations of the P_3 permutation group is interpreted using a simple physical picture.

Acknowledgement

The work described in this paper was supported in part by DOE grant DE-AS03-83ER and AFAL contract F04611-86-K-0067. One of the authors (SAC) also thanks NSF for a Graduate Fellowship. Most of the calculations were performed on the Cray X-MP/48 and SCS-40 machines at the NSF San Diego Supercomputing Center.

References

[1] S.A. Cuccaro, P.G. Hipes and A. Kuppermann, Chem. Phys. Letters 154 (1989) 155.
[2] A. Kuppermann and P.G. Hipes, J. Chem. Phys. 84 (1986) 5962.
[3] P.G. Hipes and A. Kuppermann, Chem. Phys. Letters 133 (1987) 1.
[4] R.N. Porter and M. Karplus, J. Chem. Phys. 40 (1964) 1105.
[5] B. Liu, J. Chem. Phys. 58 (1973) 1925;
P. Siegbahn and B. Liu, J. Chem. Phys. 68 (1978) 2457.
[6] D.G. Truhlar and C.J. Horowitz, J. Chem. Phys. 68 (1978) 2468; 71 (1979) 1514 (E).
[7] F.T. Smith, Phys. Rev. 118 (1960) 349.
[8] G.C. Schatz, Chem. Phys. Letters 150 (1988) 92.
[9] G.A. Parker, R.T Pack, B.J. Archer and R.B. Walker, Chem. Phys. Letters 137 (1987) 564;
R.T Pack and G.A. Parker, J. Chem. Phys. 87 (1987) 3888.
[10] M. Mladenovic, M. Zhao, D.G. Truhlar, D.W. Schwenke, Y. Sun and D.J. Kouri, Chem. Phys. Letters 146 (1988) 358.
[11] J.Z.H. Zhang and W.H. Miller, Chem. Phys. Letters 153 (1988) 465.
[12] G.C. Schatz and A. Kuppermann, J. Chem. Phys. 65 (1976) 4642; 4668.
[13] B.R. Johnson, J. Compl. Phys. 49 (1973) 23.
[14] D.M. Hood and A. Kuppermann, in: Theory of chemical reaction dynamics, ed. D.C. Clary (Reidel, Dordrecht, 1986) pp. 193–204; unpublished results.
[15] G. Herzberg, Infrared and Raman spectra of polyatomic molecules (Van Nostrand, Princeton, 1945) p. 272.
[16] M.C. Colton and G.C. Schatz, Chem. Phys. Letters 124 (1986) 256.
[17] J.M. Bowman, Chem. Phys. Letters 124 (1986) 260.
[18] B.C. Garrett and D.G. Truhlar, J. Phys. Chem. 86 (1982) 1136.
[19] A. Kuppermann, Reactive scattering resonances and their physical interpretation, in: potential energy surfaces and dynamics calculations, ed. D.G. Truhlar (Plenum Press, New York, 1981) ch. 16.
[20] J. Römelt, J. Chem. Phys. 79 (1983) 197.
[21] E. Pollak, Chem. Phys. Letters 137 (1987) 171.
[22] P.G. Hipes, Three-Dimensional Atom–Diatom Reactive Scattering Calculations Using Symmetrized Hyperspherical Coordinates, Ph.D. Thesis, California Institute of Technology (1988); unpublished results.
[23] E. Pollak, J. Phys. Chem. 90 (1986) 3619.
[24] B.C. Garrett, D.W. Schwenke, R.T. Skodje, D. Thirumalai, T.C. Thompson and D.G. Truhlar, Bimolecular reactive collisions, adiabatic and nonadiabatic methods for energies, lifetimes, and branching probabilities, in: Resonances, ACS Symp. Ser. Vol. 263 (Am. Chem. Soc., Washington, 1984) p. 375.
[25] G. Herzberg, Infrared and Raman spectra of polyatomic molecules (Van Nostrand, Princeton, 1945) p. 80.
[26] A.B. Elkowitz and R.E. Wyatt, J. Chem. Phys. 62 (1975) 2504; 63 (1975) 702.
[27] A. Kuppermann and J.P. Dwyer, in: Electronic and atomic collisions, Abstract of Contributed Papers, XIth International Conference on the Physics of Electronic and Atomic Collisions, eds. K. Takayanagi and N. Oda (Society for Atomic Collision Research, Japan, 1979) pp. 888, 889.
[28] G. Hauke, J. Manz and J. Römelt, J. Chem. Phys. 73 (1980) 5040.
[29] J.A. Kaye and A. Kuppermann, Chem. Phys. Letters 77 (1981) 573.
[30] V.K. Babamov and R.A. Marcus, J. Chem. Phys. 74 (1981) 1790.
[31] J.M. Launay and B. Lepetit, Chem. Phys. Letters 144 (1988) 346.
[32] J.M. Launay and M. Le Dourneuf, J. Phys. B 15 (1982) L455.
[33] B. Lepetit, M. Le Dourneuf, J.M. Launay and F.X. Gadea, Chem. Phys. Letters 135 (1987) 377.

CALCULATION OF BOUND ROVIBRATIONAL STATES ON THE FIRST ELECTRONICALLY EXCITED STATE OF THE H_3 SYSTEM

B. LEPETIT [1], Z. PENG [2] and A. KUPPERMANN [3]

Arthur Amos Noyes Laboratory of Chemical Physics, Division of Chemistry and Chemical Engineering, California Institute of Technology, Pasadena, CA 91125, USA

Received 25 October 1989; in final form 4 December 1989

The bound rovibrational states of the upper manifold of the two lowest electronic states of H_3 have been calculated using variational and hyperspherical coordinate propagation methods, neglecting in both the coupling between those electronic states. Inclusion of the effect of the geometric phase induced by the conical intersection between those manifolds (sometimes referred to as the molecular Aharonov–Bohm effect) is shown to change significantly the number, the energies and the wavefunctions of those bound rovibrational states. Quantum numbers are defined which permit a physical understanding of these changes.

1. Introduction

The Rydberg spectrum of the H_3 system has been extensively studied by Herzberg and coworkers [1]. Of particular interest is the experimental discovery of a long-lived metastable state [1–3]. On the theoretical side, investigations have been restricted to the calculation of electronic energies for a few nuclear geometries [4–7], but the complete electronic potential energy surfaces, necessary to investigate the rovibrational structures of the spectrum and to compute accurately the lifetimes of the excited states, are available only for the ground and the first electronically excited states (DMBE potential [8]). In the equilateral triangular nuclear configuration, these two electronic states are degenerate and their electronic wavefunctions belong to the $^2E'$ representation of the D_{3h} group. Displacement away from the equilateral triangular geometry lifts this degeneracy and generates a conical intersection between two Jahn–Teller sheets [9]. Whereas the lower sheet is responsible for $H+H_2$ reactive scattering below about 3 eV [10–17], the upper one supports rovibrational quasi-bound states, which can predissociate by rovibronic coupling to the ground electronic state [18,19].

In this Letter, we assume that the upper Jahn–Teller sheet is decoupled from the lower one and therefore supports bound rovibrational states. We compare two methods of computing these states on the DMBE excited potential energy surface. One is the variational method of Tennyson and Sutcliffe [20,21] (referred to as TS method in this paper). The other, described in section 2, is a hyperspherical propagation method which uses modified Whitten–Smith coordinates [22,23] and derives from reactive scattering theory [10–13,24]. It generalizes earlier molecular bound state calculations limited to $J=0$ [25,26]. We show in section 3 that the hyperspherical method is very appropriate to the H_3 system because:

- It allows easy inclusion of the full permutation symmetries of the three identical nuclei, whereas the TS method only allows inclusion of the permutation symmetries of two identical atoms.
- It permits inclusion of the effect of the conical intersection on the phase of the nuclear wavefunction [27–29]. This effect results from the sign change of the electronic wavefunction as one follows a closed path in the

[1] Permanent address: UPR 261 du CNRS, Observatoire de Paris, 92195 Meudon, France.

[2] Work performed in partial fulfillment of the requirements for the Ph.D. Degree in Physics at the California Institute of Technology.

[3] Contribution No. 8052.

nuclear configuration space around the line along which the two $^2E'$ electronic states conically intersect. It corresponds to a particular case of Berry's geometric phase [30] which has been experimentally observed in the Na_3 system [31]. Since the total electronuclear wavefunction is continuous and single valued, there has to be a compensating sign change in the nuclear part of the wavefunction, which can be included easily in the hyperspherical method. The effect of the conical intersection on the phase of the nuclear wavefunction is sometimes referred to as the molecular Aharonov–Bohm effect [28,29,32], but we will use the simpler name "geometric phase" in the following.

2. Hyperspherical method

Let A_α, A_β, A_γ be the atoms of the system, and (λ, ν, κ) be any cyclic permutation of (α, β, γ). $\boldsymbol{r}_\lambda$ is the mass-scaled [33] internuclear vector for the diatom $A_\nu A_\kappa$ and $\boldsymbol{R}_\lambda$ the mass-scaled vector of A_λ with respect to the center of mass of $A_\nu A_\kappa$. The hyperspherical method uses the hyperradius $\rho = (R_\lambda^2 + r_\lambda^2)^{1/2}$ to describe the global size of the triatomic system and a set of five angles ζ to describe its shape and orientation in space [10–13,22,23,33,34]. In this paper, we will neglect all spin–orbit and spin–spin interactions. In the Born–Oppenheimer approximation, the electronuclear wavefunction can be written as a product of the electronic part ψ_e, which we choose to be real, and the nuclear part. The latter can be factored into a nuclear spin part and a spacial part $\psi^{JM\Pi\Gamma}$. J is the total nuclear angular momentum quantum number, M its projection onto a laboratory-fixed axis, Π the parity with respect to the inversion of nuclear coordinates and Γ the irreducible representation of the nuclear permutation group (P_3) to which $\Psi^{JM\Pi\Gamma}$, the electronuclear wavefunction excluding the nuclear spin part, belongs:

$$\Psi^{JM\Pi\Gamma} = \psi^{JM\Pi\Gamma}(\rho, \zeta)\, \psi_e(q_e; \rho, \zeta)\,. \tag{1}$$

q_e refers to the set of all, spacial and spin, electronic coordinates. $\psi^{JM\Pi\Gamma}$ is an eigenfunction of the nuclear motion Hamiltonian:

$$H = -\frac{\hbar^2}{2\mu}\rho^{-5}\frac{\partial}{\partial\rho}\rho^5\frac{\partial}{\partial\rho} + \frac{\hat{\Lambda}^2}{2\mu\rho^2} + V(\rho, \zeta)\,, \tag{2}$$

where μ is the three-body reduced mass, $\hat{\Lambda}$ the grand canonical angular momentum and V the Born–Oppenheimer electronic potential energy function. The nuclear function $\psi^{JM\Pi\Gamma}$ is expanded in a basis of local hyperspherical surface functions (LHSF) $\Phi_n^{JM\Pi\Gamma}$:

$$\psi^{JM\Pi\Gamma}(\rho, \zeta) = \frac{1}{\rho^{5/2}}\sum_n F_n^{J\Pi\Gamma}(\rho)\, \Phi_n^{JM\Pi\Gamma}(\zeta; \rho)\,. \tag{3a}$$

The LHSF are defined as the eigenfunctions of the fixed hyperradius nuclear Hamiltonian:

$$\left(\frac{\hat{\Lambda}^2}{2\mu\rho^2} + V(\rho, \zeta)\right)\Phi_n^{JM\Pi\Gamma}(\zeta; \rho) = \epsilon_n^{J\Pi\Gamma}(\rho)\; \Phi_n^{JM\Pi\Gamma}(\zeta; \rho)\,. \tag{3b}$$

The coefficients $F_n^{J\Pi\Gamma}$ in eq. (3a) are solutions of a set of coupled differential equations in ρ, which we solve using piece-wise diabatic bases [10,34]. For assumed values of the rovibrational energies, the solutions are propagated forward and backward from small and large ρ values where they have negligible amplitudes. The energy is scanned iteratively until the quantization condition that the forward and backward solutions match smoothly at an intermediate value of ρ is reached.

In the present study, we use the Whitten–Smith [22] definition of the five angular coordinates ζ as modified by Johnson [23]. Three Euler angles $(\alpha\beta\gamma)$ specify the orientation of the body frame in space. The axes of this frame lie along the principle axes of inertia: the Z axis is parallel to $\boldsymbol{r}_\lambda \times \boldsymbol{R}_\lambda$ and the X axis is associated to

the smallest moment of inertia and is oriented such that $r_{\lambda X} \geq 0$. Two angles $(\theta, \varphi_\lambda)$ describe the shape of the molecular triangle and are defined by

$$r_{\lambda X} = \rho \cos(\pi/4 - \theta/2) \sin(\varphi_\lambda/2) , \tag{4a}$$

$$r_{\lambda Y} = -\rho \sin(\pi/4 - \theta/2) \cos(\varphi_\lambda/2) , \tag{4b}$$

$$R_{\lambda X} = \rho \cos(\pi/4 - \theta/2) \cos(\varphi_\lambda/2) , \tag{4c}$$

$$R_{\lambda Y} = \rho \sin(\pi/4 - \theta/2) \sin(\varphi_\lambda/2) . \tag{4d}$$

The ranges for these angles are $0 \leqslant \theta \leqslant \pi/2$ and $0 \leqslant \varphi_\lambda \leqslant 2\pi$. $\theta = 0$ corresponds to the symmetric top configuration (an equilateral triangle for three identical particles) in which the principal axes of inertia X and Y are undefined.

The grand canonical angular momentum is given explicitly by [22,23]

$$\hat{\Lambda}^2 = -4\hbar^2 \left(\frac{1}{\sin 2\theta} \frac{\partial}{\partial \theta} \sin 2\theta \frac{\partial}{\partial \theta} + \frac{1}{\sin^2\theta} \frac{\partial^2}{\partial \varphi_\lambda^2} \right) + \frac{4i\hbar \cos\theta}{\sin^2\theta} \hat{J}_Z \frac{\partial}{\partial \varphi_\lambda} + \frac{2(\hat{J}^2 - \hat{J}_Z^2)}{\cos^2\theta} + \frac{\hat{J}_Z^2}{\sin^2\theta} + \frac{\sin\theta}{\cos^2\theta} (\hat{J}_+^2 + \hat{J}_-^2) , \tag{5}$$

where $\hat{J}_Z$ is the body-fixed Z component of the total angular momentum $\hat{J}$, and $\hat{J}_\pm = \hat{J}_X \pm i\hat{J}_Y$.

Eq. (3b) is solved variationally by expansion in a body-fixed basis $\chi^{JMK}_{n\theta n_\varphi}$ built with products of simple analytical functions [13]:

$$\chi^{JMK}_{n\theta n_\varphi} = \exp(i n_\varphi \varphi_\lambda) f_{n_\theta}(\theta) D^J_{MK}(\alpha\beta\gamma) , \tag{6}$$

D^J_{MK} is a Wigner rotation matrix [35] and n_φ is integer or half of an odd integer. $f_{n_\theta}(\theta)$ are simple trigonometric functions, such that the LHSF have correct behaviors near the singularities of the kinetic energy operator $\theta = 0$ and $\pi/2$. In practice, the f_{n_θ} can be chosen as the functions $\cos(n_\theta\theta)$ or $\sin(n_\theta\theta)$, with n_θ integer or half odd integer, in terms of which the hyperspherical harmonics (whose θ dependence is usually written as a polynomial in $\cos\theta$) can be written (eq. (31) in ref. [36], eqs. (20)–(23) in ref. [37] or eq. (32) in ref. [38]).

We now focus attention on the special case of three identical nuclei and we describe how to build electronuclear wavefunctions $\Psi^{JM\Pi\Gamma}$ which are bases for the irreducible representations of the permutation group of the nuclei (P_3). The operations of this group correspond to simple changes in φ_λ (which are related to the *isomorphism between* P_3 *and* C_{3v}) as indicated in table 1. If $\epsilon^e_{\nu\kappa}$ ($= \pm 1$) is the symmetry of the electronic wavefunction with respect to the $\nu \leftrightarrow \kappa$ permutation, then the linear combinations defined by

$$\chi^{JMK\epsilon^{en}_{\nu\kappa}}_{n\theta|n_\varphi|} = \chi^{JMK}_{n\theta|n_\varphi|} + \epsilon^{en}_{\nu\kappa} \epsilon^e_{\nu\kappa} (-1)^{J+K+2n_\varphi} \chi^{JM,-K}_{n\theta,-|n_\varphi|} , \tag{7}$$

give electronuclear wavefunctions $\Psi^{JM\Pi\Gamma}$ (eq. (1)) with the $\epsilon^{en}_{\nu\kappa}$ ($= \pm 1$) symmetry with respect to the $\nu \leftrightarrow \kappa$ permutation.

If there is no conical intersection between electronic states, the electronic wavefunction $\psi_e(q_e; \rho, \zeta)$ belongs to a one-dimensional representation of the nuclear permutation group (A_1 for $\epsilon^e_{\nu\kappa} = +1$, or A_2 for $\epsilon^e_{\nu\kappa} = -1$). Table 2 indicates how the total angular momentum, the parity and the irreducible representation Γ of P_3 to which $\Psi^{JM\Pi\Gamma}$ belongs determines the set of quantum numbers n_φ.

Table 1
Effect of permutations of the nuclei on the angle φ_λ

Permutation	$P_{\lambda\nu\kappa}$ [a]	$P_{\nu\kappa\lambda}$ [b]	$P_{\kappa\lambda\nu}$ [c]	$P_{\nu\kappa}$ [d]	$P_{\lambda\nu}$ [d]	$P_{\lambda\kappa}$ [d]
value of φ_λ [e]	φ_λ	$\varphi_\lambda + 2\pi/3$	$\varphi_\lambda + 4\pi/3$	$2\pi - \varphi_\lambda$	$2\pi/3 - \varphi_\lambda$	$4\pi/3 - \varphi_\lambda$

[a] $P_{\lambda\nu\kappa}$ is the identity permutation. [b] $P_{\nu\kappa\lambda}$ refers to the cyclic permutation $\lambda\nu\kappa \rightarrow \nu\kappa\lambda$. [c] $P_{\kappa\lambda\nu}$ refers to the cyclic permutation $\lambda\nu\kappa \rightarrow \kappa\lambda\nu$.
[d] P_{ij} refers to the pairwise permutation of nuclei i and j.
[e] The changes in φ_λ are true modulo 2π, since φ_λ must remain in the range $[0, 2\pi]$.

Table 2
Choice of n_φ for each parity Π and irreducible representation Γ of the nuclear permutation group P_3

Π	Γ [c]	n_φ
even, without phase [a]	A_1/A_2	$3m$ [d]
odd, with phase [b]	E	$3m\pm1$ [d]
even, with phase [b]	A_1/A_2	$3m+\frac{1}{2}$ [d]
odd, without phase [a]	E	$3m\pm\frac{1}{2}$ [d]

[a] Without consideration of the geometric phase due to the conical intersection.
[b] With consideration of the geometric phase due to the conical intersection.
[c] Γ is the irreducible representation of P_3 to which $\Psi^{JM\Pi\Gamma}$ (see text and eq. (1)) belongs.
[d] m is a non-negative integer.

If there is a conical intersection between electronic states for equilateral triangular configurations of the nuclei and if the geometric phase is taken into account, one can show [27–29] that in the vicinity of the conical intersection ($\theta=0$), the φ_λ dependence of the Born–Oppenheimer electronic wavefunction is given by

$$\psi_e \approx \cos(\varphi_\lambda/2)\,\psi_e^{E_1} - \sin(\varphi_\lambda/2)\,\psi_e^{E_2} \quad (\epsilon^c_{\nu\kappa}=-1)\,, \tag{8a}$$

or

$$\psi_e \approx \cos(\varphi_\lambda/2)\,\psi_e^{E_2} + \sin(\varphi_\lambda/2)\,\psi_e^{E_1} \quad (\epsilon^c_{\nu\kappa}=+1)\,, \tag{8b}$$

where $(\psi_e^{E_1}, \psi_e^{E_2})$ are two degenerate ρ-dependent but φ_λ-independent states at $\theta=0$ which form a basis for the E irreducible representation of P_3 ($\psi_e^{E_1}$ being symmetric for the $\nu\leftrightarrow\kappa$ permutation and ψ^{E_2} antisymmetric). Although permutations of the nuclei can only change the sign of ψ_e, these Born–Oppenheimer *electronic* wavefunctions do not belong to a one-dimensional irreducible representation of P_3 and are discontinuous in the internal configuration space [39] in the plane $\varphi_\lambda=0$. However, continuous *electronuclear* wavefunctions which belong to irreducible representations of P_3 can be built if the new set of n_φ indicated in table 2 is used for the *nuclear* wavefunctions.

3. Results

Fig. 1 illustrates the main features of the electronic potential in the internal configuration space defined in

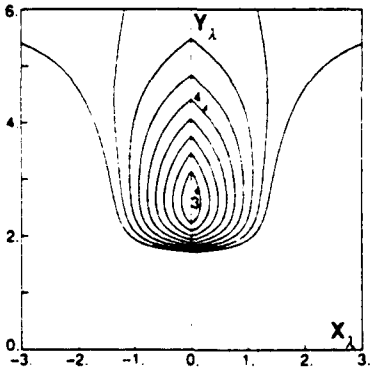

Fig. 1. Plot of the DMBE excited electronic potential V in the internal configuration space defined in ref. [39] along the plane $\varphi_\lambda=\pi/2, 3\pi/2$ (i.e. $Z_\lambda=0$). In this space, the coordinates $(\rho, \theta, \varphi_\lambda)$ defined in the text correspond to spherical polar coordinates with respect to the Y_λ axis of the figure. This axis is also the one along which the excited DMBE potential conically intersects the lower one. The equipotentials are equally spaced by 0.25 eV in the range [3, 5 eV]. The contours for $V=3$ and 4 eV are specifically indicated. The distances on the X_λ and Y_λ axes are in bohr. Along constant Y_λ lines, V shows the usual "V"-shaped behaviour characteristic of conical intersections. The approximate constancy of the X_λ spacing between the equipotentials in this figure is a manifestation of this linear dependence. Equipotentials on cuts along other planes containing the Y_λ axis look, in the vicinity of this axis, very similar to the ones displayed in this figure, i.e. V has a local nearly cylindrical symmetry around Y_λ.

ref. [39]. It has a quasi-cylindrical symmetry around the Y_A axis of that figure ($\theta=0$) which corresponds to the axis of the conical intersection and to the local minima on the fixed ρ spheres. It has an absolute minimum for $\rho=2.6$ bohr, $\theta=0$ corresponding to an energy of 2.72 eV with respect to the bottom of the ground electronic state H_2 well. In the vicinity of that minimum, the potential increases steeply and almost linearly as a function of θ, but more slowly as a function of ρ.

Table 3 compares the rovibrational energy levels for this potential obtained by the hyperspherical method and the TS variational method without consideration of the geometric phase.

The hyperspherical method uses 20 n_θ values, between 4 (A_1 and A_2 symmetry) and 8 (E symmetry) $|n_\varphi|$ values (eqs. (6) and (7)), between 6 (A_1 or A_2 symmetry) and 12 (E symmetry) LHSF (eq. (3)). The LHSF have been computed at typically 50 ρ values between 1.5 and 6.5 bohr. The convergence of the LHSF and rovibrational energies is of the order of 10^{-4} eV. The compactness of the hyperspherical expansion comes from the quasi-cylindrical symmetry of the potential around the $\theta=0$ line (small number of n_φ values) and from the steep increase of the potential as a function of θ (small number of LHSF).

The TS method uses a body frame with its Z axis in the direction of R_A and computes the bound states variationally by expansion on a product basis of two Morse-like functions (in R_A and r_A) for the radial part and of associated Legendre functions for the angular part. The optimized parameters of the Morse potential which we chose are indicated in table 4. Nearly 1400 such product functions have been used for each J, each inversion parity Π and each of the two symmetries for the permutation of the two identical atoms ν and κ. This unusually large number of basis functions (only 880 such functions were used to get fully converged results on H_3^+ in ref. [40]) is required by the shape of the potential and the sudden change of its derivative in the vicinity of the conical intersection axis. Table 3 shows that the convergence of the energy levels is always worse with the TS method than with the hyperspherical method. The quality of the TS calculation for $J=1$ odd parity is not

Table 3
Bound state energies without consideration of the geometric phase [a]

v_1v_2l [b]	$J=0$ [c]			$J=1$ even parity [c]			$J=1$ odd parity [c]		
0 0 0	3.7210	A_1	3.7218	3.7283	A_2	3.7294	3.7264	E	3.7276
1 0 0	3.9216	A_1	3.9223	3.9284	A_2	3.9297	3.9266	E	3.9281
2 0 0	4.1067	A_1	4.1073	4.1130	A_2	4.1145	4.1114	E	4.1131
3 0 0	4.2759	A_1	4.2766	4.2817	A_2	4.2849	4.2802	E	4.2831
4 0 0	4.4282	A_1	4.4301	4.4336	A_2	4.4386	4.4322	E	4.4398
5 0 0	4.5621	A_1	4.5734	4.5665	A_2	4.5803	4.5656	E	4.5894
0 1 1	4.2886	E	4.2886	4.2955	E	4.2956	4.2971	A_1	4.2975
							4.2969	A_2	4.2972
							4.2904	E	4.2908
1 1 1	4.4533	E	4.4533	4.4596	E	4.4598	4.4610	A_1	4.4618
							4.4608	A_2	4.4615
							4.4550	E	4.4557
2 1 1	4.5980	E	4.5983	4.6036	E	4.6048	4.6049	A_1	4.6083
							4.6047	A_2	4.6093
							4.5996	E	4.6028
3 1 1	4.7212	E		4.7261	E	4.7349	4.7272	A_1	4.7370
							4.7270	A_2	4.7355
							4.7225	E	
0 2 0	4.6806	A_1	4.6813	4.6871	A_2	4.6893	4.6842	E	4.6878

[a] The energy is in eV and its origin corresponds to the bottom of the ground electronic state of the isolated H_2 molecule.
[b] Quantum numbers used to classify the states (see text)
[c] The left column gives the hyperspherical method results and the right column the TS method results. The central column gives the irreducible representation of the permutation group of the nuclei to which the spacial part of the nuclear wavefunction belongs.

Table 4
Optimized parameters of the Morse-like functions in R_λ and r_λ

	D_e (au) [a]	ω_e (au) [a]	r_e (au) [a]
$J=0$	0.230 [b]	0.0130 [b]	1.96 [b]
$J=1$	0.262 [b]	0.0100 [b]	2.01 [b]
$J=0$	0.262 [c]	0.0122 [c]	2.09 [c]
$J=1$	0.232 [c]	0.0102 [c]	2.32 [c]

[a] These parameters are defined in eqs. (19) and (20) of ref. [20].
[b] Parameters for the Morse-like functions in R_λ.
[c] Parameters for the Morse-like functions in r_λ.

as good as the TS calculation for $J=0$ since the global size of the basis has been kept constant instead of being doubled. For a given total angular momentum and parity, the quality of the TS results decreases as the energy increases, and in particular, states diffuse along ρ (corresponding to high v_1 values, see below) are poorly represented. This suggests that different sets of optimized parameters of the Morse-like functions should be used for compact and diffuse states.

The hyperspherical method can be compared with the TS method from computational and formal points of view:

– The hyperspherical method requires less memory: smaller basis sets can be used for the variational solution of the two-dimensional LHSF equation (see eq. (3b)) than for the three-dimensional variational solution of the bound states in the TS method. However, the hyperspherical method required about two times more CPU time than the TS method, since the computation of the LHSF has to be repeated many times, but did not exceed 40 min of total CPU time on an SCS-40 for a typical run $J=0$, A_1 plus E permutation symmetries. In addition, the hyperspherical method does not involve adjustable parameters which have to be optimized in the TS method.

– The bases used in the TS method to expand the bound state wavefunctions do not have the P_3 permutation symmetry, but only the P_2 symmetry of two identical nuclei. As a result, plots of the bound state wavefunctions show that, even in the $J=0$ case where the energy convergence is better than 10^{-3} eV, the shape of the TS wavefunctions do not exhibit the correct symmetry properties of a system of three identical particles, whereas they are imbedded in the LHSF basis used in the hyperspherical method. Moreover, the TS method does not

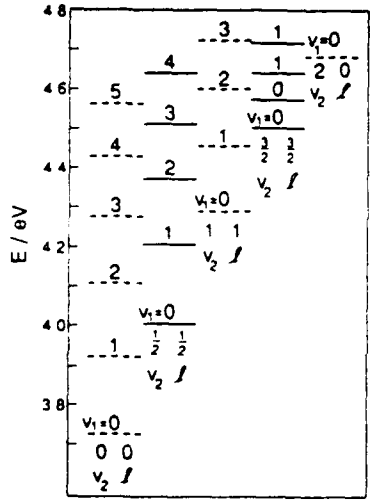

Fig. 2. Rovibronic energy levels associated to the first electronically excited state of H_3. The full lines are the levels including the effect of the geometric phase while the dashed ones exclude that effect. The quantum numbers v_1, v_2 and l are defined in the text. The origin for the energy scale is the bottom of the isolated ground electronic H_2 potential energy curve. These levels are for the $J=0$ states, but the $J=1$ levels are nearly degenerate with them, the splitting being of the order of 10^{-2} eV. Their nuclear permutation symmetries depend on J and on the parity Π, as well as whether the geometric phase is or is not included (see tables 3 and 5). There are two levels for each of the sets of quantum numbers ($v_1=0$, $v_2=l=\frac{1}{2}$) and ($v_1=1$, $v_2=l=\frac{1}{2}$), which would be degenerate if the potential were exactly cylindrically symmetric around the Y_1 axis (see text and fig. 1).

Table 5
Hyperspherical method energy levels including the effect of the geometric phase [a,b]

$v_1 v_2 l$ [c]	$J=0$	$J=1$ even parity	$J=1$ odd parity
$0\,\frac{1}{2}\,\frac{1}{2}$	4.0215 (E)	4.0286 (E)	4.0256 (A_1) [d]
			4.0243 (A_2)
			4.0284 (E)
$1\,\frac{1}{2}\,\frac{1}{2}$	4.2049 (E)	4.2114 (E)	4.2087 (A_1) [d]
			4.2076 (A_2)
			4.2113 (E)
$2\,\frac{1}{2}\,\frac{1}{2}$	4.3710 (E)	4.3769 (E)	4.3744 (A_1) [d]
			4.3734 (A_2)
			4.3768 (E)
$3\,\frac{1}{2}\,\frac{1}{2}$	4.5189 (E)	4.5243 (E)	4.5220 (A_1) [d]
			4.5210 (A_2)
			4.5241 (E)
$4\,\frac{1}{2}\,\frac{1}{2}$	4.6468 (E)	4.6517 (E)	4.6496 (A_1) [d]
			4.6487 (A_2)
			4.6515 (E)
$0\,\frac{3}{2}\,\frac{3}{2}$	4.5005 (A_1) [d]	4.5071 (A_2)	4.5050 (E)
	4.5700 (A_2)	4.5768 (A_1) [d]	4.5733 (E)
$1\,\frac{3}{2}\,\frac{3}{2}$	4.6425 (A_1) [d]	4.6484 (A_2)	4.6466 (E)
	4.7177 (A_2)	4.7237 (A_1) [d]	4.7223 (E)

[a] The energy is in eV and its origin corresponds to the bottom of the ground electronic state of the isolated H_2 molecule.
[b] The irreducible representations are the ones for the permutation group of the nuclei to which $\Psi^{JM\Pi\Gamma}$ belongs.
[c] Quantum numbers used to classify the states (see text).
[d] Levels with A_1 symmetry are included for completeness, but are forbidden by the Pauli principle.

permit inclusion of the geometric phase due to the conical intersection whereas the hyperspherical method does.

Fig. 2 and table 5 show the important modifications of the bound rovibrational energies when the geometric phase is included in the hyperspherical calculation. These changes can be understood if one defines quantum numbers to the bound states of tables 3 and 5 by modeling the nuclear wavefunction in the following way [81]:

– We retain a single term in the expansion of the bound states in the LHSF basis (eq. (3a)). This Born–Oppenheimer-type approximation, also used to model reactive scattering resonances [24], is very accurate in the present case where the frequency associated to the hyperspherical mode is smaller than those of the fixed-ρ bending modes: the resulting bound state energies are shifted by less than 0.4 meV. This approximation suggests that we define the quantum number v_1 associated with the hyperradial motion as the number of nodes of the hyperradial function $F_n^{J\Pi\Gamma}(\rho)$ (eq. (3a)). This mode corresponds to the breathing normal mode in the limit of small amplitude vibrations, but in the present case, it can have large amplitudes with an excitation as large as $v_1 = 5$ (table 3).

– We assume that the fixed-ρ bending vibration has small amplitude, so that the wavefunction is concentrated near $\theta = 0$. This approximation is reasonable due to the steep increase of the potential as a function of θ. It suggests that we neglect the asymmetric top coupling elements in the kinetic energy (last term of eq. (5)) and the φ_i dependence in the potential. The (non-symmetrized) LHSF can then be factored as

$$\Phi_n^{JM\Pi} = \exp(i n_\bullet \varphi_i)\, g_{v_2 l}(\theta;\rho)\, D^J_{MK}(\alpha,\beta,\gamma)\,, \tag{9a}$$

where $g_{v_2 l}$ is defined by

[81] The actual energy values given in tables 3 and 5 are calculated accurately; this model is used only to assign quantum numbers to these levels.

$$\left[-\frac{2\hbar^2}{\mu\rho^2}\left(\frac{1}{\theta}\frac{\partial}{\partial\theta}\theta\frac{\partial}{\partial\theta}-\frac{l^2}{\theta^2}\right)+V(\rho,\theta)\right]g_{v_2 l}(\theta;\rho)=\left[\epsilon_{v_2 l}^{JK}(\rho)-\left(\frac{J(J+1)-\frac{1}{2}K^2}{\mu\rho^2}\pm\frac{lK}{\mu\rho^2}\right)\hbar^2\right]g_{v_2 l}(\theta;\rho)\,. \qquad (9b)$$

Eq. (9b) is the small-θ limit of eq. (3b) (see also eq. (5)). l quantizes the absolute value of the vibrational angular momentum in a new body frame, which is an Eckart frame associated to the equilibrium position of the nuclei in the equilateral triangular configuration [41], and is given by $l=|n_\varphi-\frac{1}{2}K|$. v_2 is the bending vibrational quantum number and is defined by analogy with the two-dimensional harmonic oscillator such that the number of θ nodes of $g_{v_2 l}$ is $\frac{1}{2}(v_2-l)$ [42]. v_2 and l are both integers when the geometric phase is not considered and become both half odd integers when it is taken into account. If the potential were a harmonic function of θ, the bound state energies would increase linearly with v_2 for each v_1 value. Although the potential is an approximate linear function of θ, tables 3 and 5 indicate that the dependence of the bound state energies on v_2 is not far from linear. Therefore, as shown in fig. 2, each of the levels with the geometric phase (v_2 half odd integer) is almost half way in energy between two consecutive ones without this phase (v_2 integer).

The quantum numbers v_2 and l defined above are closely related to the ones (n and j) defined in ref. [31] for the analysis of the geometric phase in the $2\,^2E'$ Na_3 excited state. However, due to important differences in the shapes of the electronic potentials (minimum for equilateral triangular configurations in the present excited H_3 state, but for distorted configurations [9] in the Na_3 potential used in ref. [31]), the dependence of the bound state energies on these quantum numbers is different in the two systems.

Due to the Pauli principle and to the symmetries of the nuclear spin wavefunction with respect to interchange of the identical nuclei, the only allowed electronuclear wavefunctions $\Psi^{JM\pi\Gamma}$ (eq. (1)) have A_2 or E nuclear permutation symmetries, and they correspond to quartet and doublet nuclear spins respectively. The number of such levels which satisfy the Pauli principle and their spin symmetries change significantly when the effect of the geometric phase is included.

4. Conclusions

We have described a new hyperspherical propagation method for the calculation of bound rovibrational states. This method is well adapted to systems of three identical particles, because it allows easy inclusion of the full permutation symmetries of the system and of the effect of conical intersections on the phase of the nuclear wavefunction.

We have shown that, in the case of the bound rovibrational states in the first electronically excited state of H_3, the geometric phase results in bending modes having half odd integer quantum numbers and in important changes of the rovibrational state energies and of their symmetry properties. In the following paper [43], we study the influence of the geometric phase on the chemical reaction which occurs in the ground electronic state of H_3.

Acknowledgement

This work has been supported in part by Air Force Astronautics Laboratory contract F04611-86-K-0067 and by DOE grant DE-AS03-83ER. Most of the calculations were performed on the CRAY-XMP/48 and SCS-40 computers at the NSF San Diego Supercomputing Center. BL thanks the "Centre National de la Recherche Scientifique" for financial support and J.M. Launay for useful discussions on the hyperspherical method.

References

[1] G. Herzberg, J. Chem. Phys. 70 (1979) 4806;
I. Dabrowski and G. Herzberg, Can. J. Phys. 58 (1980) 1238;

G. Herzberg and J.K.G. Watson, Can. J. Phys. 58 (1980) 1250;
G. Herzberg, H. Lew, J.J. Sloan and J.K.G. Watson, Can. J. Phys. 59 (1981) 428;
G. Herzberg, J.J. Sloan and J.K.G. Watson, Can. J. Phys. 60 (1982) 1261.
[2] H. Helm, Phys. Rev. Letters 56 (1986) 42.
[3] J. Garvey and A. Kuppermann, Chem. Phys. Letters 107 (1984) 491.
[4] H. King and K. Morokuma, J. Chem. Phys. 71 (1979) 3213.
[5] M. Jungen, J. Chem. Phys. 71 (1979) 3540.
[6] R. Martin, J. Chem. Phys. 71 (1979) 3541.
[7] I.D. Petsalakis, G. Theodorakopoulos and J.S. Wright, J. Chem. Phys. 89 (1988) 6850.
[8] A.J.C. Varandas, F.B. Brown, C.A. Mead, D.G. Truhlar and N.C. Blais, J. Chem. Phys. 86 (1987) 6258.
[9] H.A. Jahn and E. Teller, Proc. Roy. Soc. A 161 (1937) 220.
[10] G.C. Schatz and A. Kuppermann, J. Chem. Phys. 65 (1976) 4668;
R.T. Ling and A. Kuppermann, in: Electronic and Atomic Collisions, Abstract of the 9th International Conference on the Physics of Electronic and Atomic Collisions, Seattle, Washington, 24–30 July 1975, Vol. 1, eds. J.S. Risley and R. Geballe (Univ. Washington Press, Seattle, 1975) pp. 353, 354;
A. Kuppermann and P.G. Hipes, J. Chem. Phys. 84 (1986) 5962;
P.G. Hipes and A. Kuppermann, Chem. Phys. Letters 133 (1987) 1;
S.A. Cuccaro, P.G. Hipes and A. Kuppermann, Chem. Phys. Letters 154 (1989) 155; 157 (1989) 440.
[11] R.T Pack and G.A. Parker, J. Chem. Phys. 87 (1987) 3888.
[12] J. Linderberg, S. Padkjær, Y. Öhrn and B. Vessal, J. Chem. Phys. 90 (1989) 6254.
[13] J.M. Launay and M. Le Dourneuf, Chem. Phys. Letters 163 (1989) 178.
[14] J.Z.H. Zhang and W.H. Miller, Chem. Phys. Letters 153 (1988) 465; 159 (1989) 130.
[15] A.B. Elkowitz and R.E. Wyatt, J. Chem. Phys. 62 (1975) 2504; 63 (1975) 702;
D.E. Manopoulos and R.E. Wyatt, Chem. Phys. Letters 159 (1989) 123.
[16] R.B. Walker, E.B. Stechel and J.C. Light, J. Chem. Phys. 69 (1978) 2922;
F. Webster and J.C. Light, J. Chem. Phys. 90 (1989) 300.
[17] M. Mladenovic, M. Zhao, D.G. Truhlar, D.W. Schwenke, Y. Sun and D.J. Kouri, J. Phys. Chem. 92 (1988) 7035; Chem. Phys. Letters 146 (1988) 358.
[18] M. Vogler, Phys. Rev. A 19 (1979) 1.
[19] J.K.G. Watson, Phys. Rev. A 22 (1980) 2279.
[20] J. Tennyson, Computer Phys. Commun. 42 (1986) 257.
[21] J. Tennyson, Computer Phys. Rept. 4 (1986) 1.
[22] R.C. Whitten and F.T. Smith, J. Math. Phys. 9 (1968) 1103.
[23] B.R. Johnson, J. Chem. Phys. 73 (1980) 5051; 79 (1983) 1906, 1916.
[24] J.M. Launay and B. Lepetit, Chem. Phys. Letters 144 (1988) 346;
B. Lepetit and J.M. Launay, Chem. Phys. Letters 151 (1988) 287.
[25] R. Wallace, Chem. Phys. 37 (1979) 93.
[26] J.G. Frey, Chem. Phys. Letters 102 (1983) 421;
J.G. Frey and B.J. Howard, Chem. Phys. 99 (1985) 415.
[27] H.C. Longuet-Higgins, U. Öpik, M.H.L. Pryce and R.A. Sack, Proc. Roy. Soc. A 244 (1958) 1;
G. Herzberg and H.C. Longuet-Higgins, Discussions Faraday Soc. 35 (1963) 77;
H.C. Longuet-Higgins, Advan. Spectry. 2 (1961) 429.
[28] C.A. Mead and D.G. Truhlar, J. Chem. Phys. 70 (1979) 2284.
[29] C.A. Mead, Chem. Phys. 49 (1980) 23.
[30] M.V. Berry, Proc. Roy. Soc. A 392 (1984) 45.
[31] G. Delacrétaz, E.R. Grant, R.L. Whetten, L. Wöste and J.W. Zwanziger, Phys. Rev. Letters 56 (1986) 2598.
[32] Y. Aharonov and D. Bohm, Phys. Rev. 115 (1959) 485.
[33] L.M. Delves, Nucl. Phys. 9 (1959) 391; 20 (1960) 275.
[34] B. Lepetit, J.M. Launay and M. Le Dourneuf, Chem. Phys. 106 (1986) 103.
[35] A.S. Davydov, Quantum mechanics, 2nd Ed. (Pergamon Press, Oxford, 1976) pp. 151–161.
[36] W. Zickendraht, Ann. Phys. 35 (1965) 18.
[37] H. Mayer, J. Phys. A 8 (1975) 1562.
[38] L. Wolniewicz, J. Chem. Phys. 90 (1989) 371.
[39] A. Kuppermann, Chem. Phys. Letters 32 (1975) 374.
[40] J. Tennyson and B.T. Sutcliffe, Mol. Phys. 51 (1984) 887.
[41] E.B. Wilson, J.C. Decius and P.C. Cross, Molecular vibrations (Dover, New York, 1980) ch. 11.
[42] S. Flügge, Practical quantum mechanics (Springer, Berlin, 1974) problem 42.
[43] B. Lepetit and A. Kuppermann, Chem. Phys. Letters 166 (1990) 581.

NUMERICAL STUDY OF THE GEOMETRIC PHASE IN THE H+H_2 REACTION

B. LEPETIT [1] and A. KUPPERMANN

Arthur Amos Noyes Laboratory of Chemical Physics, Division of Chemistry and Chemical Engineering [2], California Institute of Technology, Pasadena, CA 91125, USA

Received 25 October 1989; in final form 4 December 1989

The effect on the H + H_2 reaction of the geometric phase induced by the conical intersection between the two lowest electronic states of H_3 is investigated by an accurate quantum mechanical computation up to 2.6 eV above the bottom of the ground state H_2 electronic potential well for the total angular momentum $J=0$. The main effects of the inclusion of the geometric phase are a sign change in the reactive scattering matrix and modifications in the nuclear permutation symmetries of the calculated resonances. Cross-sections to which non-reactive processes contribute (ortho→ortho and para→para) are significantly modified, whereas the others (ortho→para and para→ortho) are not.

1. Introduction

Most of the quantum theoretical studies on the $H(^2S)+H_2(^1\Sigma_g^+)$ reaction have used the Born–Oppenheimer approximation (see for instance refs. [1–12]), and assumed that the reaction occurs on the single ground electronic potential energy surface. This approximation is expected to be quite accurate below about 2.6 eV of total energy (with respect to the bottom of the $H_2(^1\Sigma_g^+)$ potential well) since this is 0.1 eV below the energy of the minimum of the first excited potential.

However, a complication neglected in all the previous numerical studies [1–12] arises from the fact that the ground electronic state conically intersects the first excited one for equilateral triangular configurations of the nuclei. There is a sign change of the electronic wavefunction as one follows a closed path in nuclear configuration space around the line of the conical intersection. Since the total electronuclear wavefunction is continuous and single-valued, there has to be a compensating sign change in the nuclear part of the wavefunction [13–16]. This sign change is a particular case of Berry's geometric phase [17] and is sometimes referred to as the molecular Aharonov–Bohm effect [14–16,18]. We use the expression "geometric phase" in the rest of this paper. In the preceding paper [19], referred to hereafter as I, we have shown that this geometric phase completely modifies the energy spectrum and the permutation symmetry properties of the quasi-bound rovibrational states of the first electronically excited state. In this Letter, we study the effect of this geometric phase on the chemical reaction which occurs on the ground electronic potential energy surface.

It has been shown formally that, if the condition that the wavefunction is zero in a certain region of nuclear configuration space separating different arrangement channels (see section 3) is fulfilled, the only effect of the geometric phase is to produce an interference between reactive and non-reactive scattering amplitudes which is exactly the opposite to what it would be without consideration of the conical intersection [16]. This condition is likely to be satisfied for the low collision energies considered in the earlier quantum studies of this reaction [1–3], but a numerical study including the geometric phase exactly is required to find out if this condition remains valid at the higher energies reached using more recent methods [4–12].

To include the geometric phase in the calculation of the scattering states of the system, two distinct ap-

[1] Permanent address: UPR 261 du CNRS, Observatoire de Paris, 92195 Meudon, France.

[2] Contribution No. 8053.

0009-2614/90/$ 03.50

proaches can be followed, both leading to the same final result:

- One can use real electronic and nuclear wavefunctions with compensating sign changes and include the geometric phase simply by enforcing appropriate boundary conditions and permutation symmetries on the nuclear wavefunction.

- Alternatively, one can add extra complex phase factors to the electronic and nuclear parts of the wavefunction to enforce the continuity and single-valuedness of each of them. These extra phases add to the nuclear Schrödinger equation a term formally similar to a vector potential associated to a delta-function magnetic field located on the conical intersection line [14,15]. Similarly to the Aharonov–Bohm effect [18], this magnetic field modifies the interference pattern between semi-classical trajectories passing on opposite sides of the conical intersection line [14].

In this paper, we use the first of these two approaches to compute the quantum-mechanical three-dimensional reactive scattering matrix for the total angular momentum $J=0$ and for total energies below 2.6 eV. We restrict the use of the second approach to the semi-classical interpretation of the results. Section 2 describes briefly how the proper boundary conditions and symmetry properties of the nuclear wavefunction can be easily incorporated in a hyperspherical formalism which uses modified [20] Whitten–Smith coordinates [21] to describe the strong interaction of the three atoms and symmetrized hyperspherical coordinates [4,22] derived from Delves' coordinates [23] to describe the initial and final $H+H_2$ arrangements. In section 3, we describe in detail the effect of the geometric phase on the scattering matrix and cross-sections for distinguishable and undistinguishable nuclei.

2. Method

We outline here the main features of the hyperspherical method, already described in I. As in that paper, we neglect spin–orbit and spin–spin interactions throughout. In the Bohr–Oppenheimer approximation, the total wavefunction is a product of electronic and nuclear parts. The latter is a product of nuclear spin and nuclear spacial wavefunctions. The *electronuclear* wavefunction $\Psi^{JM\Pi\Gamma}$ excluding the nuclear spin part (see eq. (1) in I) is chosen to belong to an irreducible representation Γ of the nuclear permutation group (P_3) of H_3. It is also labelled by the total nuclear angular momentum quantum number J, its component M along a laboratory-fixed axis and the nuclear parity Π. In the absence of the geometric phase, we make the usual assumption that the electronic wavefunction belongs to the A_1 irreducible representation of the nuclear permutation group (P_3). In this case, the spacial part $\psi^{JM\Pi\Gamma}$ of the nuclear wavefunction belongs to the same irreducible representation Γ as $\Psi^{JM\Pi\Gamma}$. In the presence of the geometric phase, although $\Psi^{JM\Pi\Gamma}$ still belongs to the irreducible representation Γ of P_3, the spacial part of the nuclear wavefunction and the electronic wavefunction do not.

Let A_α, A_β, A_γ be the atoms of the system, and (λ, ν, κ) be any cyclic permutation of (α, β, γ). r_λ is the mass-scaled [23] internuclear vector for the diatom $A_\nu A_\kappa$ and R_λ the mass-scaled vector of A_λ with respect to the center of mass of $A_\nu A_\kappa$. In the hyperspherical method, the Hamiltonian is written in terms of the hyperradius $\rho=(R_\lambda^2+r_\lambda^2)^{1/2}$ which parametrizes the global size of the triatomic system and of a set of five angles ζ which describe its shape and orientation in space [4,5,10–12,19–24]:

$$H=-\frac{\hbar^2}{2\mu}\rho^{-5}\frac{\partial}{\partial\rho}\rho^5\frac{\partial}{\partial\rho}+\frac{\hat{\Lambda}^2}{2\mu\rho^2}+V(\rho,\zeta)\,. \qquad (1)$$

In this expression, μ is the three-body reduced mass, $\hat{\Lambda}$ the grand-canonical angular momentum and V the Born–Oppenheimer electronic potential. The spacial nuclear scattering wavefunction $\psi^{JM\Pi\Gamma}$ is an eigenfunction of the nuclear Hamiltonian (eq. (1)) and is expanded in a basis of local hyperspherical surface functions (LHSF), $\Phi_n^{JM\Pi\Gamma}$:

$$\psi^{JM\Pi\Gamma}(\rho,\zeta)=\frac{1}{\rho^{5/2}}\sum_n F_n^{J\Pi\Gamma}(\rho)\,\Phi_n^{JM\Pi\Gamma}(\zeta;\rho)\,, \qquad (2)$$

which are eigenfunctions of the fixed-hyperradius Hamiltonian:

$$\left(\frac{\hat{\Lambda}^2}{2\mu\rho^2}+V(\rho,\zeta)\right)\Phi_n^{JM\Pi\Gamma}(\zeta;\rho)$$

$$=\epsilon_n^{J\Pi\Gamma}(\rho)\,\Phi_n^{JM\Pi\Gamma}(\zeta;\rho)\,. \qquad (3)$$

The coefficients $F_n^{J\Pi\Gamma}$ in eq. (2) are solutions of a

set of ordinary coupled differential equations in ρ, which we solve using piece-wise diabatic bases [4,25].

A solution of eq. (3) efficient for all values of the hyperradius requires a division of the internal configuration space into two regions:

– Region I corresponds to small values of the hyperradius for which the three atoms interact strongly. We use the modified [20] Whitten–Smith [21] definition of the five angular coordinates in this region: three Euler angles define the orientation of the frame of the principal axes of inertia in space, and the angles $(\theta, \varphi_\lambda)$ specify the shape of the molecular triangle. The LHSF are computed numerically by expansion in a product basis of simple trigonometric functions in θ and φ_λ (see eqs. (6) and (7) in I). Table 1 indicates how to choose the functions of φ_λ to obtain electronuclear wavefunctions $\Psi^{JM\Pi\Gamma}$ with correct permutation symmetries, with and without consideration of the geometric phase.

– Region II corresponds to large values of the hyperradius for which the system has separated into an atom and a diatom. The nuclear wavefunction is now localized in the electronic potential valleys associated to each of the corresponding asymptotic arrangements and its amplitude on the plateaux separating the arrangement channels is negligible. This localization makes the expansion of the LHSF on the delocalized product basis used in region I inefficient and suggests the use of symmetrized hyperspherical coordinates [4,22] instead. Therefore, $(\theta, \varphi_\lambda)$ are replaced in region II by $(\omega_\lambda, \gamma_\lambda)$ defined by $\omega_\lambda = 2\arctan(r_\lambda/R_\lambda)$ and $\gamma_\lambda = \arccos(R_\lambda \cdot r_\lambda / R_\lambda r_\lambda)$, each in the range 0 to π. The LHSF are now expanded in a product basis [4] of Legendre polynomials in $\cos\gamma_\lambda$ and vibrational-type functions in ω_λ. Since product bases associated to different arrangements do not overlap in region II, the LHSF which include the geometric phase differ from the ones which exclude it only by simple changes in the signs of the pieces of the wavefunction within each arrangement channel. The geometric phase can be included straightforwardly in region II since it does not change the overlap and interaction matrices.

The LSTH Born–Oppenheimer electronic potential energy surface has been used [26]. This surface was chosen, rather than the DMBE [27] one used for the bound state calculations of paper I, because we already had accurate scattering results [4] for it which served to test the validity of the new hyperspherical method described here. Recent results [7,9] indicate that the use of the DMBE potential does not significantly change the final scattering matrix results. The boundary between region I and region II was set at $\rho = 6$ bohr. Surface functions were computed at 20 values of ρ between 2 and 6 bohr in region I and 31 values of ρ between 6 and 12 bohr in region II. The results shown below have been obtained with 1156 product functions (34 for each of the two angular coordinates θ and φ_λ) in region I and 156 product functions in region II. We verified that the convergence of the scattering matrix elements with respect to the size of the product basis was of the order of 1% by comparing with a smaller calculation involving 900 product functions in region I. 65 LHSF for A_1 and A_2 permutation symmetries and 130 LHSF for E symmetries, with energies accurate to within approximation 10^{-3} eV, have been used in the expansion of the wavefunction. The unitarity of the resulting scattering matrix was always

Table 1
Basis in φ_λ for expansion of the $J=0$ LHSF

	A_1 [a]	A_2 [a]	E [a]
without phase [b]	$\cos(3n\varphi_\lambda)$	$\sin(3n\varphi_\lambda)$	$\cos[(3n\pm1)\varphi_\lambda]$
with phase [c]	$\cos[(3n+\frac{3}{2})\varphi_\lambda]$	$\sin[(3n+\frac{3}{2})\varphi_\lambda]$	$\cos[(3n\pm\frac{1}{2})\varphi_\lambda]$

[a] Irreducible representation of the permutation group of the nuclei to which the electronuclear wavefunction $\Psi^{JM\Pi\Gamma}$ belongs. We choose the component of the E irreducible representation which is symmetric with respect to the $A_\rho \leftrightarrow A_\alpha$ permutation (see text). n is a non-negative integer.

[b] Excluding consideration of the geometric phase. In this case, the electronic wavefunction is assumed to belong to the A_1 irreducible representation of P_3.

[c] Including consideration of the geometric phase.

better than 1%, except for the E symmetry above 2.4 eV for a few columns and rows associated to highly excited reactants or products.

3. Results

We first discuss the effect of the geometric phase on the scattering matrices associated to electronuclear wavefunctions $\Psi^{J,M\Pi\Gamma}$ which are bases for irreducible representations of the permutation group of the nuclei. Then, we switch to the scattering matrices associated to distinguishable particles. This representation affords a simple understanding of the effect of the geometric phase on the $H+H_2$ reaction.

Figs. 1 and 2 show some transition probabilities for the total angular momentum $J=0$ and for electronuclear wavefunctions $\Psi^{J,M\Pi\Gamma}$ belonging to irreducible representations of P_3. Comparison of both rows of figs. 1 and 2 shows that the inclusion of the geometric phase induces important changes in the qualitative features of the transition probabilities associated to irreducible representations of the permutation group, except for the transitions from para to ortho (and ortho to para because of the microscopic reversibility) hydrogen in the E irreducible representation which remain almost unchanged (last column of fig. 2).

One interesting modification due to the inclusion of the geometric phase is the exchange of qualitative features between the transition probabilities associated to the A_1 and A_2 irreducible representations (fig. 1). In particular, the resonances, which correspond to A_1 wavefunctions without geometric phase, appear on the A_2 probabilities when this phase is included. This exchange results from a similar one in the nodal structure of the nuclear wavefunctions. Indeed, the last of ref. [4] shows that resonance wavefunctions are non-zero for near linear configurations of H_3 where two internuclear distances are equal. These configurations correspond to the half planes $\varphi_i=\pi/3,\ \pi,\ 5\pi/3$, which, according to table 1, are nodal planes for the A_2 wavefunctions in the absence of the geometric phase and for the A_1 wavefunctions when this phase is included. Therefore, the resonances must correspond to A_1 electronuclear wavefunctions $\Psi^{J,M\Pi\Gamma}$ without the geometric phase and to A_2 wavefunctions with this phase for $J=0$.

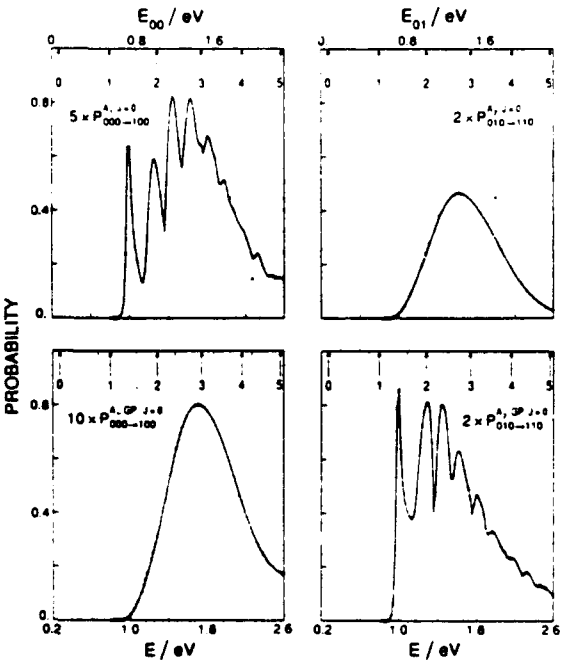

Fig. 1. Transition probabilities as a function of energy for $J=0$ without (upper row) and with (lower row) consideration of the geometric phase. The left column corresponds to an electronuclear wavefunction $\Psi^{J,M\Pi\Gamma}$ which belongs to the A_1 irreducible representation of the permutation group of the nuclei and to the transition $H+H_2(v=0, j=0, m_j=0)\rightarrow H+H_2(v'=1, j'=0, m_{j'}=0)$. The right column corresponds to an electronuclear wavefunction $\Psi^{J,M\Pi\Gamma}$ which belongs to the A_2 irreducible representation of the permutation group of the nuclei and to the transition $H+H_2(v=0, j=1, m_j=0)\rightarrow H+H_2(v'=1, j'=1, m_{j'}=0)$. The lower abscissa is the total energy and the upper abscissa the reagent relative translational energy. The vertical arrows on the upper abscissa denote the energies of the $H_2(v, j=0)$ states and are labelled by the values of v. The squares on the probability curves indicate the points for which the scattering calculations were made.

More generally, the inclusion of the geometric phase modifies the result of the symmetry analysis of resonances for low total angular momentum described in the last of ref. [4]. This paper shows that the exchange of the two extreme hydrogen atoms of the near linear configurations considered in the previous paragraph multiplies the spacial part of the *nuclear* wavefunction by a factor $(-1)^{\Pi+K}$, where K is the vibrational angular momentum of the resonant state and Π its parity. If X_Γ is the eigenvalue of the operator which permutes the two extreme hydrogen

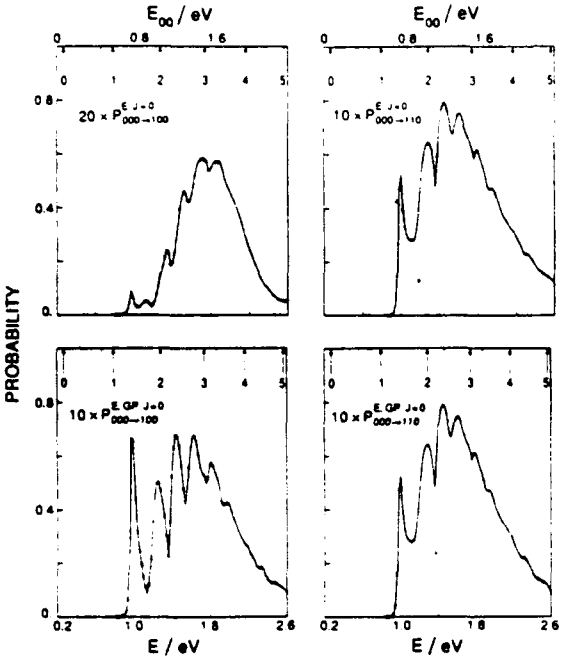

Fig. 2. Transition probabilities as a function of energy for $J=0$ without (upper row) and with (lower row) consideration of the geometric phase, for the transitions $H+H_2(v=0, j=0, m_j=0) \rightarrow H+H_2(v'=1, j'=0, m_{j'}=0)$ (left column) and $H+H_2(v=0, j=0, m_j=0) \rightarrow H+H_2(v'=1, j'=1, m_{j'}=0)$ (right column) with the electronuclear wavefunction $\Psi^{JM\Pi\Gamma}$ belonging to the E irreducible representation of P_3. For the other details, see the caption of fig. 1.

atoms in the *electronuclear* wavefunction $\Psi^{JM\Pi\Gamma}$ ($+1$ for the A_1 irreducible representation, -1 for A_2 and ± 1 for the E doubly degenerate irreducible representation, according to which component is considered), the condition for having a resonance without consideration of the geometric phase is $X_\Gamma = (-1)^{\Pi+K}$, since, in this case, we assume that the *electronic* part of the wavefunction is symmetric for the permutation of the hydrogen nuclei. If now the geometric phase is included, the condition for having a resonance becomes $X_\Gamma = (-1)^{\Pi+K+1}$ since the *electronic* wavefunction is now antisymmetric with respect to the nuclear permutation. Therefore, the symmetry assignments of the resonances are exchanged for the A_1 and A_2 irreducible representations, but remain unchanged for the E irreducible representation, which has doubly degenerate symmetric and antisymmetric components.

We now assume that the three hydrogen atoms are distinguishable particles. Fig. 3 shows that the non-reactive (direct) and reactive (exchange) transition probabilities are almost not affected by the inclusion of the geometric phase. Only slight changes (less than 10%) appear in the probabilities above 2 eV for low excited states of the reactants and products (these changes however can become larger than 10% for small transitions between rotationally excited reactant and product states). The strong effect observed in fig. 1 in the transition probabilities associated to the irreducible representations of the permutation group of the nuclei results mainly in *a change of π in the phase of the reactive scattering matrix elements*, whereas the phases of the non-reactive matrix elements and the norms of the reactive and non-reactive scattering matrix elements are only slightly modified by the geometric phase. These numerical results validate the conclusion of ref. [16] and the assumption on which it rests over a wide energy range. Indeed, ref. [16] shows formally that, if the wavefunction is zero in the vicinity of the half plane $\varphi_\lambda = \pi$, then the only effect of the geometric phase is to change the sign of the reactive scattering matrix. This result should be also valid for non-zero total angular momenta.

Ref. [14] suggests a semiclassical picture for the effect of the geometric phase on the reactive probabilities, in terms of the modification of the interference pattern between trajectories passing on opposite sides of the conical intersection axis ($\theta=0$). However, the quantum results suggest that, since only the phases of the reactive scattering matrix elements are significantly changed, almost all trajectories should pass on the same side of the conical intersection, namely the one nearest the minimum energy path. We performed quasi-classical trajectory calculations for $J=0$ with a sample of 400 trajectories for each collision energy. Below 2.6 eV, we found indeed that for the ground rovibrational initial state ($v=j=0$) only one trajectory (at 2.4 eV) passes on the side of the conical intersection opposite to the minimum energy path. However, rotational excitation of the reactants can increase this number: 10% of the reactive trajectories pass on the side opposite to the minimum energy path at 2.5 eV for $j=10$ and 15. This suggests that, as observed in the quantum results, the effect of the geometric phase can become

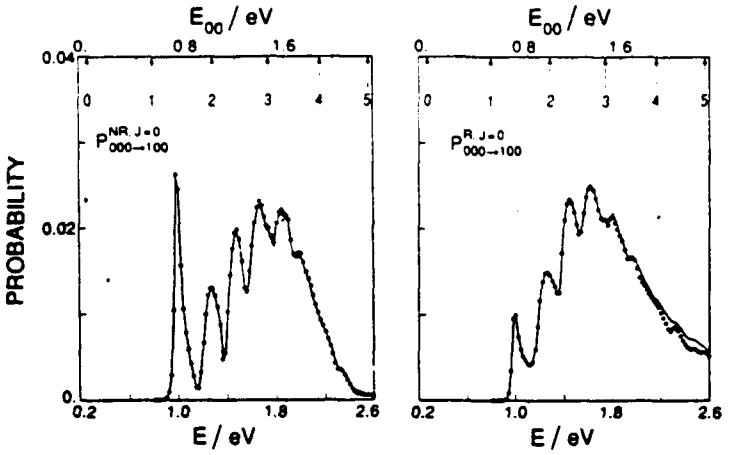

Fig. 3. Non-reactive (left) and reactive (right) transition probabilities for $H+H_2(v=0, j=0, m_j=0) \rightarrow H+H_2(v'=1, j'=0, m_j=0)$. The dots and the continuous lines refer to the calculations excluding and including the geometric phase respectively. For the other details, see the caption of fig. 1.

more important for some transitions between rotationally excited reactants and products. Finally, the number of trajectories passing on the side of the conical intersection opposite to the minimum energy path increases strongly above 2.8 eV and reaches 40% of the total number of reactive trajectories for $j=0$ at 4 eV. This indicates that the geometric phase modifies both the norms and the phases of the scattering matrix elements in this high energy range. However, inclusion of the electronic coupling to the first electronically excited state becomes necessary to obtain quantitatively correct results in this energy range.

Consideration of the Pauli-antisymmetrized (defined in the second ref. [1]) $J=0$ partial cross-sections allows us to estimate qualitatively how the Pauli-antisymmetrized integral cross-sections are modified by inclusion of the geometric phase. The previous discussion indicates that the para to ortho or ortho to para antisymmetrized cross-sections are almost not modified for energies below 2.6 eV by inclusion of the geometric phase, since only the reactive scattering amplitude appears in the expressions of the antisymmetrized cross-sections for these transitions (see eqs. (5.39) and (5.40) in the second ref. [1]). Therefore, this phase cannot be the reason for the important discrepancies between experimental and theoretical integral cross-sections below 1.4 eV for para to ortho transitions: the strong resonant patterns which are present on the experimental integral cross-sections [28] will not appear on the corresponding theoretical results [6,7,12] even if the geometric phase is included. However, fig. 4 suggests that antisymmetrized cross-sections can be significantly modified by the introduction of the geometric phase for para to para or ortho to ortho transitions, since the way reactive and non-reactive scattering amplitudes interfere is, with a good accuracy below 2.6 eV, changed to its opposite (see eqs. (5.39) and (5.40) in the second ref. [1]). This change is not very important at low energy when the reaction probabilities are small compared to the non-reactive ones (see the 000→020 transition probability below 0.6 eV in fig. 4), but it can modify even the qualitative features and the order of magnitude of the antisymmetrized cross-sections when, at higher energy, reactive and non-reactive scattering amplitudes become of the same order of magnitude.

The effect of the geometric phase on the details of the angular distributions of the ortho→ortho and para→para cross-sections should be even more pronounced than on the corresponding integral cross-sections. The differential cross-sections for these transitions show an oscillatory dependence on scattering angle [1] which should become more intense as energy increases. These oscillations are due to in-

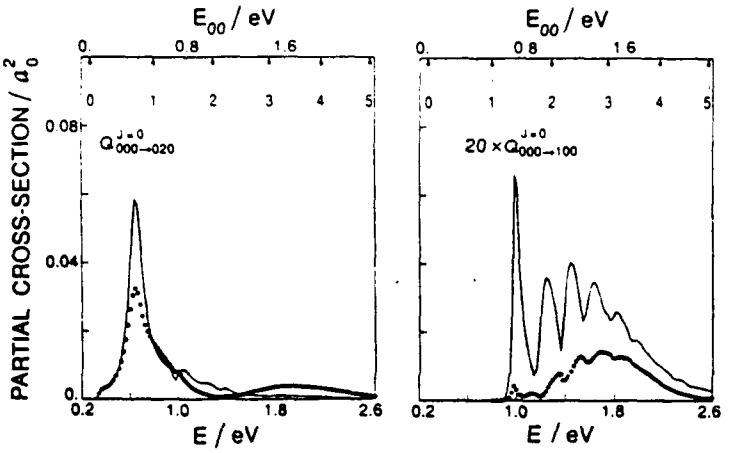

Fig. 4. Antisymmetrized $J=0$ partial integral cross-sections for the transition $H+H_2(v=0, j=0, m_j=0) \rightarrow H+H_2(v'=0, j'=2, m_j=0)$ (left) and $H+H_2(v=0, j=0, m_j=0) \rightarrow H+H_2(v'=1, j'=0, m_j=0)$ (right). The dots and the continuous lines refer to the calculations excluding and including the geometric phase respectively. For the other details, see the caption of fig. 1.

terferences between direct and exchange scatterings, and a change in the sign of the exchange scattering amplitude should make constructive interferences destructive and vice versa [16].

4. Conclusions

The present numerical study of the geometric phase in the $H+H_2$ validates the conclusion of ref. [16] in a wide energy range below 2.6 eV: quite accurate cross-sections can be obtained by neglecting the geometric phase in the computations of the reactive and non-reactive scattering matrix elements and by including it a posteriori by changing the signs of the reactive scattering matrix elements. This sign change can modify significantly the spin-averaged cross-sections when the energy is high enough for reactive transition probabilities to be non-negligible compared to the non-reactive ones. Quasi-classical trajectory calculations indicate that this approximate treatment of the geometric phase becomes inaccurate at the higher energies for which the Born–Oppenheimer approximation is expected to break down. Finally, our quantum study also indicates that inclusion of the geometric phase changes the symmetry assignments of the resonances.

Acknowledgement

This work has been supported in part by Air Force Astronautics Laboratory Contract F04611-86-K-0067 and by DOE grant DE-AS03-83ER. The quantum calculations were performed both on the CRAY-XMP/48 and SCS-40 computers at the NSF San Diego Supercomputing Center and the CRAY-XMP/18 of the Jet Propulsion Laboratory. The quasi-classical trajectory calculations were performed on the 8 node Mark III hypercube of the California Institute of Technology. BL thanks the "Centre National de la Recherche Scientifique" for financial support and J.M. Launay for useful discussions on the hyperspherical method.

References

[1] A. Kuppermann and G.C. Schatz, J. Chem. Phys. 62 (1975) 2502;
G.C. Schatz and A. Kuppermann, J. Chem. Phys. 65 (1976) 4642.
[2] A.B. Elkowitz and R.E. Wyatt, J. Chem. Phys. 62 (1975) 2504; 63 (1975) 702.
[3] R.B. Walker, E.B. Stechel and J.C. Light, J. Chem. Phys. 69 (1978) 2922.
[4] R.T. Ling and A. Kuppermann, in: Electronic and Atomic Collisions, Abstract of the 9th International Conference on the Physics of Electronic and Atomic Collisions, Seattle.

Washington, 24–30 July 1975, Vol. 1, eds. J.S. Risley and R. Geballe (Univ. Washington Press, Seattle, 1975) pp. 353, 354;
A. Kuppermann and P.G. Hipes, J. Chem. Phys. 84 (1986) 5962;
P.G. Hipes and A. Kuppermann, Chem. Phys. Letters 133 (1987) 1;
S.A. Cuccaro, P.G. Hipes and A. Kuppermann, Chem. Phys. Letters 154 (1989) 155; 157 (1989) 440.
[5] G.C. Schatz, Chem. Phys. Letters 150 (1988) 92.
[6] J.Z.H. Zhang and W.H. Miller, Chem. Phys. Letters 153 (1988) 465; 159 (1989) 130.
[7] D.E. Manopoulos and R.E. Wyatt, Chem. Phys. Letters 159 (1989) 123.
[8] F. Webster and J.C. Light, J. Chem. Phys. 90 (1989) 300.
[9] M. Mladenovic, M. Zhao, D.G. Truhlar, D.W. Schwenke, Y. Sun and D.J. Kouri, Chem. Phys. Letters 146 (1988) 358; J. Phys. Chem. 92 (1988) 7035.
[10] J. Linderberg, S. Padkjær, Y. Öhrn and B. Vessal, J. Chem. Phys. 90 (1989) 6254.
[11] R.T Pack and G.A. Parker, J. Chem. Phys. 87 (1987) 3888.
[12] J.M. Launay and M. Le Dourneuf, Chem. Phys. Letters 163 (1989) 178.
[13] H.C. Longuet-Higgins, U. Öpik, M.H.L. Pryce and R.A. Sack, Proc. Roy. Soc. A 244 (1958) 1;
G. Herzberg and H.C. Longuet-Higgins, Discussions Faraday Soc. 35 (1963) 77;
H.C. Longuet-Higgins, Advan. Spectry. 2 (1961) 429.
[14] C.A. Mead and D.G. Truhlar, J. Chem. Phys. 70 (1979) 2284.
[15] C.A. Mead, Chem. Phys. 49 (1980) 23.
[16] C.A. Mead, J. Chem. Phys. 72 (1980) 3839.
[17] M.V. Berry, Proc. Roy. Soc. A 392 (1984) 45.
[18] Y. Aharonov and D. Bohm, Phys. Rev. 115 (1959) 485.
[19] B. Lepetit, Z. Peng and A. Kuppermann, Chem. Phys. Letters 166 (1990) 572.
[20] B.R. Johnson, J. Chem. Phys. 73 (1980) 5051; 79 (1983) 1906; 1916.
[21] R.C. Whitten and F.T. Smith, J. Math. Phys. 9 (1968) 1103.
[22] A. Kuppermann, Chem. Phys. Letters 32 (1975) 374.
[23] L.M. Delves, Nucl. Phys. 9 (1959) 391; 20 (1960) 275.
[24] J.M. Launay and B. Lepetit, Chem. Phys. Letters 144 (1988) 346;
B. Lepetit and J.M. Launay, Chem. Phys. Letters 151 (1988) 287.
[25] B. Lepetit, J.M. Launay and M. Le Dourneuf, Chem. Phys. 106 (1986) 103.
[26] P. Siegbahn and B. Liu, J. Chem. Phys. 68 (1978) 2457;
D.G. Truhlar and C.J. Horowitz, J. Chem. Phys. 68 (1978) 2466; 71 (1979) 1514.
[27] A.J.C. Varandas, F.B. Brown, C.A. Mead, D.G. Truhlar and N.C. Blais, J. Chem. Phys. 86 (1987) 6258.
[28] J.C. Nieh and J.J. Valentini, Phys. Rev. Letters 60 (1988) 519.

QUANTUM MECHANICAL REACTIVE SCATTERING USING A HIGH-PERFORMANCE DISTRIBUTED-MEMORY PARALLEL COMPUTER

Yi-Shuen Mark WU [1], Steven A. CUCCARO, Paul G. HIPES [2] and Aron KUPPERMANN
Arthur Amos Noyes Laboratory of Chemical Physics, Division of Chemistry and Chemical Engineering [3], California Institute of Technology, Pasadena, CA 91125, USA

Received 17 January 1990; in final form 21 February 1990

We have performed accurate three-dimensional quantum mechanical reactive scattering calculations for the $H+H_2$ system on the Caltech/JPL Mark *IIIfp* 64 processor hypercube, using the method of symmetrized hyperspherical coordinates and local hyperspherical surface functions. The results and timing obtained demonstrate that such distributed memory parallel architectures are competitive with the CRAY X-MP, CRAY 2 and CRAY Y-MP supercomputers and should allow the study of larger, more complicated chemical systems. In addition, we show that a selection rule for scattering resonances developed previously and tested for $J=0$, 1 resonances is also satisfied by the $J=2$ resonances obtained in the present calculations.

1. Introduction

There is considerable current interest in performing accurate quantum mechanical three-dimensional reactive scattering cross section calculations. Accurate solutions have until recently proved to be difficult and computationally expensive to obtain, in large part due to the lack of sufficiently powerful computers [1–7]. Prior to the advent of supercomputers, one could only solve the equations of motion for model systems or for sufficiently light atom–diatom systems at low energy [1–4]. As a result of the current development of efficient methodologies and increased access to supercomputers, there has been a remarkable surge of activity in this field [8–19]. The use of symmetrized hyperspherical coordinates [20] and of the local hyperspherical surface function formalism [8,9,21] has proven to be a successful approach to solve the three-dimensional Schrödinger equation [8,9,15,16]. However, even for modest reactive scattering calculations the memory and CPU demands are so great that CRAY-type supercomputers will soon be limiting progress.

Although there has been a steady improvement in the necessary technologies of the basic logic speeds of computers, there is little prospect of substantially faster single processor designs in the near future. Concurrent supercomputers are a natural next step in meeting the need for both increased memory and faster CPU. Individual processors, although slower than a single sequential supercomputer processor, can be connected together in sufficient number to make a powerful supercomputer. Such architectures offer the potential to obtain large increases in computing speed by simply increasing the number of processors. The actual speed-up depends on the nature of the algorithm, the characteristics of the processors, and the particular way these communicate with each other. The algorithms used and the codes developed on sequential machines should be replaced by codes optimized for parallel machines.

The essential property a calculation must have to be efficiently done on a highly parallel computer is that it be decomposable in such a way that in performing it almost all processors should be computing efficiently almost all of the time, and that the communication time between the processors should represent a small fraction of the computation time. In

[1] Work performed in partial fulfillment of the requirements for the Ph.D. degree in Chemistry at the California Institute of Technology.

[2] Current address: 2338 Redwood Road, Scotch Plains, NJ 07076, USA.

[3] Contribution number 8068.

0009-2614/90/$ 03.50

the present paper we show how quantum mechanical reactive scattering calculations can be structured so as to fulfil these criteria.

The hypercube architecture is a leading design for MIMD-type (multiple instruction multiple data) distributed memory parallel architectures based on message passing. The first such machine was developed by Seitz [22] and used by Fox [23,24], both at Caltech. We have created efficient codes to solve the quantum mechanical equation of motion for reactive collisions of an atom with a diatomic molecule using a hypercube computer of this type. Very similar codes should be appropriate for other MIMD distributed memory parallel architectures.

In this paper, we present a concurrent algorithm for calculating local hyperspherical surface functions (LHSF) and use a parallelized version [25] of Johnson's logarithmic derivative method [26], modified to include the improvements suggested by Manolopoulos [27], for integrating the resulting coupled channel reactive scattering equations. We review the formalism briefly in section 2. In section 3 we discuss the parallel algorithms and in section 4 we compare the results of scattering calculations on the Caltech/JPL Mark IIIfp 64 processor hypercube for the $H+H_2$ system $J=0$, 1, 2 partial waves on the LSTH [28,29] potential energy surface with those of calculations done on a CRAY X-MP/48 and a CRAY-2. Both accuracy and performance are discussed, and speed estimates are made for the Mark IIIfp 128 processor hypercube soon to become available and the San Diego Supercomputer Center CRAY Y-MP/864 machine which has just been put into operation. We summarize the conclusions in section 5.

2. Methodology

The detailed formulation of reactive scattering based on hyperspherical coordinates and local variational hyperspherical surface functions (LHSF) is discussed elsewhere [8,9,15]. We present a very brief review to facilitate the explanation of the parallel algorithms.

For a triatomic system, we label the three atoms A_α, A_β and A_γ. Let (λ, ν, κ) be any cyclic permutation of the indices (α, β, γ). We define the λ coordinates, the mass-scaled [30] internuclear vector r_λ from A_ν to A_κ, and the mass-scaled position vector R_λ of A_λ with respect to the center of mass of the $A_\nu A_\kappa$ diatom. The symmetrized hyperspherical coordinates [20] are the hyperradius $\rho=(R_\lambda^2+r_\lambda^2)^{1/2}$, and a set of five angles ω_λ, γ_λ, θ_λ, ϕ_λ and ψ_λ, denoted collectively as ζ_λ. The first two of these are in the range 0 to π and are respectively $2\arctan(r_\lambda/R_\lambda)$ and the angle between R_λ and r_λ. The angles θ_λ, ϕ_λ are the polar angles of R_λ in a space-fixed frame and ψ_λ is the tumbling angle of the R_λ, r_λ half-plane around its edge R_λ. The hamiltonian $\hat{H}_\lambda$ is the sum of a radial kinetic energy operator term in ρ, and the surface Hamiltonian $\hat{h}_\lambda$, which contains all differential operators in ζ_λ and the electronically adiabatic potential $V(\rho, \omega_\lambda, \gamma_\lambda)$. $\hat{h}_\lambda$ depends on ρ parametrically and is therefore the "frozen" hyperradius part of $\hat{H}_\lambda$.

The scattering wave function $\Psi^{JM\Pi\Gamma}$ is labelled by the total angular momentum J, its projection M on the laboratory-fixed Z axis, the inversion parity Π with respect to the center of mass of the system and the irreducible representation Γ of the permutation group of the system (P_3 for $H+H_2$) to which the electronuclear wave function, excluding the nuclear spin part [31,32], belongs. It can be expanded in terms of the LHSF $\Phi^{JM\Pi\Gamma}$, defined below, and calculated at the values $\bar{\rho}_q$ of ρ:

$$\Psi_i^{JM\Pi\Gamma}(\rho, \zeta_\lambda) = \sum_n b_{ni}^{J\Pi\Gamma}(\rho; \bar{\rho}_q)\Phi_n^{JM\Pi\Gamma}(\zeta_\lambda; \bar{\rho}_q) . \quad (1)$$

The index i is introduced to permit consideration of a set of many linearly independent solutions of the Schrödinger equation corresponding to distinct initial conditions which are needed to obtain the appropriate scattering matrices.

The LHSF $\Phi_n^{JM\Pi\Gamma}(\zeta_\lambda; \bar{\rho}_q)$ and associated energies $\epsilon_n^{J\Pi\Gamma}(\bar{\rho}_q)$ are respectively the eigenfunctions and eigenvalues of the surface Hamiltonian $\hat{h}_\lambda$. They are obtained using a variational approach [15]. The variational basis set consists of products of Wigner rotation matrices $D^J_{M\Omega}(\phi_\lambda, \theta_\lambda, \psi_\lambda)$, associated Legendre functions of γ_λ and functions of ω_λ which depend parametrically on $\bar{\rho}_q$ and are obtained from the numerical solution of one-dimensional eigenvalue–eigenfunction differential equations in ω_λ involving a potential related to $V(\bar{\rho}, \omega_\lambda, \gamma_\lambda)$.

The variational method leads to an eigenvalue problem with coefficient and overlap matrices $h^{J\Pi\Gamma}(\bar{\rho}_q)$ and $s^{J\Pi\Gamma}(\bar{\rho}_q)$ and whose elements are five-

dimensional integrals involving the variational basis functions.

The coefficients $b_{ni}^{J\pi\Gamma}(\rho;\bar{\rho}_q)$ defined by eq. (1) satisfy a coupled set of second-order differential equations involving an interaction matrix $\mathcal{I}^{J\pi\Gamma}(\rho;\bar{\rho}_q)$ whose elements are defined by

$$[\mathcal{I}^{J\pi\Gamma}(\rho;\bar{\rho}_q)]_{n'}^{n} = \langle \Phi_{n'}^{JM\pi\Gamma}(\zeta_\lambda;\bar{\rho}_q)\,|\,V(\rho,\omega_\lambda,\gamma_\lambda) - (\bar{\rho}_q/\rho)^2 V(\bar{\rho}_q,\omega_\lambda,\gamma_\lambda)\,|\,\Phi_n^{JM\pi\Gamma}(\zeta_\lambda;\bar{\rho}_q)\rangle . \quad (2)$$

The configuration space ρ, ζ_λ is divided in a set of Q hyperspherical shells $\rho_q \leqslant \rho \leqslant \rho_{q+1}$ $(q=1, 2, ..., Q)$ within each of which we choose a value $\bar{\rho}_q$ used in expansion (1).

When changing from the LHSF set at $\bar{\rho}_q$ to the one at $\bar{\rho}_{q+1}$ neither $\Psi_i^{JM\pi\Gamma}$ nor its derivative with respect to ρ should change. This imposes continuity conditions on the $b_{ni}^{J\pi\Gamma}$ and their ρ derivatives at $\rho=\rho_{q+1}$, involving the overlap matrix $\mathcal{C}^{J\pi\Gamma}(\bar{\rho}_{q+1},\bar{\rho}_q)$ between the LHSF evaluated at $\bar{\rho}_q$ and $\bar{\rho}_{q+1}$

$$[\mathcal{C}^{J\pi\Gamma}(\bar{\rho}_{q+1},\bar{\rho}_q)]_{n'}^{n} = \langle \Phi_{n'}^{JM\pi\Gamma}(\zeta_\lambda;\bar{\rho}_{q+1})\,|\,\Phi_n^{JM\pi\Gamma}(\zeta_\lambda;\bar{\rho}_q)\rangle . \quad (3)$$

The five-dimensional integrals required to evaluate the elements of $h^{J\pi\Gamma}$, $s^{J\pi\Gamma}$, $\mathcal{I}^{J\pi\Gamma}$ and $\mathcal{C}^{J\pi\Gamma}$ are performed analytically over ϕ_λ, θ_λ and ψ_λ and by two-dimensional numerical quadratures over γ_λ and ω_λ. These quadratures account for 90% of the total time needed to calculate the LHSF $\Phi_n^{JM\pi\Gamma}$ and the matrices $\mathcal{I}^{J\pi\Gamma}$ and $\mathcal{C}^{J\pi\Gamma}$.

The system of second-order ordinary differential equations in the $b_{ni}^{J\pi\Gamma}$ is integrated as an initial value problem from small values of ρ to large values using Manolopoulos' logarithmic derivative propagator [27]. Matrix inversions account for more than 90% of the time used by this propagator. All aspects of the physics can be extracted from the solutions at large ρ by a constant ρ projection [8,9,33].

3. Parallel algorithm

The computer used for this work is a 64 processor Mark IIIfp hypercube. Each node consists of two independent Motorola 68020 microprocessors, one for computation and one for I/O, and four megabytes of dynamic memory. The computation microprocessor has a Motorola 68882 floating-point arithmetic coprocessor and 128 kilobytes of static private memory. The I/O microprocessor has 64 kilobytes of static private memory. An additional daughter board with a pipe-lined 32-bit floating point unit based on the Weitek XL series of chips is attached to each node and has a nominal peak speed of 16 Mflops. The crystalline operating system (CrOS)-channel-addressed synchronous communication provides the library routines to handle communications between nodes [24,34,35]. Program development is done on a Motorola 68020-based Counterpoint workstation that runs on UNIX. The programs are written in C programming language except for the time-consuming two-dimensional quadratures and matrix inversions, which are optimized in assembly language.

The hypercube is configured as a two-dimensional array of processors. The mapping is done using binary Gray codes [24,36] which gives the Cartesian coordinates in processor space and communication channel tags for a processor's nearest neighbors. With a distributed-memory machine like the hypercube, the elements of a large matrix of data must be distributed across the memory of all the processors. This makes it possible to fully utilize the large memory available and facilitates the load-balancing task of keeping most of the processors busy doing useful arithmetic most of the time. The parallelization of scientific codes is frequently based on a large grain size decomposition of the task. A method of distributing the global matrix among the processors is the first choice that must be made and it is closely related to the parallel algorithm chosen.

We mapped the matrices into processor space by local decomposition. Let N_r and N_c be the number of processors in the rows and columns of the hypercube configuration, respectively. Element $A(i, j)$ of an $M\times M$ matrix is placed in processor row $P_r=\mathrm{int}(iN_r/M)$ and column $P_c=\mathrm{int}(jN_c/M)$, where int x means the integer part of x.

The parallel code implemented on the hypercube consists of five major steps. Step one constructs, for each value of $\bar{\rho}_q$, a primitive basis set composed of the product of Wigner rotation matrices, associated Legendre functions, and the numerical one-dimensional functions in ω_λ mentioned in section 2 and obtained by solving the corresponding one-dimensional eigenvalue–eigenvector differential equation using a finite difference method. This requires tha-

a subset of the eigenvalues and eigenvectors of a tridiagonal matrix be found.

A bisection method [37] which accomplishes the eigenvalue computation using the TRIDIB routine from EISPACK [38] was ported to the Mark IIIfp. This implementation of the bisection method allows computation of any number of consecutive eigenvalues specified by their indices. Eigenvectors are obtained using the EISPACK inverse iteration routine TINVIT with modified Gram–Schmidt orthogonalization. Each processor solves independent tridiagonal eigenproblems since the number of eigenvalues desired from each tridiagonal system is small but there are a large number of distinct tridiagonal systems. To achieve load balancing, we distributed subsets of the primitive functions among the processors in such a way that no processor computes greater than one eigenvalue and eigenvector more than any other. These large grain tasks are most easily implemented on MIMD machines; SIMD (single instruction multiple data) machines would require more extensive modifications and would be less efficient because of the sequential nature of effective eigenvalue iteration procedures. The one-dimensional bases obtained are then broadcast to all the other nodes.

In step two a large number of two-dimensional quadratures involving the primitive basis functions which are needed for the variational procedure are evaluated. These quadratures are highly parallel procedures requiring no communication overhead once each processor has the necessary subset of functions. Each processor calculates a subset of integrals independently.

Step three assembles these integrals into the real symmetric dense matrices $s^{JnP}(\bar{\rho}_q)$ and $h^{JnP}(\bar{\rho}_q)$ which are distributed over processor space. The entire spectrum of eigenvalues and eigenvectors for the associated variational problem is sought. With the parallel implementation of the Householder method [39], this generalized eigensystem is tridiagonalized and the resulting single tridiagonal matrix is solved in each processor completely with the QR algorithm [40]. The QR implementation is purely sequential since each processor obtains the entire solution to the eigensystem. However, only different subsets of the solution are kept in different processors for the evaluation of the interaction and overlap matrices in step four. This part of the algorithm is not time-consuming and the straightforward sequential approach was chosen. It has the further effect that the resulting solutions are fully distributed, so no communication is required.

Step four evaluates the two-dimensional quadratures needed for the interaction $\mathcal{I}^{JnP}(\rho; \bar{\rho}_q)$ and overlap $\mathcal{C}^{JnP}(\bar{\rho}_{q+1}; \bar{\rho}_q)$ matrices. The same type of algorithms are used as were used in step two. By far, the most expensive part of the sequential version of the surface function calculation is the calculation of the large number of two-dimensional numerical integrals required by steps two and four. These steps are, however, highly parallel and well suited for the hypercube.

Step five uses Manolopoulos' [27] algorithm to integrate the coupled linear ordinary differential equations. The parallel implementation of this algorithm is discussed elsewhere [25]. The algorithm is dominated by parallel Gauss–Jordan matrix inversion and is I/O intensive, requiring the input of one interaction matrix per integration step. To reduce the I/O overhead a second source of parallelism is exploited. The entire interaction matrix (at all ρ) and overlap matrix (at all $\bar{\rho}_q$) data sets are loaded across the processors and many collision energies are calculated simultaneously. This strategy works because the same set of data is used for each collision energy and because enough main memory is available. Calculation of scattering matrices from the final logarithmic derivative matrices is not computationally intensive, and is done sequentially.

The program steps were all run on the Weitek coprocessor which only supports 32-bit arithmetic. Experimentation has shown that this precision is sufficient for the work reported below. The 64-bit arithmetic hardware needed for larger calculations was installed after the present calculations were completed.

4. Results and discussion

Accuracy. Calculations were performed for the $H+H_2$ system on the LSTH surface [28,29] for partial waves with total angular momentum $J=0$, 1, 2 and energies up to 1.6 eV. Flux is conserved to better than 1% for $J=0$, 2.3% for $J=1$ and 3.6% for $J=2$

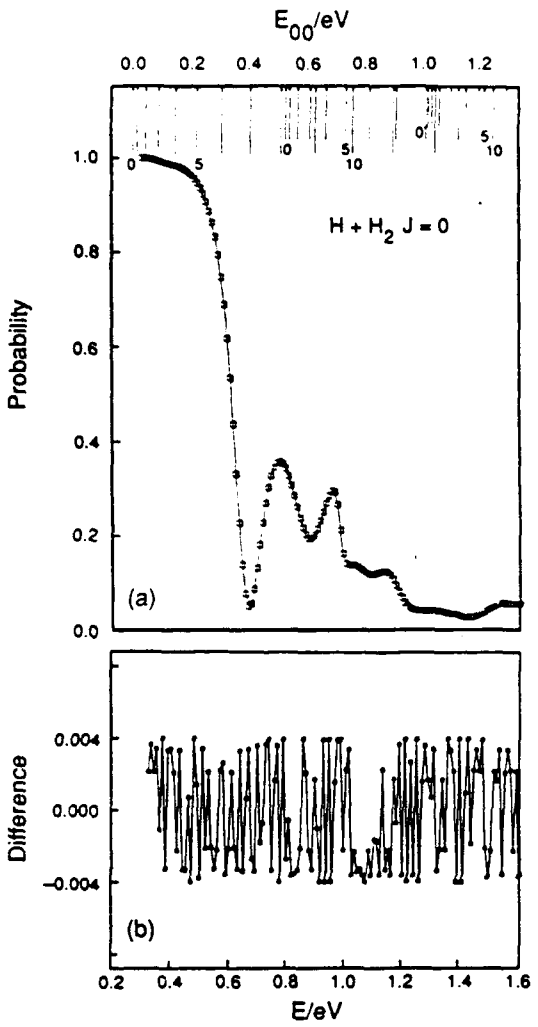

Fig. 1. Probabilities (a) and probability differences (b) as a function of total energy E (lower abscissa) and initial relative translational energy E_{00} (upper abscissa) for the $J=0$ (0, 0, 0) → (0, 0, 0) A_1 symmetry transition in $H+H_2$ collisions on the LSTH potential energy surface. The symbol (v, j, Ω) labels an asymptotic state of the $H+H_2$ system in which v, j, and Ω are the quantum numbers of the initial or final H_2 states. The vertical arrows on the upper abscissa denote the energies at which the corresponding $H_2(v, j)$ states open up. The length of those arrows decreases as v spans the values 0, 1 and 2, and the numbers 0, 5, and 10 associated with the arrows define a labelling for the value of j. (a) The results from the Mark IIIfp hypercube; (b) differences between these and those from the CRAY X-MP/48. The number of LHSF used was 36 and the number of primitives used to calculate these surface functions was 80.

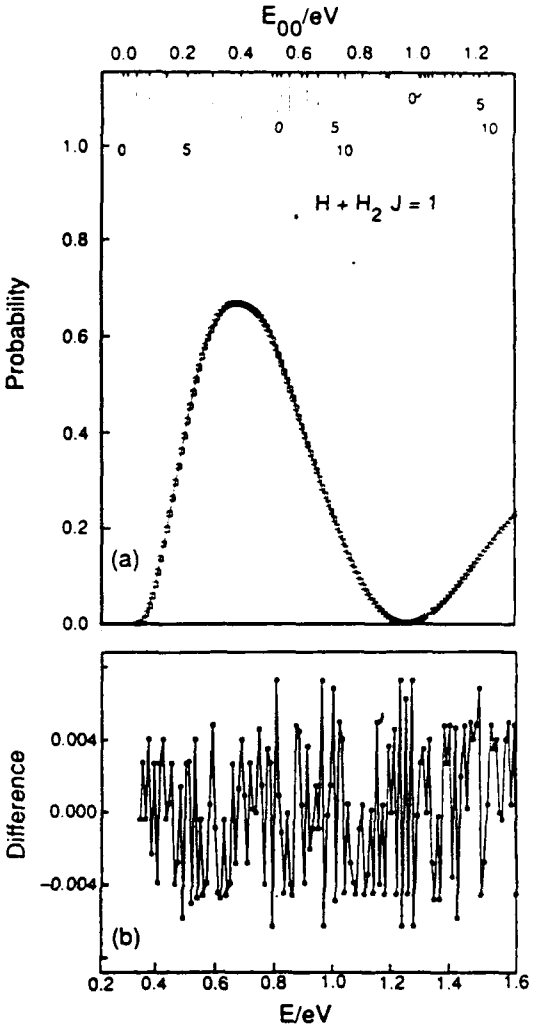

Fig. 2. Same as for fig. 1 except for $J=1$, A_1, odd parity ($\Pi=!$), (0, 0, 0) → (0, 0, 2) transitions. The number of LHSF used was 74 and the number of primitives used to calculate these surface functions was 152.

for all open channels over the entire energy range considered.

To illustrate the accuracy of the 32-bit arithmetic calculations, the scattering results from the Mark IIIfp with 64 processors are shown in figs. 1, 2, and 3 for $J=0$, 1, 2, respectively, in which some transition probabilities as a function of the total collision energy E are plotted. Also shown are the differences between these results and those obtained using a

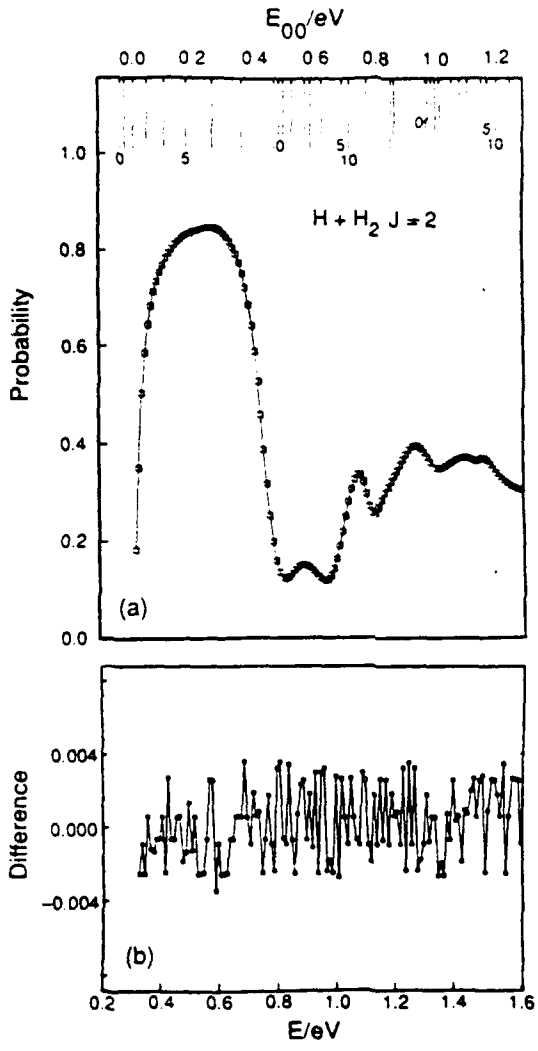

Fig. 3. Same as for fig. 1 except for $J=2$, A_1, odd parity ($\Pi=1$), $(0, 2, 1) \rightarrow (0, 2, 1)$ transition. The differences plotted in (b) are between the Mark IIIfp hypercube and the CRAY-2 results. The number of *LHSF used was 65 and the number of primitives used* to calculate these surface functions was 136.

CRAY X-MP/48 and a CRAY-2. These differences do not excede 0.004 in absolute value over the energy range investigated. The effect of the geometric phase associated with the conical intersection between the two lowest electronic potential energy surface of H_3 [32] is not included in these results. Much of the structure in the transition probability curves is due to the underlying resonances [1, 9, 16] and are discussed below. The two sets of data in each figure are virtually indistinguishable on the scale of the plots.

Analysis of $J=2$ resonances. Table 1 contains a list of the $J=2$ resonance energies detected from the maxima in the lifetime versus energy curves, calculated as described previously [9,16], as well as their quantum number assignments, permutation and inversion symmetry labels, and lifetimes. The permutation symmetries are given with and without the inclusion of the effect of the geometrical phase (GP) associated with the conical intersection between the two lowest electronic state potential energy surfaces [31,32]. The energy of these resonances is consistent with the physical model for the selection rule previously developed [16] and tested with the $J=0$, 1 resonances. The results of table 1 adds additional credence to the generality of that rule. According to it, if GP effects are ignored, a necessary (but not sufficient) condition for resonances to occur in $A_1(A_2)$ partial waves is that $(-1)^{\Pi+K}$ be equal to $1(-1)$, where K is the vibrational angular momentum quantum number, whereas they are permitted in E partial waves for all K. To include the GP effect, it suffices to interchange A_1 and A_2 in this selection rule [32]. In agreement with this picture, not all higher energy $J=2$ resonances which are allowed by this rule were detected.

Timing and parallel efficiency. In tables 2 and 3 we present the timing data on the 64 processor Mark IIIfp, a CRAY X-MP/48 and a CRAY-2, for both the surface function code (including calculation of the overlap $\mathcal{C}^{J\Pi\Gamma}$ and interaction $\mathcal{J}^{J\Pi\Gamma}$ matrices) and the logarithmic derivative propagation code. For the surface function code, the speeds on the first two machines is about the same. The CRAY-2 is 1.43 times faster than the Mark IIIfp and 1.51 times faster than the CRAY X-MP/48 for this code. The reason is that this program is dominated by matrix–vector multiplications which are done in optimized assembly code in all three machines. For this particular operation the CRAY-2 is 2.03 times faster than the CRAY X-MP/48 whereas for more memory-intensive operations the CRAY-2 is slower than the CRAY X-MP/48 [41]. A slightly larger primitive basis set is required on the Mark IIIfp in order to obtain surface function energies of an accuracy equivalent to that obtained with the CRAY machines. This is due

Table 1
$J=2$ resonances and their characteristics for H_3

Assignment	Permutation symmetry [a]		Inversion symmetry Π [c]	E (eV)	Lifetime (fs)
	without GP [b]	with GP [b]			
$(0, 0^0, 0)$	A_1, E	A_2, E	0	0.65	11
$(0, 1^1, 0)$	A_2, A_1, E	A_1, A_2, E	0, 1	0.77	9
$(0, 2^0, 0)$	A_1, E	A_2, E	0	0.88	10
$(0, 2^2, 0)$	A_1, A_2, E	A_2, A_1, E	0, 1	0.90	10
$(1, 0^0, 0)$	A_1, E	A_2, E	0	0.98	28
$(0, 3^1, 0)$	A_2, A_1, E	A_1, A_2, E	0, 1	1.00	8
$(1, 1^1, 0)$	A_2, A_1, E	A_1, A_2, E	0, 1	1.09	29
$(0, 4^0, 0)$	A_1, E	A_2, E	0	1.10	5
$(0, 4^2, 0)$	A_1, A_2, E	A_2, A_1, E	0, 1	1.12	5
$(1, 2^2, 0)$	A_1, A_2, E	A_2, A_1, E	0, 1	1.22	8
$(0, 5^1, 0)$	A_2, A_1, E	A_1, A_2, E	0, 1	1.22	6
$(2, 1^1, 0)$	A_2, A_1, E	A_1, A_2, E	0, 1	1.45	38

[a] This refers to the irreducible representation of the P_3 permutation group to which the electronuclear wave function, excluding the nuclear spin part, belongs [31,32].

[b] With(out) GP refers to the case in which the effect of the geometrical phase associated to conical intersection between the two lowest electronic state potential energy surface is (not) included [31,32].

[c] When two values of Π are indicated, the first (second) one is associated with the first (second) permutation symmetry.

to the lower accuracy of the 32-bit arithmetic of the former with respect to the 64-bit arithmetic of the latter.

The absolute times presented in table 2 and 3 are apt to decrease as the codes are improved and the numerical parameters are further tuned. As a result, they are not well suited for an appropriate comparison of the relative effectiveness of different reactive scattering methodologies [8–19]. The relevant information in those tables is, instead, the relative times among different machines as given by the corresponding speeds. These are indicative of the relative effectiveness of these machines for performing the reactive scattering calculations described in this paper.

The efficiency (ϵ) of the parallel LHSF code was determined using the definition $\epsilon = T_1/NT_N$, where T_1 and T_N are respectively the implementation times using a single processor and N processors. The single processor times are obtained from runs performed after removing the overhead of the parallel code, i.e. after removing the communication calls and some logical statements. Perfect efficiency ($\epsilon = 1.0$) implies that the N processor hypercube is N times faster than a single processor. In fig. 4 efficiencies for the surface function code (including the calculation of the overlap and interaction matrices) as a function of the size of the primitive basis set are plotted for 2, 4, 8, 16, 32 and 64 processor configurations of the hypercube. The global dimensions of the matrices used are chosen to be integer multiples of the number of processor rows and columns in order to insure load balancing among the processors. Because of the limited size of a single processor memory, the efficiency determination is limited to 32 primitives. As shown in fig. 4, the efficiencies increase monotonically and approach unity asymptotically as the size of the calculation increases. Converged results require large enough primitive basis sets so that the efficiency of the surface function code is estimated to be about 0.95 or greater.

The data for the logarithmic derivative code given in table 3 for a 245 channel (i.e. LHSF) example show that the Mark IIIfp has a speed about 62% to that of the CRAY-2 but only about 31% of that of the CRAY X-MP/48. This code is dominated by matrix inversions, which are done in optimized assembly code in all three machines. The reason for the slowness of the hypercube with respect to the CRAYs is that the efficiency of the parallel logarithmic derivative code is 0.52. This relatively low value is due to the fact that matrix inversions require a significant

Table 2
Performance of the surface function code [a]

J	Mark IIIfp [b] 64 processors		CRAY X-MP/48		CRAY-2	
	time (h)	speed (Mflops)	time (h)	speed (Mflops)	time (h)	speed (Mflops)
0	0.71 [c]	100 [d]	0.74 [e]	96 [f]	0.49 [g]	145 [h]
1	2.88 [i]	112 [d]	3.04 [j]	106 [f]	2.01 [k]	160 [h]
2	5.60 [l]	124 [d]	5.94 [m]	117 [n]	3.96 [o]	176 [k]

[a] This code calculates the surface functions at the 51 values of β from 2.0 to 12.0 bohr in steps of 0.2 bohr, the corresponding overlap matrices between consecutive values of β and the propagation matrices in ρ steps of 0.1 bohr. The number of primitives used for each J and described in the remaining footnotes permits us to generate enough LHSF to achieve the accuracy described in the text.

[b] Sixty-four single precision processors.

[c] For 80 A_1, 80 A_2 and 160 E primitives. This basis is larger than the one described in e) below and is needed to generate the same number of linearly independent surface functions as in e). The reason for this difference is the 32-bit arithmetic of the Mark IIIfp compared to the 64-bit arithmetic of the CRAY X-MP/48.

[d] Estimated on the basis of the absolute measured speed on the CRAY X-MP/48 and the measured relative speeds of the Mark IIIfp with respect to the CRAY X-MP/48.

[e] For 76 A_1, 76 A_2 and 152 E primitives.

[f] Measured using the hardware-performance monitor of the PERFMON and PERFPRT subroutines.

[g] This time, for the same primitives as describes in e) was estimated on the basis of the relative speeds of the CRAY-2 and CRAY X-MP/48 measured for a set of five values of β. It is smaller than the time in e) for the reason in h).

[h] Estimated on the basis of the relative speed of the CRAY-2 with respect to the CRAY X-MP/48 described in g). The reason this speed is $\frac{3}{4}$ of the corresponding CRAY X-MP/48 speed is that the dominant parts of the calculation are optimized assembly code matrix–vector multiplications for which the CRAY-2 is 50% faster than the CRAY X-MP/48. Otherwise, the CRAY-2 is slightly slower than CRAY X-MP/48. See text.

[i] For 72 A_1, 80 A_2 and 152 E primitives of even parity and 152 A_1, 160 A_2 and 312 E primitives of odd parity. These numbers of primitives are larger than the ones given in j) for the reason given in c).

[j] For 64 A_1, 76 A_2 and 140 E primitives of even parity and 140 A_1, 152 A_2 and 292 E primitives of odd parity.

[k] Estimated on the basis of the relative speeds of the CRAY X-MP/48 and CRAY-2 and the measured CRAY X-MP/48 times or speeds.

[l] For 216 A_1, 232 A_2 and 448 E primitives of even parity and 136 A_1, 152 A_2 and 288 E primitives of odd parity. These numbers are larger than those in o) for the reason given in c).

[m] This time is estimated as in k), since the calculation cannot be done on the CRAY X-MP/48 because of insufficient memory.

[n] *Estimated to be the same as in f) since the calculation cannot be done on the CRAY X-MP/48 for the reason given in m).*

[o] For 204 A_1, 216 A_2 and 420 E primitives of even parity and 128 A_1, 140 A_2 and 268 E primitives of odd parity.

amount of inter-processor communication. Fig. 5 displays efficiencies of the logarithmic derivative code as a function of the number of channels propagated for different processor configurations, as done previously for the Mark III [25,42] hypercubes. The data can be fit well be an operations count formula developed previously for the matrix inversion part of the code [43]; this formula can be used to extrapolate the data to larger numbers of processors or larger numbers of channels. It can be seen that for an 8 processor configuration, the code runs with an efficiency of 0.81. This observation suggested that we divide the Mark IIIfp into 8 clusters of 8 processors each and perform calculations for different energies in different clusters. The corresponding timing information is also given in table 3. As can be seen from the last row of this table, the speed of the logarithmic derivative code using this configuration of the 64 processor Mark IIIfp is 48.5 Mflops, which is about 44% of that of the CRAY X-MP/48 and 88% of that of the CRAY-2. As the number of channels increases, the number of processors per cluster may be made larger in order to increase the amount of memory available in each cluster. The corresponding efficiency should continue to be adequate due to the larger matrix dimensions involved.

In the near future, the number of processors of the Mark IIIfp will be increased to 128 and the I/O system will be replaced by high performance CIO (concurrent I/O) hardware. The new Weitek coprocessors installed since the present calculations were done perform 64 bit floating point arithmetic at about the

Table 3
Performance of the logarithmic derivative code [a]

	Mark IIIfp [b]		CRAY X-MP/48	CRAY-2
	64 processor global configuration [c]	8 clusters of 8 processors [d]		
total time (h)	4.8 [e]	3.4 [f,g]	1.5	2.9 [h]
time for 1 energy (min)	2.2 [i]	1.6 [i]	0.7	1.3
efficiency	0.52	0.81	-	-
speed [j] (Mflops)	34.4 [k]	48.5 [k]	110	55.4

[a] Based on a calculation using 245 surface functions and 131 energies, and a logarithmic derivative integration step of 0.01 bohr.
[b] Sixty-four single precision processors.
[c] The calculation for each energy was distributed among all 64 processors.
[d] The hypercube was configured into 8 clusters of 8 processors each. Each cluster did full calculations for 16 energies, for a total of 128 energies. The times reported were multiplied by 131/128 for normalization purposes. All 8 clusters operated simultaneously.
[e] This includes 1.9 h of I/O time.
[f] This includes 1.6 h of I/O time. This time is shorter than that in e) because of a different and more efficient broadcast of the data between the host and the 8 clusters.
[g] Each cluster did full calculations for 16 energies for a total of 128 energies. The total time reported was obtained by subtracting the I/O time from the measured time, multipling the result by 131/128 for normalization to 131 energies and adding the I/O time.
[h] Estimated on the basis of the CRAY X-MP/48 times and the ratio of the speeds of the CRAY-2 and CRAY X-MP/48 for the logarithmic derivative code.
[i] This includes the pro-rated I/O contribution.
[j] All speeds include I/O contribution.
[k] Estimated on the basis of the measured CRAY X-MP/48 speed for the logarithmic derivative code and the relative speeds of the Mark IIIfp and CRAY X-MP/48 for this code.

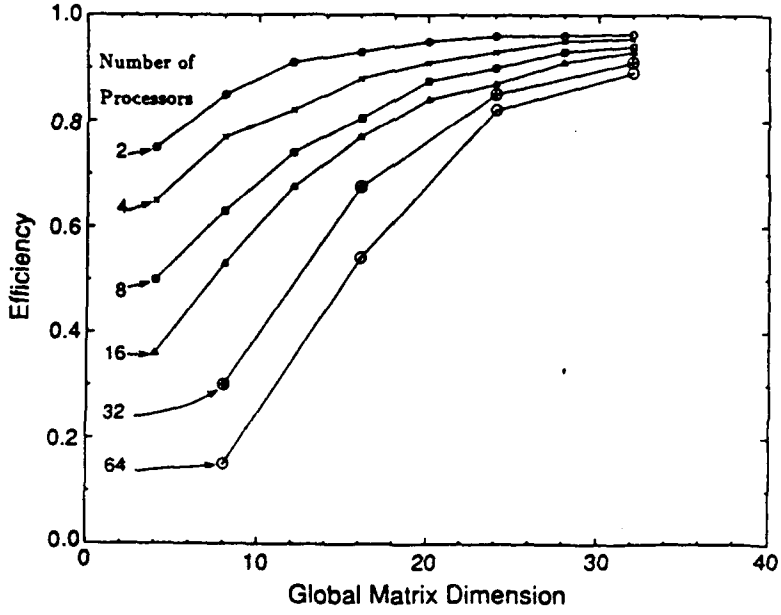

Fig. 4. Efficiency of the surface function code (including the calculation of the overlap and interaction matrices) as a function of the global matrix dimension (i.e. the size of the primitive basis set) for 2, 4, 8, 16, 32, and 64 processors. The solid curves are straight line segments connecting the data points for a fixed number of processors and are provided as an aid to examine the trends.

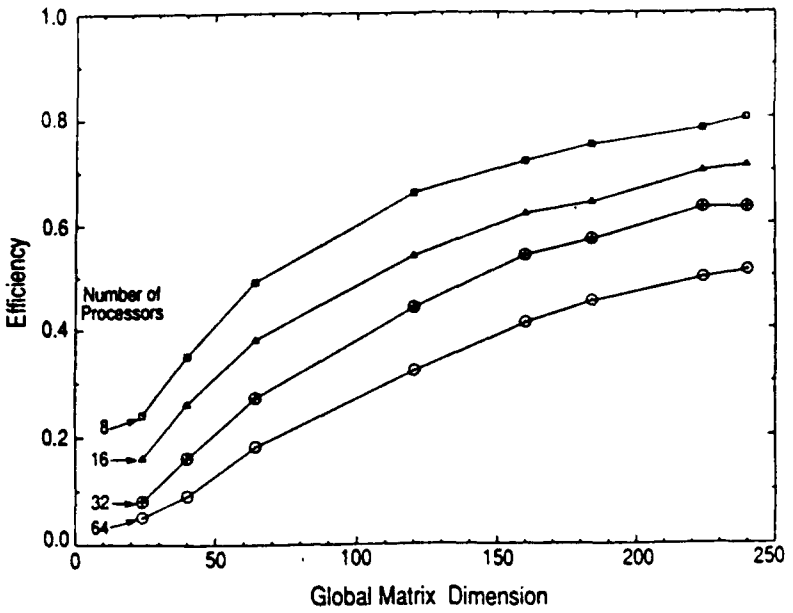

Fig. 5. Efficiency of logarithmic derivative code as a function of the global matrix dimension (i.e. the number of channels of LHSF) for 8, 16, 32, and 64 processors. The solid curves are straight line segments connecting the data points for a fixed number of processors and are provided as an aid to examine the trends.

Table 4
Overall speed of reactive scattering codes on several machines

	Mark IIIfp		CRAY X-MP/48	CRAY-2	CRAY Y-MP/864
	64 processor	128 processors			
surface function code for $J=2$ (Mflops)	124	240 [a]	117 [b]	176 [b]	232 [b]
logarithmic derivative code [c] (Mflops)	48.5 [d]	127 [a,d,e]	110 [b]	55.4 [b]	187 [b]
total main memory of computer (64-bit Mwords)	32	64	8	256	64

[a] Estimated on the basis of the 64 processor performance.
[b] For single processor operation.
[c] For 245 channels. As the number of channels increases, the Mark IIIfp speed increases by a factor not exceeding 1.25, but the speed of the CRAY machines remains approximately constant.
[d] Hypercube configured in clusters of 8 processors.
[e] This speed assumes four-fold increase in the I/O data rate, compared to the 64 processor machine, due to concurrent I/O hardware.

same nominal peak speed as the 32 bit boards. From the data in the present paper it is possible to predict with good reliability the performance of this upgraded version of the Mark IIIfp. A CRAY Y-MP/864 has just been installed at the San Diego Supercomputer Center. Initial speed measurements show that it is 2 times faster than the CRAY X-MP/48 for the surface function code and 1.7 times faster for the logarithmic derivative code. In table 4, we summarize the available or predicted speed information for

the present codes for the current 64 processor and near future 128 processor Mark IIIfp as well as the CRAY X-MP/48, CRAY-2 and CRAY Y-MP/864 supercomputers. Its can be seen that Mark IIIfp machines are competitive with all of the currently available CRAYs (operating as single processor machines).

5. Summary

We performed quantum mechanical reactive scattering calculations on the Mark IIIfp hypercube parallel computer. The results obtained for the $H+H_2$ system $J=0$, 1, 2 partial waves agree well with those from a CRAY X-MP/48 and a CRAY-2. The resonance structure in the $J=2$ calculations is consistent with a selection rule developed previously [9,16]. The high degree of parallelism of the most time-consuming step of the surface function calculation (the evaluation of two-dimensional numerical quadratures) leads to a high efficiency for that calculation. As a result, the speed of the 64 processor Mark IIIfp for the surface function calculation is about the same as that of the CRAY X-MP/48 and about 0.7 of that of the CRAY-2. When configuring the Mark IIIfp into 8 clusters of 8 processors each, the logarithmic derivative code is about 56% slower than the CRAY X-MP/48 and 12% slower than the CRAY-2. The speed of the 128 processor Mark IIIfp soon to become available should exceed, both for the surface function calculation and the logarithmic derivative calculation, those of the CRAY X-MP/48 and CRAY-2; however, although still comparable to the CRAY Y-MP/864 for the surface function code, it will be 32% slower for the logarithmic derivative code (the CRAYs operating as single processor machines). These results demonstrate the feasibility of performing reactive scattering calculations with high efficiency in parallel fashion. As the number of processors continues to increase, such parallel calculations in systems of greater complexity will become practical in the not too distant future.

Acknowledgement

The work described in this paper was supported in part by DOE Grant DE-AS03-83ER and Air Force Astronautic Laboratory contract F04611-86-K-0067. The calculations were performed on the 64 processor Mark IIIfp Caltech/JPL hypercube, the CRAY X-MP/48 and CRAY Y-MP/864 at the NSF San Diego Supercomputing Center and the CRAY-2 at the Air Force Weapons Laboratory and we thank those institutions for their help. We also thank Dr. B. Lepetit and Professor Geoffrey Fox for useful discussions.

References

[1] G.C. Schatz and A. Kuppermann, J. Chem. Phys. 62 (1975) 2502; 65 (1976) 4642, 4668.
[2] A.B. Elkowitz and R.E. Wyatt, J. Chem. Phys. 62 (1975) 2504; 63 (1975) 702.
[3] R.B. Walker, E.B. Stechel and J.C. Light, J. Chem. Phys. 69 (1978) 2922.
[4] R.B. Bernstein, ed., Atom–molecule collision theory (Plenum Press, New York, 1979).
[5] G.C. Schatz, in: Proceeding of NATO workshop, Orsay, France, Theory of chemical reaction dynamics, ed. D.C. Clary (1986) p. 1.
[6] B.C. Garrett and D.G. Truhlar, Ann. Rev. Phys. Chem. 35 (1984) 159.
[7] J.M. Bowman, Advan. Chem. Phys. 61 (1985) 115.
[8] A. Kuppermann and P.G. Hipes, J. Chem. Phys. 84 (1986) 5962.
[9] P.G. Hipes and A.. Kuppermann, Chem. Phys. Letters 133 (1987) 1.
[10] G.A. Parker, R.T Pack, B.J. Archer and R.B. Walker, Chem. Phys. Letters 137 (1987) 564;
R.T Pack and G.A. Parker, J. Chem. Phys. 87 (1987) 3888.
[11] J.Z.H. Zhang and W.H. Miller, Chem. Phys. Letters 140 (1987) 329; 153 (1988) 465; 159 (1989) 130.
[12] G.C. Schatz, Chem. Phys. Letters 150 (1988) 92.
[13] J.Z.H. Zhang, D.J. Kouri, K. Haug, D.W. Schwenke, Y. Shima and D.G. Truhlar, J. Chem. Phys. 88 (1988) 2492.
[14] M. Mladenovic, M. Zhao, D.G. Truhlar, D.W. Schwenke, Y. Sun and D.J. Kouri, Chem. Phys. Letters 146 (1988) 358;
C.H. Yu, D.J. Kouri, M. Zhao and D.G. Truhlar, Chem. Phys. Letters 157 (1989) 491.
[15] S.A. Cuccaro, P.G. Hipes and A. Kuppermann, Chem. Phys. Letters 154 (1989) 155.
[16] S.A. Cuccaro, P.G. Hipes and A. Kuppermann, Chem. Phys. Letters 157 (1989) 440.
[17] F. Webster and J.C. Light, J. Chem. Phys. 90 (1989) 300.
[18] J. Linderberg, S. Padkjaer, Y. Öhrn and B. Vessal, J. Chem. Phys. 90 (1989) 6254.
[19] D.E. Manolopoulos and R.E. Wyatt, Chem. Phys. Letters 159 (1989) 123.
[20] A. Kuppermann, Chem. Phys. Letters 32 (1975) 374.

[21] R.T. Ling and Kuppermann, in: Electronic and atomic collisions, abstracts of Papers of the 9th International Conference on the Physics of Electronic and Atomic Collisions, Seattle, Washington, 24–30 July 1975, Vol. 1, eds. J.S. Rusley and R. Geballe (Univ. Washington Press, Seattle, 1975) pp. 353, 354.
[22] C.L. Seitz and J. Matisoo, Phys. Today 37 (1984) 38; C.L. Seitz, Comments ACM 28 (1985) 22.
[23] G.C. Fox and S.W. Otto, Phys. Today 37 (1984) 50.
[24] G.C. Fox, M.A. Johnson, G.A. Cyzenga, S.W. Otto, J.K. Salmon and D.W. Walker, in: Solving problems in concurrent processors (Prentice Hall, Englewood Cliffs, 1988).
[25] P.G. Hipes, T. Mattson, Y-S.M. Wu and A. Kuppermann, Proceedings of the Third Conference on Hypercube Concurrent Computers and Applications, Pasadena, 1988 (ACM, New York, 1988) pp. 1051–1061.
[26] B.R. Johnson, J. Compl. Phys. 13 (1973) 445; J. Chem. Phys. 67 (1977) 4086; NRCC Workshop, Lawrence Berkeley Laboratory, Report No. LBL 9501 (1979).
[27] D.E. Manolopoulos, J. Chem. Phys. 85 (1986) 6425.
[28] B. Liu, J. Chem. Phys. 58 (1973) 1925; P. Siegbahn and B. Liu, J. Chem. Phys. 68 (1978) 2457.
[29] D.G. Truhlar and C.J. Horowitz, J. Chem. Phys. 68 (1978) 2468; 71 (1979) 1514 (E).
[30] L.M. Delves, Nucl. Phys. 9 (1959) 391; 20 (1960) 275.
[31] B. Lepetit, Z. Peng and A. Kuppermann, Chem. Phys. Letters 166 (1990) 572.
[32] B. Lepetit and A. Kuppermann, Chem. Phys. Letters 166 (1990) 581.
[33] D.M. Hood and A. Kuppermann, in: Theory of chemical reaction dynamics, ed. D.C. Clary (Reidel, Dordrecht, 1986) pp. 193–214.
[34] G.C. Fox, ed. Caltech JPL Concurrent Computation Project Annual Report 1983–1984 (February 1985).
[35] G.C. Fox, G. Lyzenga, D. Rogstad and S. Otto, Proceedings of the 1985 ASME International Computers in Engineering Conference (1985). The Caltech Concurrent Computation Program-Project Description.
[36] E.N. Gilbert, Bell Syst. Techn. J. 37 (1958) 815; J. Salmon, Caltech Concurrent Computation Project Report C³P-51 (1984).
[37] I.C.F. Ipsen and E.R. Jessup, Proceeding of the Second Conference on Hypercube Multiprocessors, Knoxville, Tennessee (1987); Yale internal report: YALEU/DCS/RB-548; G.C. Fox, Caltech Concurrent Computation Project Report C³P-95 (1984).
[38] B.T. Smith, Lecture notes in computer science, Vol. 6. Matrix eigensystem routine – EISPACK guide, 2nd Ed. (Springer, Berlin, 1976).
[39] G.C. Fox, Caltech Concurrent Computation Project Report C³P-98 (1984); J. Patterson, Caltech Concurrent Computation Project Report C³P-56.58 (1986).
[40] J.H. Wilkinson and C. Reinsch, in: Handbook for automatic computation, Vol. 2. Linear algebra (Springer, Berlin, 1971) pp. 227–240.
[41] W. Pfeiffer, A. Alagar, A. Kamrath, R.H. Leary and J. Rogers, Benchmarking and Optimization of Scientific Codes on the CRAY X-MP, CRAY 2, and SCS-40 Vector Computers, November 1988, San Diego Supercomputer Center Report GA-A19478.
[42] P. Messina, C.F. Baillie, E.W. Felten, P.G. Hipes, D.W. Walker, R.D. Williams, W. Pfeiffer, A. Alagar, A. Kamrath, R.H. Leary and J. Rogers, Bechmarking Advanced Architecture Computers, Caltech Concurrent Computation Project Report C³P-712 (1988).
[43] P.G. Hipes and A. Kuppermann, in: Proceeding of the Third Conference on Hypercube Multiprocessors, Pasadena CA., January 1988, Vol. 2, Applications, ed. G.C. Fox (California Institute of Technology, Mail Stop 206-49, Pasadena, 1988) pp. 1621–1634.